Winter 1990

Effect of Passive Flow-Control Devices on Turbulent Low-Speed Base Flow

Farid Heidari Miandoab
Old Dominion University

EFFECT OF PASSIVE FLOW-CONTROL DEVICES ON TURBULENT LOW-SPEED BASE FLOW

by

Farid Heidari Miandoab
B.S. Mechanical Engineering, May 1981, Kansas State University
M.S. Mechanical Engineering, October 1983, Kansas State University

A Dissertation Submitted to the Faculty of
Old Dominion University in Partial Fulfillment of the
Requirements for the Degree of

DOCTOR OF PHILOSOPHY

MECHANICAL ENGINEERING

OLD DOMINION UNIVERSITY
December 1990

Approved by:

Dr. Gregory V. Selby (Director)

Dr. Robert L. Ash

Dr. Colin Britcher

Dr. Oktay Baysal

Dr. Woodrow Whitlow

ABSTRACT

EFFECT OF PASSIVE FLOW-CONTROL DEVICES ON TURBULENT LOW-SPEED BASE FLOW

Farid H. Miandoab
Old Dominion University, 1990
Director: Dr. Gregory V. Selby

Some configurations of blunt trailing-edge airfoils are known to have a lower pressure drag compared to sharp trailing-edge airfoils. However, this advantage in addition to the structural advantage of a thick trailing-edge airfoil is offset by its high base drag. At subsonic velocities, this is attributed to the low-pressure base flow dominated by a Karman vortex street. In the limiting case, the steady separated flow over a rearward-facing step is attained if the periodically shed vortices from a blunt trailing-edge are suppressed by the addition of a base splitter-plate.

Experimental studies in the Old Dominion University low-speed closed-circuit wind tunnel were conducted to examine the effect of several passive flow-control devices such as Wheeler doublets and wishbone vortex generators, longitudinal surface grooves, base cavities and serrations on the characteristics of two- and three-dimensional base flows. Flow over flat-plate airfoil and rearward-facing step models was studied in the turbulent incompressible subsonic flow regime. Models with trailing-edge and step-sweep angles of 0°, 30°, and 45° with respect to the

crossflow direction were considered. Constant-temperature hot-wire anemometry, infrared surface thermography, and pitot-static probes were used to conduct flow measurements. Parameters measured included vortex shedding frequency, convective heat-transfer rates, base pressure, and flow reattachment distance. Surveys of mean velocity profiles in the wake were also conducted.

Results have shown that most of the flow control devices tested increased the base pressure of the 2–D and 3–D flat-plate airfoils. Use of longitudinal surface grooves resulted in shorter flow reattachment distances and higher convective heat transfer rates downstream of the 2–D rearward-facing steps.

ACKNOWLEDGEMENTS

I wish to express my sincerest feelings of appreciation to my advisor, Dr. Gregory V. Selby, for the patient guidance he provided throughout the duration of this project. I am very thankful to my dissertation committee members, Drs. Robert L. Ash, Oktay Baysal, Colin P. Britcher, and Woodrow Whitlow of NASA Langley, for their helpful suggestions. I specially thank Ms. Diane Riddick for her professional job in typing the dissertation. I appreciate the help of my able friend Mr. Hamid Sayar.

My loving wife and companion in hardship and happiness, Lin, my caring mother, Azada, my kind brother, Vahid, and two precious sons, Ehsan and Sahand were a source of inspiration to me. To them, I dedicate this work.

TABLE OF CONTENTS

APPENDICES

LIST OF TABLES

LIST OF FIGURES

LIST OF SYMBOLS

A	area
A_b	base area
b	wake width $= 2\delta$
C_p	coefficient of pressure, $= \frac{P - P_{ref}}{1/2 \rho U_\infty^2}$
C_{pb}	coefficient of base pressure
$\overline{C_{pb}}$	mean base pressure coefficient $\{[\sum (P_b A)_i / A] - P_{ref}\} / 1/2 \rho U_\infty^2$
d	groove depth
D	diameter
Δf	frequency resolution
f	frequency, Hz
f_b	body forces
f_s	surface forces
h	base thickness or step height
h_w	vortex generating device height
I_1	wake parameter, $= \int_{-\infty}^{\infty} \left(\frac{w}{w_o}\right) d\left(\frac{y}{\delta}\right)$
I_2	wake parameter, $= \int_{-\infty}^{\infty} \left(\frac{w}{w_o}\right) d\left(\frac{y}{\delta}\right)$
P	pressure
P_b	base pressure
P_{ref}	reference pressure
Q_G	volumetric flow through grooves
Re	Reynolds number
Re_c	Reynolds number based on chord length
Re_h	Reynolds number based on trailing-edge thickness or step height
s	span along the base or step

St	Strouhal number
T	temperature
T_r	time record
t	time
u	streamwise velocity component
U_∞	freestream velocity
V	velocity vector
W	wake parameter, $= (w_o/U_\infty)(x/\theta)^{1/2}$
w	wake velocity defect
w_o	maximum wake velocity defect
w_r	rectangular groove width
x	streamwise coordinate
y	transverse coordinate
z	spanwise coordinate
z'	coordinate along the base of swept models

Greek Symbols

α	V-groove half angle
β	base sweep angle
δ	half-wake width measured from the wake axis to where the velocity defect is half the maximum value
δ_{bl}	boundary layer thickness
Δ	wake parameter, $= \delta/(x\theta)^{1/2}$
θ	momentum thickness
λ_1	uncertainity in thermocouple thermometer, % Rdg
λ_2	uncertainity in themocouple
λ_c	uncertainty in air velocity measurement, % Rdg
λ_f	uncertainty in frequency measurement, % Rdg
λ_p	uncertainty in differential pressure measurement, % Rdg
λ_{p1}	uncertainty in pressure transducer, % Rdg
λ_{p2}	uncertainty in multimeter, % Rdg
λ_s	uncertainty in measurement of Strouhal number

λ_T uncertainty in temperature measurement, % Rdg

λ_V uncertainty in air velocity measurement, % Rdg

λ_ρ uncertainty in air density measurement, % Rdg

ν kinematic viscosity

ρ density

Chapter 1

INTRODUCTION

1.1 Rationale

The advances which have been made in the field of base-flow research during the last decade vary depending on the particular flow regime concerned. In the case of subsonic periodic flow which exists downstream of an isolated three-dimensional blunt body or section, such as an airfoil with a blunt trailing edge, researchers are still at the stage of trying to effectively control the formation of the Karman vortex street through an understanding of the fundamental nature of base flow. In addition to low-speed periodic base flow, steady base flow can also exist. This type of steady flow occurs naturally downstream of a rearward-facing step in an otherwise continuous surface. This steady subsonic base flow can be considered to be the limiting flow configuration which would be attained if the strength of the vortex street behind an isolated section could be reduced to zero (Nash [1]*).

Non-periodic subsonic base flow is more amenable to theoretical treatment than the related flow involving the vortex street. Studies have been conducted which had as objectives the prediction of base pressures on two-dimensional rearward-facing steps and the prediction of the aerodynamic characteristics of airfoil sections with thick trailing edges with the constraint that the vortex street be successfully attenuated or eliminated (Rudy and Addy [2]). While the subsonic

---

* Numbers in brackets indicate references.

case, interest in base flows has been fairly limited, a great deal of effort has been devoted to research on supersonic base flows over the last two decades. A large volume of experimental data has been acquired, and the understanding of the nature of the flow, which is essentially steady, is already quite advanced. The development of theories for predicting base pressure has played a considerable role in research in this field, but in many respects, the theories are still inadequate pertaining to the detailed mechanics of the flow.

Most of the previous low-speed base-flow research has been performed on two-dimensional models. However, most full-scale geometries of practical interest are three-dimensional. Therefore, the need exists to gain a fundamental understanding of the flow physics associated with simple three-dimensional base geometries. Such geometries include, but are not limited to: 1) rearward-facing step with base swept at an angle relative to the plane normal to the free stream (herein referred to as a swept rearward-facing step) and 2) flat-plate airfoil with base swept at an angle relative to the direction normal to the free stream (herein referred to as the swept-base flat-plate airfoil model or simply the swept-wake model).

In addition to the similarity noted previously, low-speed flows over a rearward-facing step and over a flat-plate airfoil with blunt trailing edge at angle-of-attack are also related, due to the nature of the separated-flow regions associated with each. A region of separated flow is situated on the leeward surface of the flat-plate airfoil with two-dimensional blunt trailing edge at angle-of-attack that is similar in nature to the separated-flow region downstream of a two-dimensional rearward-facing step. Similarly, low-speed flow over a swept wing with blunt trailing edge at angle-of-attack would result in a three-dimensional separated-flow region on the leeward side of the wing similar to the region of separated flow that exists downstream of a swept rearward-facing step. In addition, the wake of the swept wing with blunt trailing edge would be similar in nature to the base flow associated with a flat plate airfoil with swept base.

There are many configurations of importance which contain regions of separated flows, such as the location of sudden increase in area in a channel, airfoils at large angles of attack, wide-angle diffusers, etc. For reasons of simplicity, most research efforts have concentrated on studying two-dimensional rearward-facing-step flow. The backward-facing-step flow configuration provides a simple example of the phenomena of separation, recirculation, reattachment, and subsequent relaxation of the shear layer since: a) the separation point is fixed and b) flow leaves the boundary at zero angle of separation. In many flows of practical interest, separation of a boundary layer and subsequent reattachment of the separated layer to a solid surface is unavoidable. For example, such flows occur in nuclear reactors, gas turbines, electronic circuitry, and heat transfer devices. Thus, the rearward-facing step is a practical, as well as frequently occurring, flow geometry.

1.2 Previous Studies

1.2.1 Flow over an Airfoil with a Thick Trailing Edge

For several years, there has been increasing interest in airfoil profiles with thick trailing edges, since they may have a smaller pressure drag at transonic and supersonic velocities than normal profiles with a sharp trailing edge (Tanner [3]). Poole and Teeling [4] studied the lift characteristics of two types of low-speed, blunt trailing-edge airfoils suitable for light transport aircraft and found improved performance when compared with similar sharp trailing-edge airfoils. The two new airfoils tested had a maximum thickness/chord ratios of 10% and 21% and were designed to achieve improved high lift and low drag by exploiting considerable aft loading via blunt trailing-edges. Their testing was carried out in the Mach number range of 0.15 to 0.45 ($Re_c = 2\times10^6$ to 2×10^7) which was relevant to light transport aircraft.

Perhaps the best known work on the subject of blunt trailing-edge airfoils has been by Chapman [5, 6]. Chapman [5, 6] and Chapman and Kester [7] have pointed out that a supersonic wing section with a blunt trailing edge could make possible a decrease in the section wave drag. In some cases, the decrease in wave drag was sufficient to offset the base drag penalty. The higher structural integrity of wings with blunt trailing edge was an additional advantage.

Other contributions to blunt trailing-edge airfoil research can be found in the work of Holder [8] and Nash [9]. Holder discussed the advantages of thickened trailing edges for transonic airfoils in general and indicated that the purpose of using a thick trailing edge is to reduce the strength of the shock on the upper airfoil surface in order to delay the onset of drag rise.

A profile with a blunt trailing edge has high base drag at subsonic velocities and therefore the total drag is considerably higher than that for a sharp trailing-edge airfoil. This arises mainly from the periodic vortex shedding which produces low pressure in the near-wake region. To reduce the base drag, periodic vortex shedding must be suppressed. In steady separated flow (as in the case of flow over a rearward-facing step), however, the base drag can still be large. Therefore, it would be desirable to increase the base pressure over its value associated with "normal" steady conditions. Methods listed by Hefner and Bushnell [10] which apply specifically to reducing base drag are:

1) boat tailing (reduces adverse pressure gradient),

2) concave surface curvature (generates longitudinal vortices),

3) splitter plates (reduces occurrence of Karman vortex street),

4) base bleed (energizes shear layer),

5) solid and ventilated base cavity (may produce splitter-plate effect) and

6) serrated base cavity (may introduce longitudinal vortices).

A few of these techniques are illustrated in figure 1.1.

Perhaps the oldest and best-known methods of influencing periodic vortex shedding at the base are the splitter plate and base bleed. The first important investigation of the effect of a thin plate (splitter plate) placed in the symmetry plane of a subsonic two-dimensional wake on the drag and pressure distribution of the body was that of Roshko [11] using cylinders. His measurements were carried out in the incompressible flow regime with a Reynolds number, based on the cylinder diameter, of 14,500. The results of his tests showed a 63% reduction in the pressure drag of a cylinder when using a splitter plate. This was attributed to the suppressing effect of a splitter plate on the vortex shedding process. The effect of mass injection from the trailing edge at low speeds has been investigated by Wood [12] and Bearman [13, 14] at low speeds and more recently in transonic flow by Motallebi and Norburg [15]. These studies found that for sufficient mass injection rates, the near-wake flow through the introduction of high momentum fluid, was stabilized and base drag was thereby reduced.

Apparently, the first use of base cavities for drag reduction was made by Osborne and Pearcey in 1960. Although their work was unpublished, Nash [9] reported that they obtained a 31% increase in the base pressure coefficient using a solid-walled cavity 1.7 base-heights deep, in a two-dimensional blunt-base airfoil. They also tested "ventilated" cavities, generally referred to as promoting "automatic bleed", by perforating the walls of the cavity or cutting streamwise slits in the walls. These modifications produced a maximum increase of 54% in the base-pressure coefficient. Nash, et al. [16] tested a thick-walled rectangular-cavity configuration at subsonic and transonic speeds and found similar results. Pollock [17] also tested several segmented cavity configurations and found configurations which produced drag reduction on the order of 50%-60% by creating a discontinuous base geometry and suppressing vortex shedding. His measurements on a two-dimensional blunt trailing-edge, flat plate models (with a profile having an elliptical leading edge) were in the Mach number range of 0.5 to 1.2 ($Re_c = 6.4\times10^5$).

The effect of trailing-edge geometry on base-drag reduction was studied experimentally by Gai and Sharma [18]. They tested a two-dimensional airfoil with an elliptic forebody and parallel upper and lower surfaces (thickness/chord ratio of 10%) at a free-stream velocity of 25 m/sec. ($Re_c = 1.5\times10^5$). Six configurations for base geometry were tested and reported base pressure recovery varied from about 22% to 58%. Sharma [19] also investigated the characteristics of the wake flow for airfoils with blunt castellated trailing edges having different geometrical cutouts along the span, using the model and test conditions just described. He reported that the wakes generated from the castellated blunt trailing edges exhibited a tendency for transverse growth in nearly the same manner as that of a plane wake when analyzed in terms of the velocity and length scales. Similarity in the shape of mean velocity profiles depended on the degree of three dimensionality in the wake and developed very slowly far downstream.

The effect of yaw and incidence on the base drag of wings with plain and castellated blunt trailing edges was examined by Sharma [20]. A rectangular wing with a symmetric airfoil section having semielliptic nose and thickness/chord ratio of 10% was used as the test model. Tests were conducted at a free-stream velocity of 22.5 m/s. Reynolds number based on base height was 1.5×10^4. Yaw angles in the range of 0° to 36° and angles of attack of 0° to 12° were examined for both two-dimensional and finite wings. The efficiency of castellations in reducing base drag was found to be maximum only at 0° yaw and 0° incidence and was reduced to about half of that value near the aerodynamic optimum combination of incidence and yaw.

Other researchers have studied vortex shedding from blunt trailing-edge airfoils in order to find methods for reducing turbomachinery noise. Most of the vibration and noise which occurs in fluid mechanics are induced by velocity fluctuations around machine elements such as blades of turbomachines, the exhaust of jet engines, combustion chambers, etc. Tamura et al. [21] investigated vortex shedding from a blunt trailing-edge airfoil with unequal free-stream flow speeds (over the upper and lower model surfaces) in order to reduce noise from turbomachinery and jet engines. Their experiments were conducted in the Reynolds number range of 190–3000 based on the trailing edge thickness. The Re-St relationship was reported to be insensitive to upper-to-lower surface velocity ratios of greater than 0.78.

Boldman et al. [22] conducted similar tests to examine the vortex shedding process. They conducted their experiments at a free–stream speed of 24.4 m/s using the smoke flow-visualization technique and compared theoretical calculations of the vortex formation (based on an incompressible inviscid model of the vortex street) to their test results. A close agreement of their measurements of vortex formation and theoretical predictions was reported.

1.2.2 Flow over a Rearward-Facing Step

The effects of flows with separation regions on engineering equipment has been stressed in many publications e.g., Abbot and Kline [23], Seban [24], and Goldstein et al. [25], and attempts have been made to develop advanced experimental and theoretical techniques in order to carefully study such flows (e.g., Durst and Whitelaw [26], Gosman and Pun [27], and Kumar and Yajnik [28]).

Sinha et al. [29] conducted a detailed study of laminar separating flow over backsteps. Those tests were carried out at a free-stream speed of 1.8 m/s and utilized smoke-flow visualization, static pressure, and hot-wire measurement techniques in the Reynolds number range of 100–12,500. They reported reattachment length as a function of Reynolds number, momentum thickness in the transition region, and intensity of fluctuations, along with the mean velocity profile, for a laminar shear layer undergoing transition over a backward step.

Gai and Sharma [30] investigated the effect of a discontinuous separation line on the pressure distribution and reattachment region downstream of a rearward-facing step and reported that 3–D disturbances in the separating shear layer diminished rapidly and the flow downstream of reattachment appeared to have a two-dimensional global shear layer. The experiments were carried out at a free-stream speed of 27 m/s and the Reynolds number based on step height was 1.1×10^4.

Armaly et al. [31] used a LDV technique to measure velocity distribution and reattachment length downstream of a two-dimensional rearward-facing step for laminar, transitional, and turbulent flow in the Reynolds number range of $70 < Re < 8{,}000$. Their work also included a comparison of their experimental measurements with predictions from a numerical analysis of backward-facing step flow. Close agreement of the numerical predictions with experimental measurements was observed when the flow maintained its two-dimensionality in the experiments, i.e. at low and high Reynolds numbers. Their work suggested a dependence of reattachment length on the Reynolds number and expansion ratio.

Heat-transfer characteristics of the flow over a rearward-facing step were investigated numerically by Sparrow and Chuck [32] for a Reynolds number of 200 (based on step height). The local Nusselt number variation with the Reynolds number was reported to take on different forms at various axial distances from the step base. In the thermally developed regime, the Nusselt number was independent of the Reynolds number.

Aung and Goldstein [33] performed a similar experimental low speed (4.5 m/sec) turbulent-flow study using a Mach-Zehnder interferometer. Their results confirmed that the Reynolds analogy does not hold in a separated-flow region and that the point of minimum shear stress at the reattachment point corresponds to the maximum heat-transfer location. Further results of their tests led to refutation of a previous theory, that the region of reverse flow is essentially a "dead air" region and therefore of constant enthalpy, by showing significant temperature variations in that region.

Troutt et al. [34] experimentally studied spanwise structures in a two-dimensional low-speed turbulent reattaching separated flow associated with a rearward-facing step. Their measurements indicated the existence of large-scale vortices in both the separated and reattached regions of this flow. The reduction of turbulence energy in the reattachment region and the slow transition of the mean flow downstream of reattachment to free-stream conditions were attributed to effects associated with these vortices.

Turbulent subsonic flow over single and double backward-facing steps was studied by Abbott and Kline [23]. They used a water table for their tests, employing a dye injection flow visualization technique and hot-wire anemometry. Contrary to the more recent findings of Armaly et al. [31], they found no effect of Reynolds number (in the range of 2×10^4 to 5×10^4 based on test-section height) and turbulence intensity on flow pattern or reattachment length. Furthermore, they determined that three zones of flow exist in turbulent separation: (I) A three-dimensional zone found immediately downstream of the step face and characterized by one or more vortices rotating about an axis normal to the streamwise direction; (II) a two-dimensional zone downstream of zone (I) which contains the classical stall pattern of flow moving upstream along the wall and downstream adjacent to the through-flow; and (III) a time-dependent tail region which is periodically changing in size. Based on mean velocity surveys, it was also concluded that flow is not two-dimensional near the reattachment point.

Adams and Johnston [35] studied the flow structure in the thin reversed-flow layer within a recirculation zone for the case of turbulent low-speed reattaching flow behind a backward-facing step (Re_h = 36,000) using Laser-Doppler and hot-wire anemometry techniques. They examined the structure of the near-wall region of the separated flow and compared it to the characteristics of a normal turbulent boundary layer. They suggested that the structures were different and that the structure of the flow in the near-wall region was a combination of the features of the large eddies above the near-wall region and the damping effect of the wall. They also conducted another study [36] to explain the scatter in existing data sets regarding the length of the reattachment zone for two-dimensional rearward-facing step flows and the effect of initial shear-layer structure those flows. They conducted their tests in the Reynolds number range of $8{,}000 < Re_h < 40{,}000$ for laminar and turbulent flows using the previously described techniques. A strong effect of boundary-layer state on the reattachment length and skin friction values within the separated zone was reported at high Reynolds numbers.

Generally, results indicate that pressure on the base of a rearward-facing step is difficult to alter for a wide range of geometric modifications made to models.

However, it is desirable in most applications to increase the base pressure for drag reduction purposes. Often, flow alterations result in a decrease in the base pressure.

1.2.3 Vortex-Generating Devices

Presently, there is considerable interest in exploring new methods of reducing various sources of drag with a view toward improving the aerodynamic efficiency of flight vehicles. As in any research, the kernel problem for drag reduction is the genesis and development of new approaches, techniques, insights, and understanding.

Vortex generating devices have long been known to increase mixing between external streams and separated boundary layers (Chang [37]). Axial vortex generators such as fins, troughs, and grooves have been used to achieve separation delay by energizing the boundary layer to overcome the adverse-pressure-gradient effects (Lin et al. [38]). Circumferential grooves have also been tested on an axisymmetric body and found to provide on the order of a 50% net body drag reduction through a series of flow separations and reattachments over the grooved surface (Howard et al. [39]). Associated drag measurements on their axisymmetric bodies in subsonic incompressible flow have shown that these transverse grooves are more effective than longitudinal V-grooves in reducing the drag of the afterbody [40].

1.3 Scope of Present Work

The present research program was performed in order to identify effective passive devices for controlling of two- and three-dimensional turbulent subsonic separated and wake flows and an understanding of the flow mechanisms associated with these devices. An understanding of the flow physics related to the interaction of the subject devices with the flows studied could result in enhancement of device effectiveness. This knowledge was obtained by experimentally examining the flow over swept and unswept rearward-facing steps and flat-plate airfoil models with swept and unswept trailing edges as affected by various passive flow control devices such as:

1) longitudinal V-grooves,

2) wishbones,

3) doublets,

4) base serrations, and

5) base fences.

V-grooves of varying angle, length, and depth; Wheeler wishbone and doublet vortex generators of varying size; and base serrations and fences of varying geometry were tested. Measurements of base and surface pressure, flow reattachment distance, wake velocity profile, vortex, and surface temperature were made using the oil-drop flow-visualization technique, pitot-probe surveys, constant-temperature hot-wire anemometers, and infrared surface imaging.

All tests were conducted in the 91 cm$\times$122 cm ($3' \times 4'$) test section of the Old Dominion University low-speed closed-circuit wind tunnel. In the process of performing the present experiments, various wind-tunnel models were fabricated, the data acquisition system of the wind tunnel was developed and improved and as testing progressed, several user-friendly data acquisition computer programs for performing different measurement tasks were developed and a sample program is included herein in an appendix.

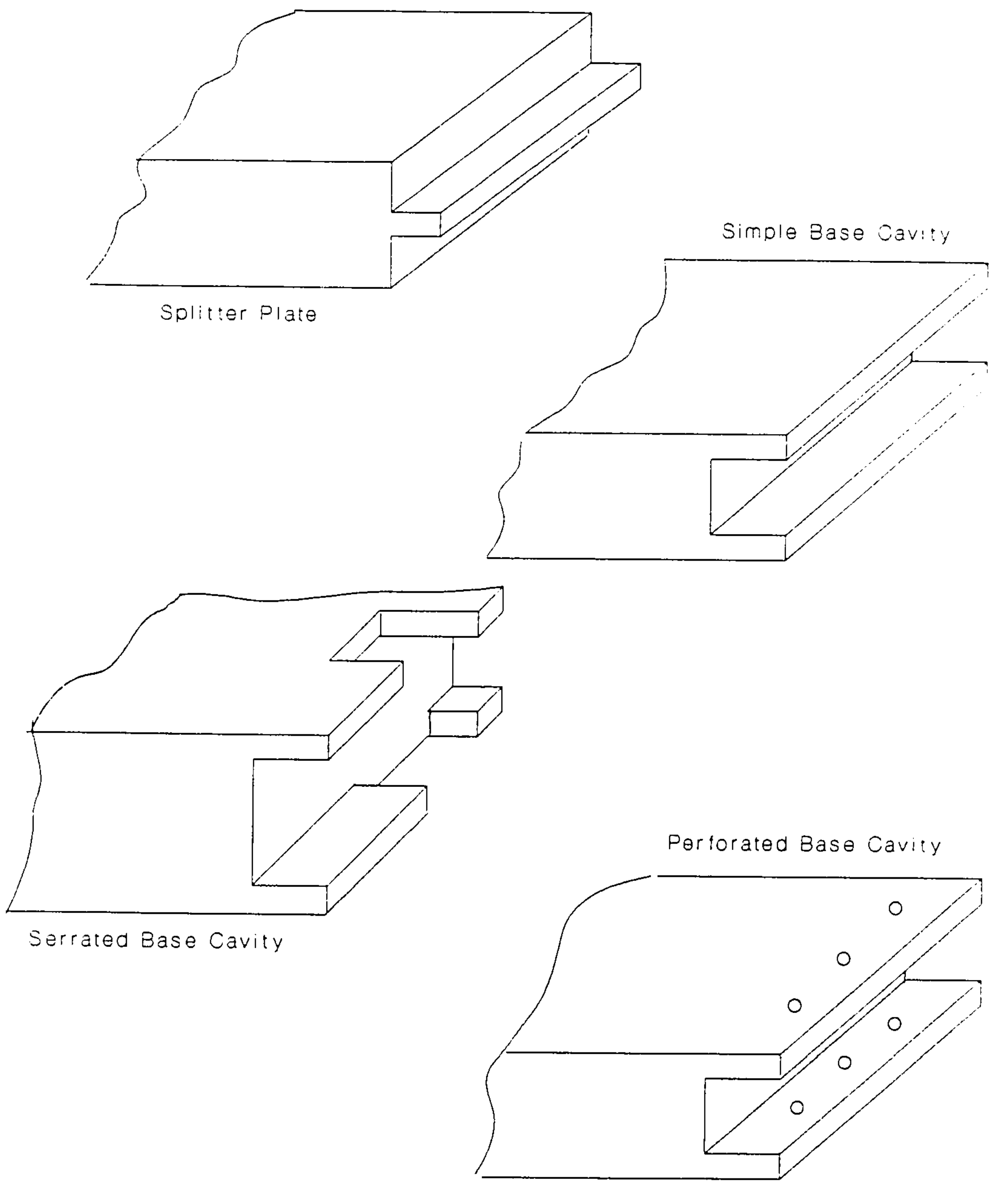

Fig. 1.1 Devices for increasing base pressure at subsonic speeds

Chapter 2

EXPERIMENTAL FACILITY, MODEL DESCRIPTION, AND TEST PROCEDURE

2.1 Wind Tunnel Facility

The present research was conducted in the Old Dominion University closed-circuit, low-speed wind tunnel. The layout of this tunnel is shown in figure 2.1. The wind tunnel, manufactured by Aerolab Supply Company (Hyattsville, MD), has two test-sections with 1.2 m×0.9 m and 2.1 m×2.4 m cross-sections. This study was completed using the 1.2 m×0.9 m (2.4 m long) test section. The tunnel utilizes an axial fan powered by a 125 hp electric motor to move the air. Maximum speed in the high speed test-section is 49 m/sec. At 43 m/sec, the wind tunnel turbulence intensity in this test-section was measured to be about 0.7%, using a single-element constant-temperature hot-wire anemometer. The tunnel air speed was initially designed to be controlled by a set of adjustable louvre control vanes where power supplied to the motor varied linearly with air speed. In the absence of a temperature control system, this posed thermal problems. The free-stream air static temperature rise over the duration of several tests was significant (25° C increase in 3 hrs). Consequently, a new fan speed control system was acquired which limits the power input to the electric motor through frequency control and creates more gradual thermal changes because of the reduced rate of energy dissipation by the wind tunnel air at lower speeds.

A remote-controlled three-axis traverse mechanism with digital readout (0.025 mm resolution, 0.5% reading error) is in place in the 1.2m×0.9m test-section for pressure and velocity surveys. This system has a maximum traverse speed of

0.37 m/min. and 0.22 m/min. in the vertical and streamwise directions, respectively.

The semi-automatic data acquisition system for the wind tunnel consists of a personal computer (Compaq: Deskpro 286, 12 MHz), a digital oscilloscope (Nicolet: Explorer III-206), and a programmable multimeter (Fluke: 8520A). A General Purpose Interface Bus (GPIB-PC) is used for communication between these devices. A differential pressure transducer (MKS Baratron: 310CD-000010) with 20 torr range and 0.08% reading accuracy was used for pressure measurements. Tunnel air temperature was measured using a type-T copper-constantan thermocouple and a digital thermocouple thermometer (Fluke: 2176A). Details of the uncertainty analysis for measurements in the present study are presented in Appendix C.

An infrared imaging system capable of providing 25 fields per second was used to provide temperature maps of the surface of the model downstream of the two-dimensional step. The nucleus of the IR imaging system was an AGA Thermovision-782 camera equipped with a $20^\circ \times 20^\circ$ lens, coated for optimal response in the shortwave infrared spectrum. The system, at a distance of 0.5 m, has a field-of-view of 15 cm$\times$15 cm which imposed a constraint on the dimensions of the test model. To optimize the performance of the IR imaging system, the surfaces of the model were painted flat black to maintain a uniform surface emittance.

2.2 Test Setup and Measurements

2.2.1 Rearward-Facing Steps

2.2.1.1 2–D Rearward-Facing Steps Oil-drop flow visualizations and surface pressure measurements were performed using the rearward-facing step model shown in figure 2.2. A sketch of the end view of the model with its support walls is shown in figure 2.3. The objective of the first series of tests was to measure base and surface pressures. The second series of tests were conducted to determine the flow reattachment distance using the oil-drop flow-visualization technique. A total of 77 pressure taps (D = 1.0 mm) were incorporated in the model design. Sixty-three were utilized to measure the pressure at the base of the step and on the surface of the model. Twenty-five of these pressure taps were along the step base centerline. The remaining taps were used to record the pressure on the surface of the model upstream and downstream of the step. Arrangement of the surface pressure taps is shown in figure 2.4.

The effect of fourteen different passive modifications to this model were studied. Table 2.1 is a list of the various modifications made to the model. V-grooves of six different dimensions were tested. (See figure 2.5 for a definition of pertinent groove parameters.) Two rectangular groove geometries were also tested. These grooves had the same groove cross-sectional areas as the V-grooves with α = 50° and d = 6.4 mm. This particular groove configuration was chosen to study the effect of groove geometry on the base pressure. All modifications to the model surface upstream of the step involving grooves included 13 grooves of 25.4 cm length and 2.5 cm spacing.

The effect of two types of vortex-generating devices, Wheeler wishbones and Wheeler doublets, were examined [41, 42]. Fourteen vortex-generating devices spaced 2.5 cm apart were used. (See figures 2.6 and 2.7)

Other modifications included a 2.5 cm deep base cavity and 2.5 cm long triangular serrations attached to the base. (See figure 2.6)

A trip wire (D = 1.02 mm) placed at 5 cm downstream of the model leading-edge (5.6% of the chord) was used to promote an early transition to turbulent boundary layer flow. Free-stream velocity was measured by recording the output of a pitot-static tube located 40.6 cm (45.7% of the chord) downstream of the leading-edge, 10 cm above the model surface. The pitot-static tube was attached to the model sidewall, protruding 10 cm out from the sidewall. Tests were conducted at a free-stream speed of approximately 43 m/sec. All measured pressures were referenced to the free-stream static pressure. All pressure lines from the model were connected via flexible tubing to a scanivalve whose output in turn was connected to a pressure transducer. The instrumentation arrangement for pressure measurements is shown in figure 2.8. Wind-tunnel air temperature variation throughout the testing period was measured using a copper-constantan thermocouple inserted in the free-stream.

For determining flow reattachment distances, a section of the model downstream of the step was slightly modified. This 381 mm$\times$406 mm section was painted glossy white and a 203 mm$\times$152 mm mesh was drawn on its surface as shown in figure 2.9. A mixture of linseed oil and black linseed oil-based artist's paint was prepared. Proportions of the ingredients in the mixture were varied until an appropriate viscosity was obtained. Prior to each run, the surface of the painted section was coated with a thin layer of linseed oil and approximately 3 mm diameter drops of the mixture were placed on the mesh using a medicine dropper. A maximum of ten rows of the drops with a spacing of 13 mm in the crossflow direction were placed on the mesh. All flow reattachment tests were conducted at a free-stream speed of 43 m/sec. At the end of each run, based on the surface streamline patterns formed by the oil drops, reattachment distance was measured and the oil-flow pattern photographed for later analysis. Several runs were made for each model tested to increase the certainty of the measurements. All configurations for which surface pressure and flow visualization data were acquired are listed in table 2.1.

An additional two-dimensional rearward-facing step model was constructed to examine the effect of V-grooves on the heat transfer rate downstream of the step. The infrared imaging system described previously was used to record temperature contours on the model in the region of interest. The two-dimensional rearward-facing step model used for the heat transfer tests consisted of a 16 cm wide by 91 cm long flat plate (partitioned at mid-span with a plexiglass plate), with a step positioned at 61 cm downstream of the leading edge. Bisection of the model surface allowed simultaneous testing of grooved and non-grooved surfaces, as shown in figure 2.10. Comparisons of temperature data obtained from the infrared images of the model surfaces on both sides of the partition were validated with this arrangement.

Prior to the start of each heat-transfer test, a temperature difference was created between the surface (aluminum) of the model downstream of the step and the warmer tunnel air (24–28 C) by circulating water at 5°C through the internal flow channels machined in it. Model surface temperature was monitored using surface-embedded thermocouples. When the surface temperature became uniform, water circulation was stopped and the testing started. The model surface upstream of the step on one side of the partition was fitted with 25 cm long V-grooves (α = 50°, d = 6.4 mm) as shown in figure 2.10. A trip wire (D = 1.5 mm) was attached to the model surface 5 cm downstream of the leading edge to promote early transition to turbulent flow. To ensure a more two-dimensional flow over the step, two 30 cm high$\times$91 cm long sidewalls were attached to the model. A pitot-static tube placed 7.6 cm upstream of the model was used to measure air speed. A velocity survey of the boundary layer at 2.5 cm upstream of the step indicated a fully-developed turbulent boundary layer. The measured boundary-layer thickness at that position was 2.25 cm. A spanwise velocity survey over the middle 50% of the span at the same longitudinal location indicated uniform flow conditions (less than 0.5% variation).

2.2.1.2 Swept Rearward-Facing Step Rearward-facing steps with step sweep angles of 30° and 45° were tested at a free-stream speed of 43 m/sec. Schematic drawings of the models are shown in figures 2.11 and 2.12. Tests involved the measurement of base and surface pressures as well as flow reattachment distance. Similar to the unswept model, a total of twenty-five pressure taps along the centerline of the step base were incorporated in the design of the model for base pressure measurements. Pressure taps were also provided on the model surface upstream and downstream of the step. The relative positioning of these pressure taps for each model is shown in figures 2.11 and 2.12. The instrumentation layout for these tests was the same as that for the tests on the two-dimensional rearward-facing step model.

Longitudinal surface grooves of 76 mm length and 25.4 mm spanwise spacing were used for the grooved-step tests. This spacing allowed the use of 13 grooves on the surface of the model leading to the step. Two different types of vortex generating devices, doublets (h_w = 3.8 mm) and wishbones (h_w = 6.4 mm), were tested with 25.4 mm spanwise spacing. Wishbones were tested in two different orientations, with apex facing the upstream direction (hereafter referred to as reversed orientation), as well as the downstream direction. Two different sizes of right-triangular fences (25 mm high×152 mm long and 25 mm high×51 mm long) were tested with variable spacing. These fences were placed at the downstream side of the step and oriented in the flow direction. Sketches of the fences and serrations tested are shown in figure 2.13. Various modifications to the swept rearward-facing step models for pressure measurements are summarized in tables 2.2 and 2.3.

Flow reattachment distance was determined using the previously described oil-drop flow-visualization technique. Grid lines were drawn on the model surface downstream of the step as shown in figure 2.14. A summary of the modifications to each swept-step model for these tests is also given in tables 2.2 and 2.3. Each model was tested twice at a free-stream speed of 43 m/sec in order to increase the certainty of the measurements. A photographic recording of the flow pattern left on the model surface was used to determine the reattachment line.

2.2.2 Flat-Plate Airfoil

2.2.2.1 2–D Flat-Plate Airfoil A schematic drawing of the flat-plate airfoil with an elliptic leading-edge and 2.5 cm thick blunt trailing edge is shown in figure 2.5 (with V-grooves). Pressure taps were incorporated in the design of the model for base and surface pressure measurements as discussed previously — the same models were used for the rearward-facing step and flat-plate airfoil measurements. The surface downstream of the step was removed for the airfoil wake studies.

Tests were conducted on the model to examine the effect of longitudinal V-grooves of varying groove angle and depth on base pressure and vortex shedding frequency in the incompressible subsonic flow regime. Hot-wire anemometry technique were also used to examine the flow in, around, and downstream of the V-grooves for qualitative flow details. A list of the V-grooves of various dimensions that were tested is given in table 2.4. Grooves were tested for angle effect and groove-depth effect at free-stream speeds of 17 and 43 m/sec.

Matched boundary-layer trip wires (D = 1.02 mm, length = 38.1 cm) were placed at the 5.6% chord location on the upper and lower airfoil surfaces to render the boundary-layer flow turbulent. At 2.5 cm upstream of the trailing edge, boundary-layer velocity profiles were measured at three spanwise positions for both the upper and lower model surfaces. (See figures A.5 to A.10 in Appendix A.) Turbulent boundary layer thickness at 43 m/sec at midspan, 2.5 cm upstream of the trailing edge was measured to be 18 mm.

All measured surface pressures were referenced to the upper-surface free-stream static pressure. Free-stream flow speed was measured using two pitot-static probes located 41 cm downstream of the model leading-edge in the free-streams of the upper and lower model surfaces.

Vortex-shedding frequency measurements were conducted for various groove modifications to the model. Tests were directed at examining the effect of groove geometry on vortex-shedding frequency. The constant-temperature hot wire anemometer system described previously, was utilized to record the velocity fluctuations in the wake of the model. The hot-wire probe was positioned 2.5 cm downstream of the trailing-edge at midspan to record the signal. The output of the anemometer was recorded using the Nicolet digital oscilloscope. The oscilloscope sample internal was 200 μsec/point (sample size = 4096) which was determined to be suitable for capturing shedding frequencies of less than 500 Hz and still provide sufficient record length for adequate resolution in the measured frequency [43]. Fast-Fourier transformation of the digitized signal and subsequent computation of the energy spectrum yielded the dominant frequency. Calculation of the flow Strouhal number (St) was based on the spectral peak frequency and utilized the model effective base thickness as the reference length. Layout of the instrumentation for vortex-shedding frequency tests is depicted schematically in figure 2.15.

Initial pressure measurements with V-grooves were conducted with the model supported by sidewalls extending from the leading edge of the model to the trailing edge. (See Table 2.4) To isolate the flow in the wake of the model from end effects, the sidewalls and the top and bottom plates of the model supports were extended 41cm beyond the trailing-edge of the model. Additional pressure measurements with vortex generators, base cavity, triangular serrations, and V-grooves were conducted on the unswept model with extended walls. Table 2.5 is a summary of the modifications made to this model. Tests with V-grooves included 13 longitudinal grooves of 25.4 cm length and 2.5 cm spacing on each surface. As mentioned previously, two types of vortex generators, wishbones and doublets were tested. Thirteen of the devices, spaced 2.5 cm apart, were attached to each surface at the trailing edge. Triangular serrations (lengths of 1.3 cm and 2.5 cm) and base cavities (1.3 cm and 2.5 cm depth; 2.2 cm height) were also tested.

2.2.2.2 Flat-Plate Airfoil with Swept Trailing Edge Two models with base sweep angles of 30° and 45° were designed, fabricated, and tested to study the effect of aforesaid modifications on the base flow. Figures 2.16 and 2.17 are schematic drawings of these models. On each model, ten pressure taps in two rows were provided on the top and bottom surfaces for surface pressure measurements. Twenty-three pressure taps for the measurement of base pressure were incorporated in the design of each model. These taps were located along the centerline of the base. Models were supported by two plexiglass sidewalls (89 cm high×132 cm long; extended walls). Flow over the top and bottom surfaces of the model was further isolated from test-section walls by attaching two (38 cm wide×132 cm long) plexiglass plates 36 cm from each surface.

Free-stream speed on the top and bottom surfaces was measured at 2.5 cm upstream and 41 cm downstream of the leading-edge. Trip wires, as in the previous models, were used to cause early transition to turbulent boundary layer flow. The wires were placed on the top and bottom surfaces at 5.1 cm downstream from the leading edge. Boundary-layer velocity profiles were measured at three locations in the crossflow direction, 2.5 cm upstream of the trailing-edge, on the top and bottom surfaces. (See figures A.11 to A.16 in Appendix A.) Turbulent boundary layer thickness (δ at 0.99 U_∞) 2.5 cm upstream from the trailing edge at midspan (at 43 m/s) was measured to be 18 mm for 30° and 45° swept base models. A pitot-static probe attached to the test-section traverse mechanism was used for the surveys. All tests were conducted at 43 m/sec.

A summary of the modifications made to the 30° and 45° models for base pressure tests are listed in tables 2.6 and 2.7. On the 30° models, wishbones were tested with different spacing and orientation. The longitudinal V-grooves (α = 50°) tested were 7.6 cm long and spaced 2.5 cm apart. Aluminum strips (2.5 cm wide and 1.6 mm thick) were used to cut out the triangular serrations tested. The two strips running the length of the base were attached to the upper and lower surfaces of the model at the base. The triangular fences were cut out of 1.6 mm thick aluminum sheets. For testing, they were attached to the model base, aligned with the flow direction, and spaced 2.5 cm apart. See figure 2.13 for serration and fence geometries.

Final tests on selected flat-plate airfoil models were conducted to determine the wake velocity-defect profiles. These profiles were used to estimate relative drag for some of the modifications. A pitot-static tube attached to the test-section traverse mechanism was used to record the flow dynamic head and static pressure variations at nine stations in the wake. (See figure 2.18) Wake surveys were conducted for the flat-plate airfoils with 0°, 30°, and 45° base sweep angles and the 30° model with wishbones and V-groove (α = 50°) modifications.

Table 2.1 Modifications to the 2–D rearward-facing step model for pressure and reattachment distance measurements

Modification	Pressure Tests	Flow Visualization
Baseline	X	X
V-grooves		
$\alpha = 10°$ (d = 6.4 mm)	X	
$\alpha = 20°$ (d = 6.4 mm)	X	
$\alpha = 30°$ (d = 6.4 mm)	X	X
$\alpha = 30°$ (d = 9.5 mm)	X	
$\alpha = 40°$ (d = 6.4 mm)	X	X
$\alpha = 50°$ (d = 6.4 mm)	X	X
Rectangular-grooves		
Deep (7.7 mm width x 6.4 mm deep)	X	X
Shallow (15.3 mm width x 3.2 mm deep)	X	
Wishbone vortex generators		
(h_w = 6.4 mm; 2.5 cm spacing)	X	X
Doublet vortex generators		
(h_w = 3.8 mm; 2.5 cm spacing)	X	X
Triangular serrations		
1.3 cm long (1.3 cm spacing)		
2.5 cm long (2.5 cm spacing)	X	X
Base cavity		
1.3 cm deep		
2.5 cm deep	X	X

Table 2.2 Modifications to the 30° swept rearward-facing step model for pressure and reattachment distance measurements

Modification	Pressure Tests	Flow Visualization
Baseline	X	X
V-groooves (α = 50° d = 6.4 mm)	X	X
Shallow rectangular grooves (15.3 mm×3.2 mm)	X	X
Doublet vortex generators (h_w = 3.8 mm; 2.5 cm spacing)	X	X
Wishbone vortex generators (h_w = 6.4 mm; 2.5 cm spacing)		
Apex facing downstream	X	X
Apex facing upstream (reversed)	X	X
Triangular Serrations (2.5 cm length; 2.5 cm spacing)	X	X
Triangular fences (5.1 cm long)		
Two placed at 1/3 and 2/3 span	X	X
Four equally spaced spanwise	X	X

Table 2.3 Modifications to the 45° swept rearward-facing step model for pressure and oil-drop flow-visualization measurements

Modification	Pressure Tests	Flow Visualization
Baseline	X	X
V-grooves (α = 50° D = 6.4 mm)	X	X
Wishbone vortex generators (h_w = 6.4 mm; 2.5 cm spacing)		
Apex pointing downstream	X	X
Apex pointing upstream (reversed)	X	X
Doublet vortex generators (h_w = 3.8 mm; 2.5 cm spacing)	X	X
Triangular Fences (four equally spaced spanwise)		
5.1 cm length	X	
15.2 cm length	X	X

Table 2.4 Dimensions of V-grooves for initial surface pressure measurements with the 2–D flat-plate airfoil model (13 grooves; 25.4 cm length; 2.5 cm spacing)

α	d, mm
10°	6.4
20°	6.4
30°	3.2
30°	4.8
30°	6.4
30°	7.8
30°	9.5
40°	6.4
50°	6.4

Table 2.5 Modifications to the 2–D flat-plate airfoil model with extended walls for pressure measurements and wake surveys

Modification	Pressure Measurements	Wake Surveys
Baseline	X	X
V-grooves:		
$\alpha = 30°$ (d = 6.4 mm)	X	
$\alpha = 30°$ (d = 8.0 mm)	X	
$\alpha = 50°$ (d = 6.4 mm)	X	
Rectangular grooves:		
(3.2 mm deep $\times$ 15 mm width)	X	X
Wishbone vortex generators:		
(2.5 cm spacing)		
h_w = 2.8 mm	X	
h_w = 6.4 mm	X	
Doublet vortex generators:		
(2.5 cm spacing)		
h_w = 2.8 mm	X	
h_w = 3.8 mm	X	
Triangular serrations:		
1.3 cm long (1.3 cm spacing)	X	
2.5 cm long (2.5 cm spacing)	X	
Base cavities:		
1.3 cm deep	X	
2.5 cm deep	X	

Table 2.6 Modifications to the flat-plate airfoil model with 30° swept base for pressure measurements and wake surveys

Modification	Pressure Measurements	Wake Surveys
Baseline	X	X
Doublet vortex generators (h_w = 3.8 mm; 2.5 cm spacing)	X	
Wishbone vortex generators (h_w = 6.4 mm; 2.5 cm spacing)		
2.5 cm spacing (reversed)	X	X
5.1 cm spacing	X	
V-grooves (α = 50°; d = 6.4 mm; 7.6 cm long)	X	X
Triangular serrations (2.5 cm long; 2.5 cm spacing)	X	
Triangular Fences (2.5 cm height; 5.1 cm long; 2.5 cm spacing)	X	

Table 2.7 Modifications to the flat-plate airfoil model with 45° swept base for pressure measurements and wake surveys

Modification	Pressure Measurements	Wake Surveys
Baseline	X	X
Wishbone vortex generators (h_w = 6.4 mm; 2.5 cm spacing;)	X	
V-grooves (α = 50°; D = 6.4 mm; 7.6 cm long)	X	
Triangular Fences (2.5 cm high; 5.1 cm long; 2.5 cm spacing)	X	

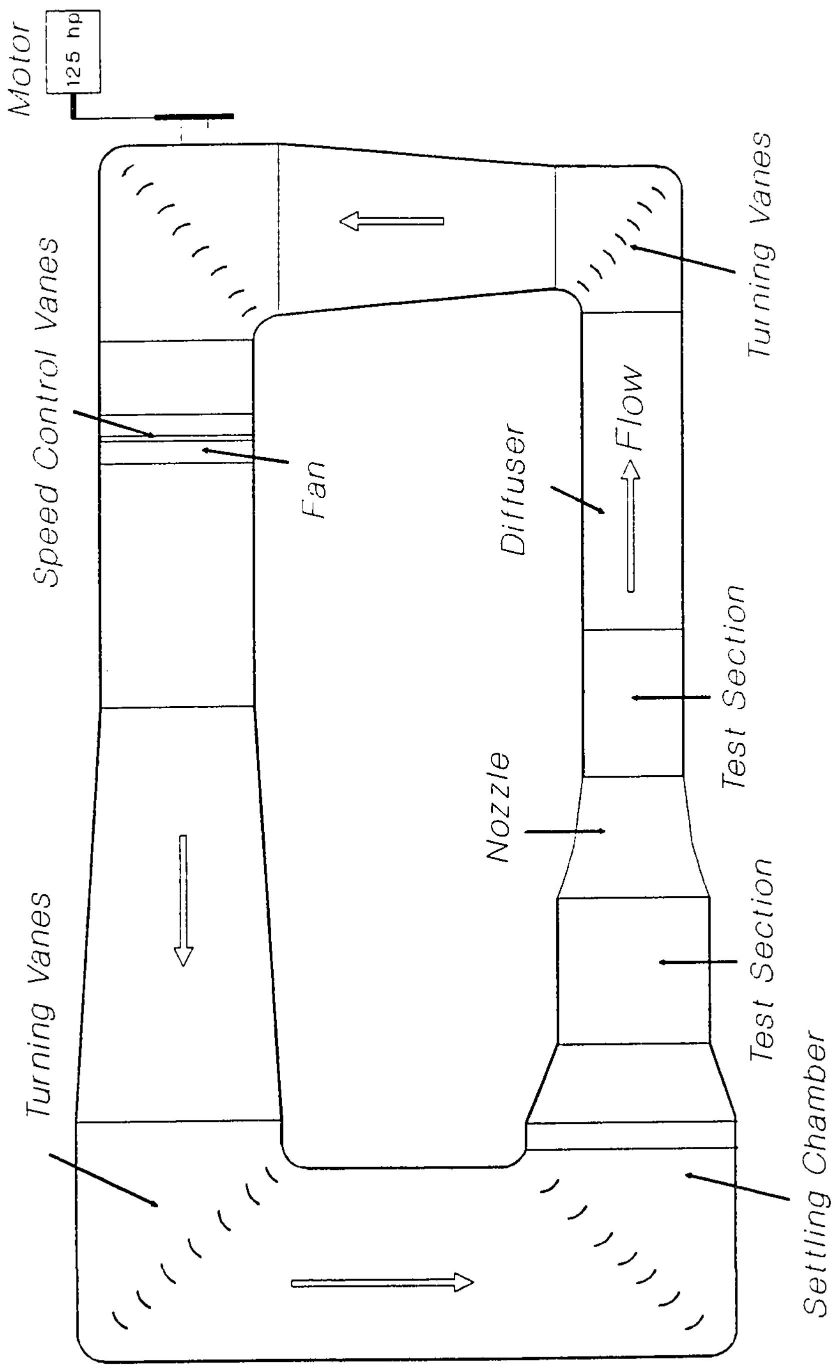

Fig. 2.1 Schematic of the Old Dominion University Low-Speed Wind Tunnel

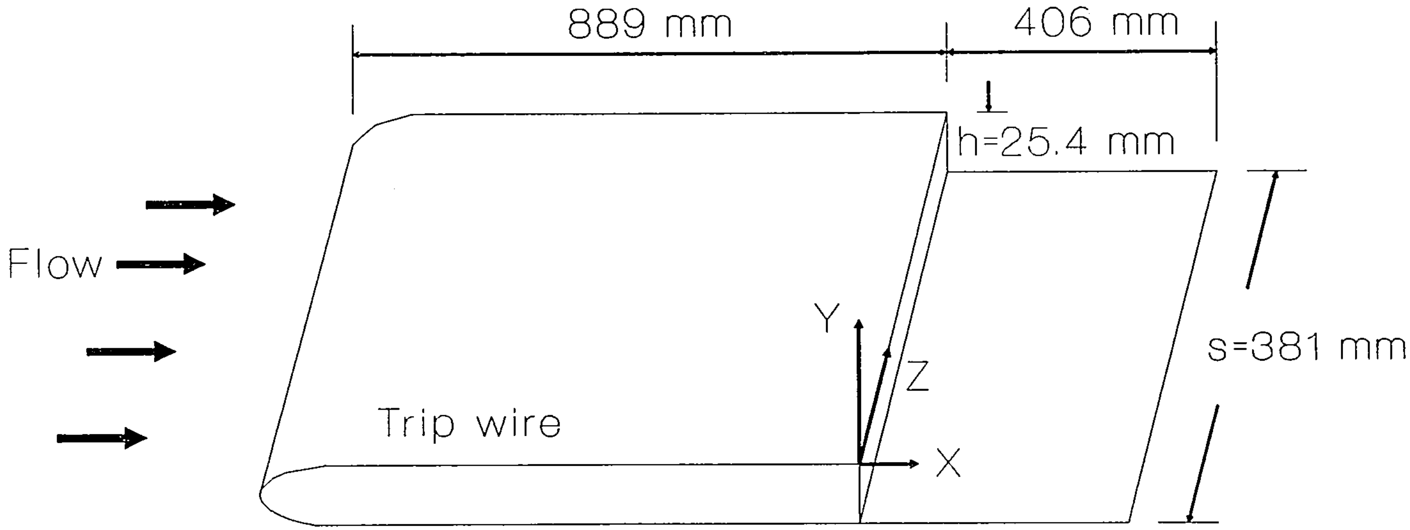

Fig. 2.2 Two-dimensional rearward-facing step model

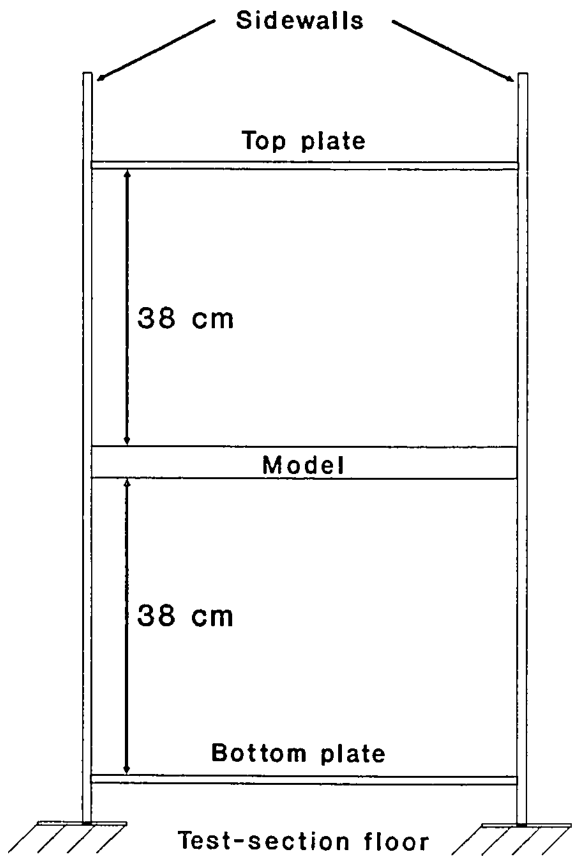

Fig. 2.3 End view of the model with its support walls

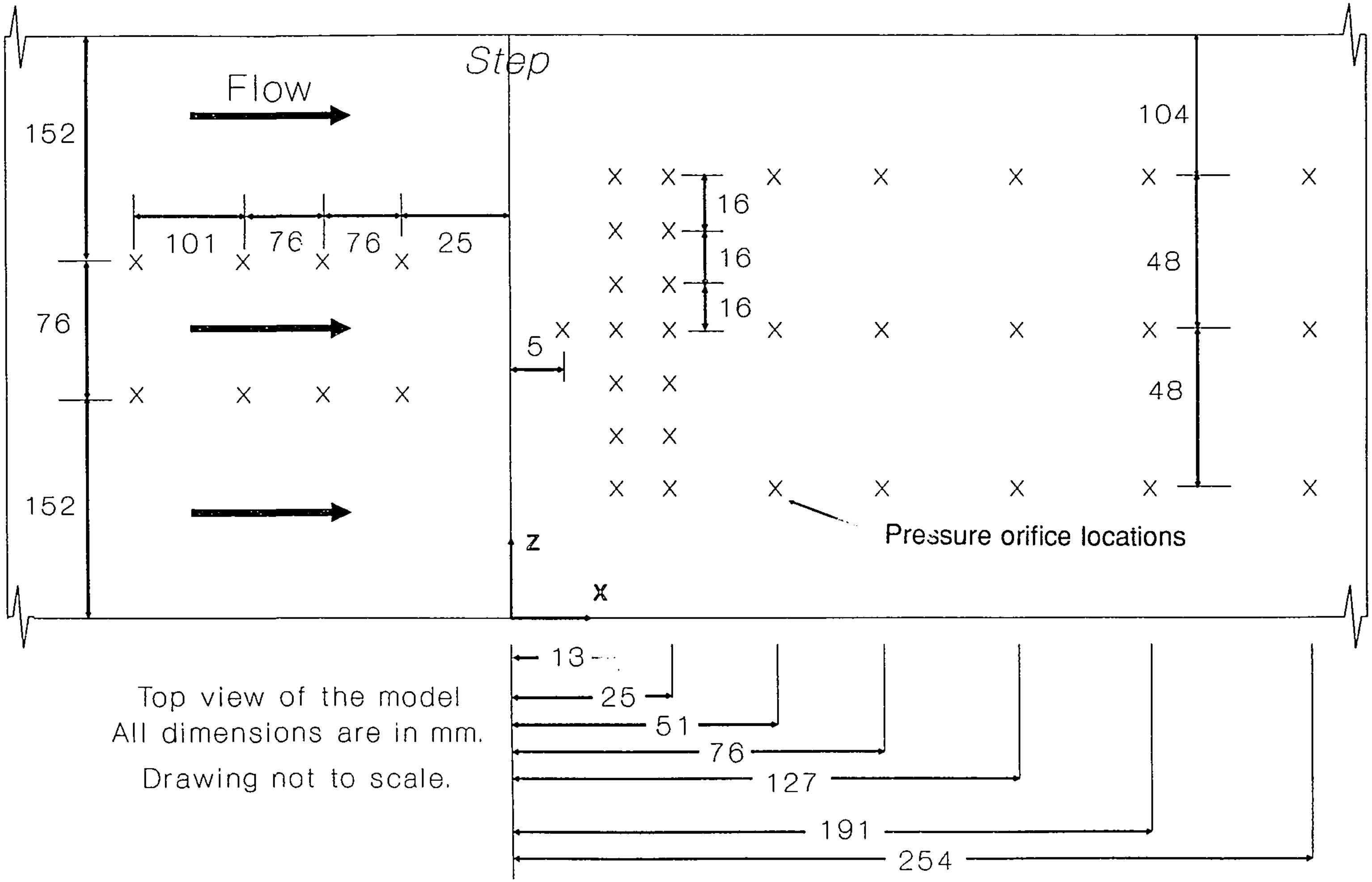

Fig. 2.4 Top view of the two-dimensional rearward-facing step model showing pressure orifice positions

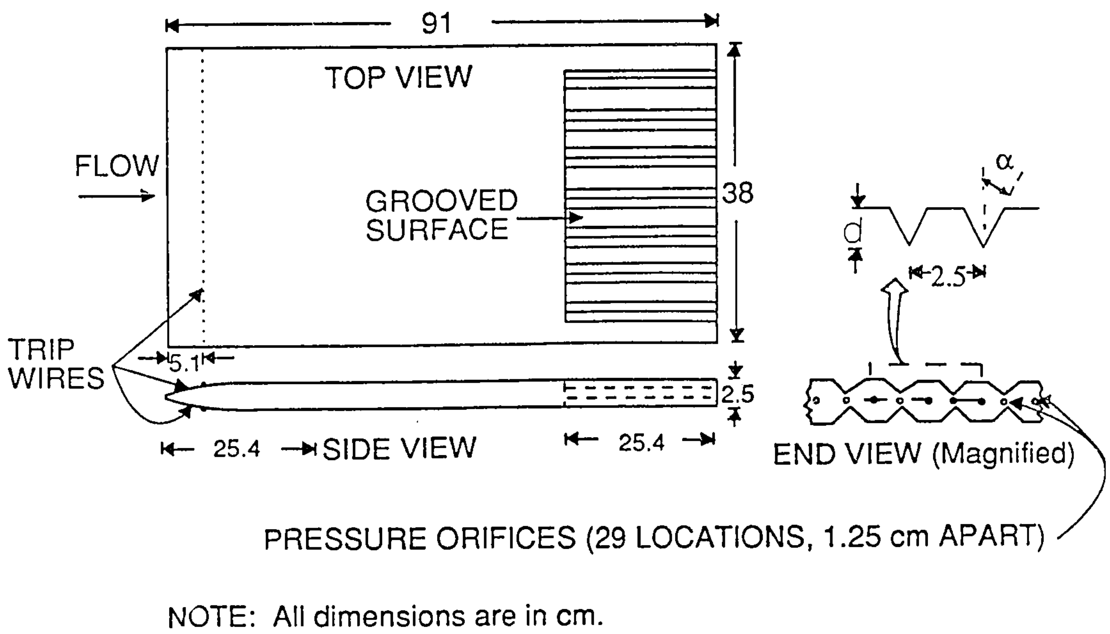

Fig. 2.5 Two-dimensional flat-plate airfoil model with longitudinal grooves

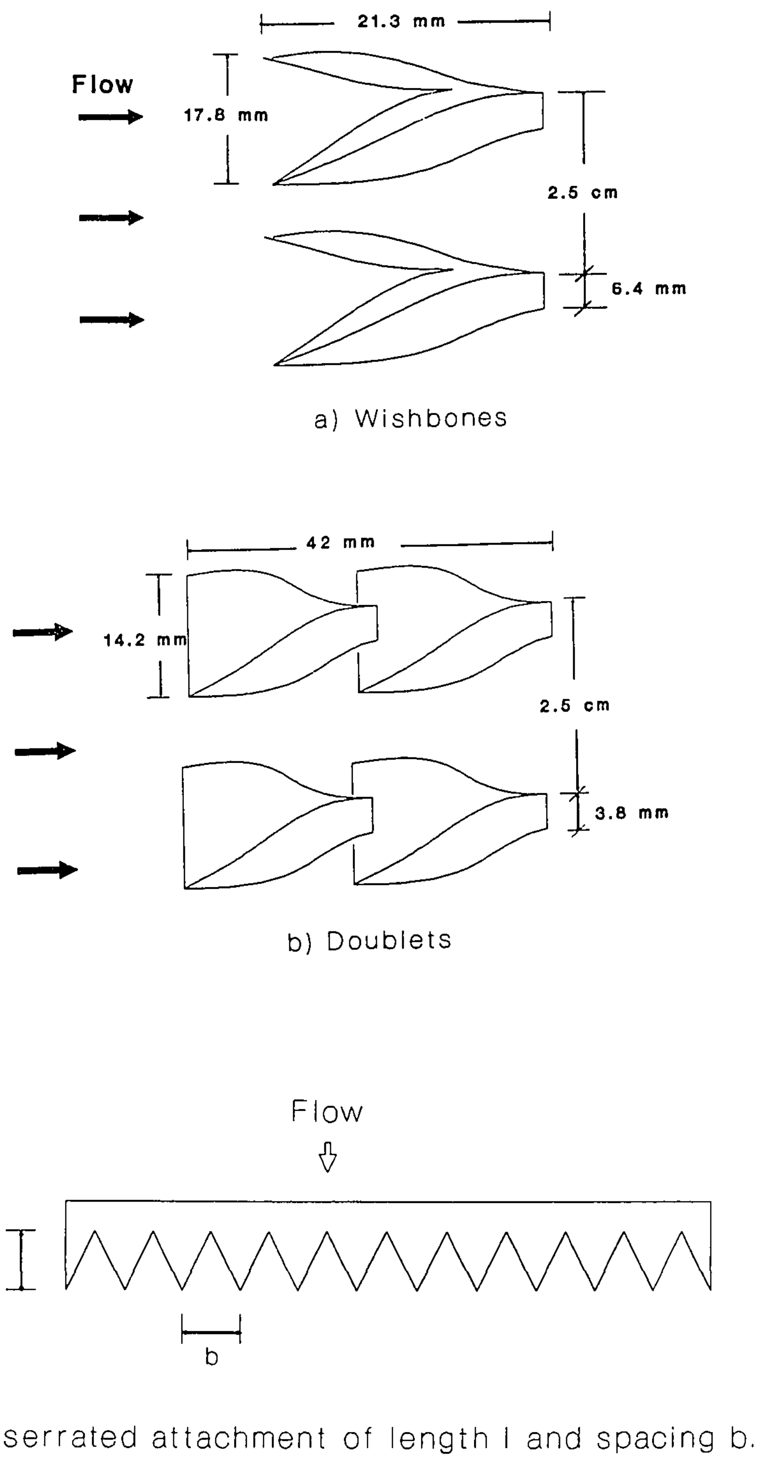

Fig. 2.6 Doublet, wishbone, and serrated (2–D) flow-control devices

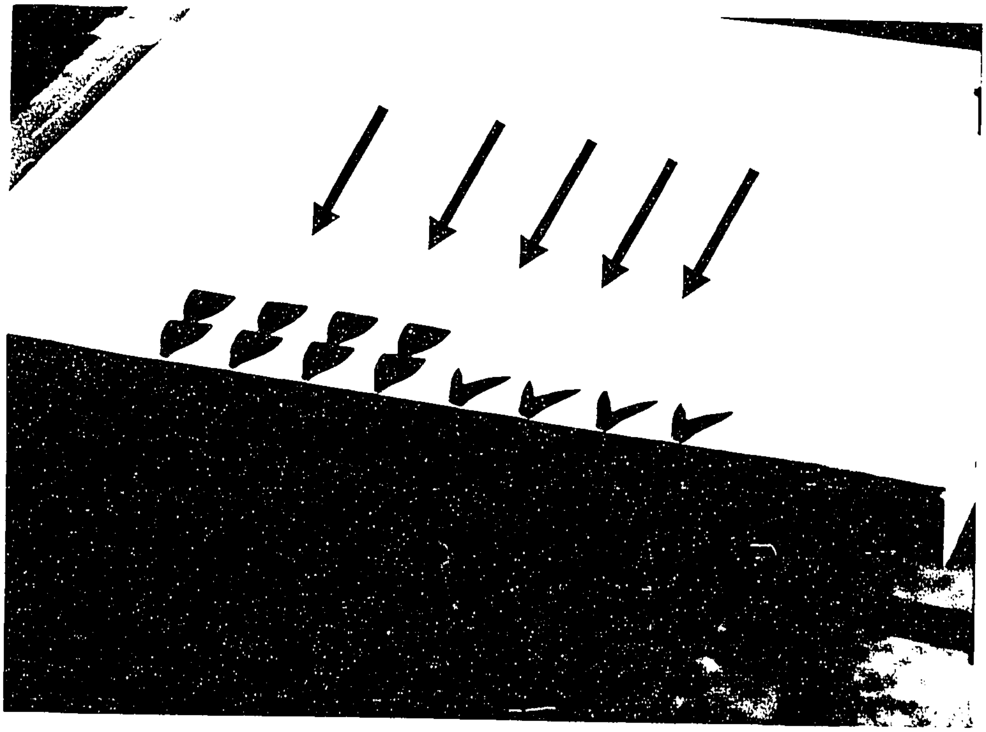

Fig. 2.7 A typical arrangement of wishbone and doublet vortex generators at the model trailing edge.

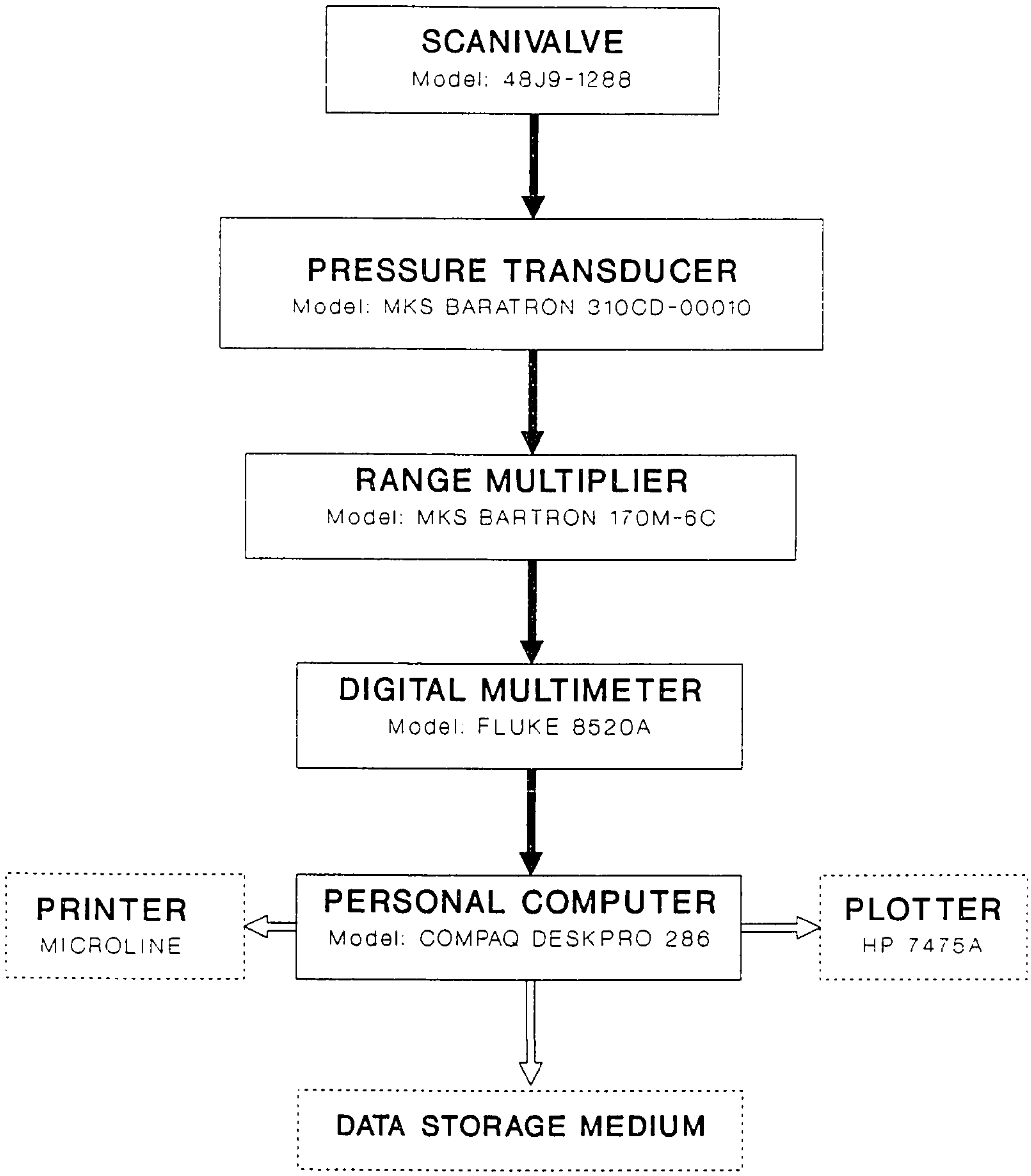

Fig. 2.8 Instrumentation block diagram for pressure measurements

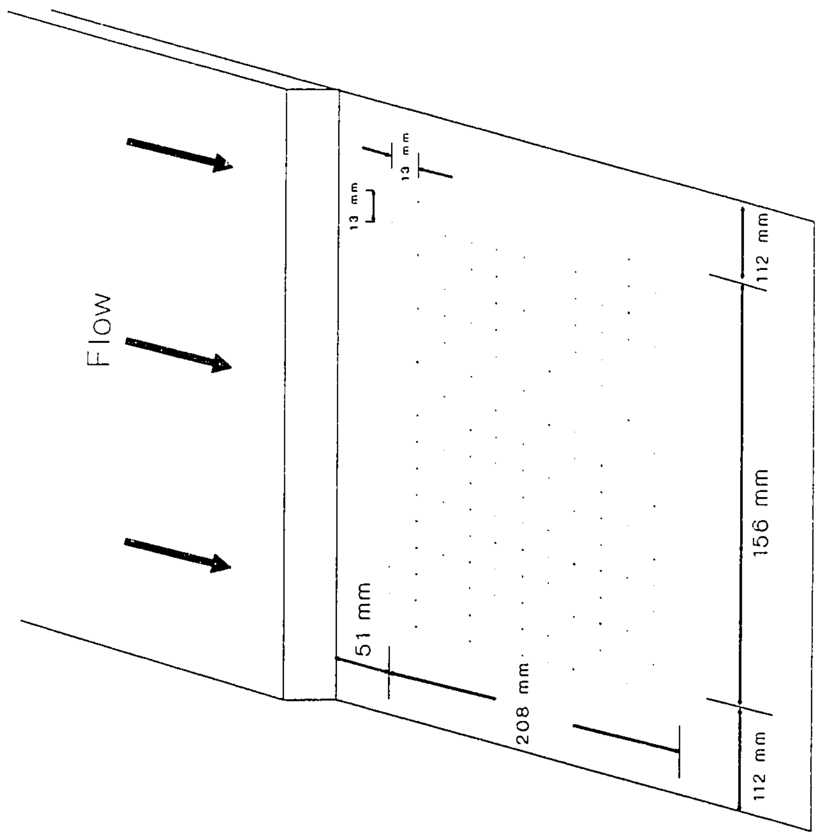

Fig. 2.9 Oil-drop flow visualization grid for the 2–D rearward-facing step

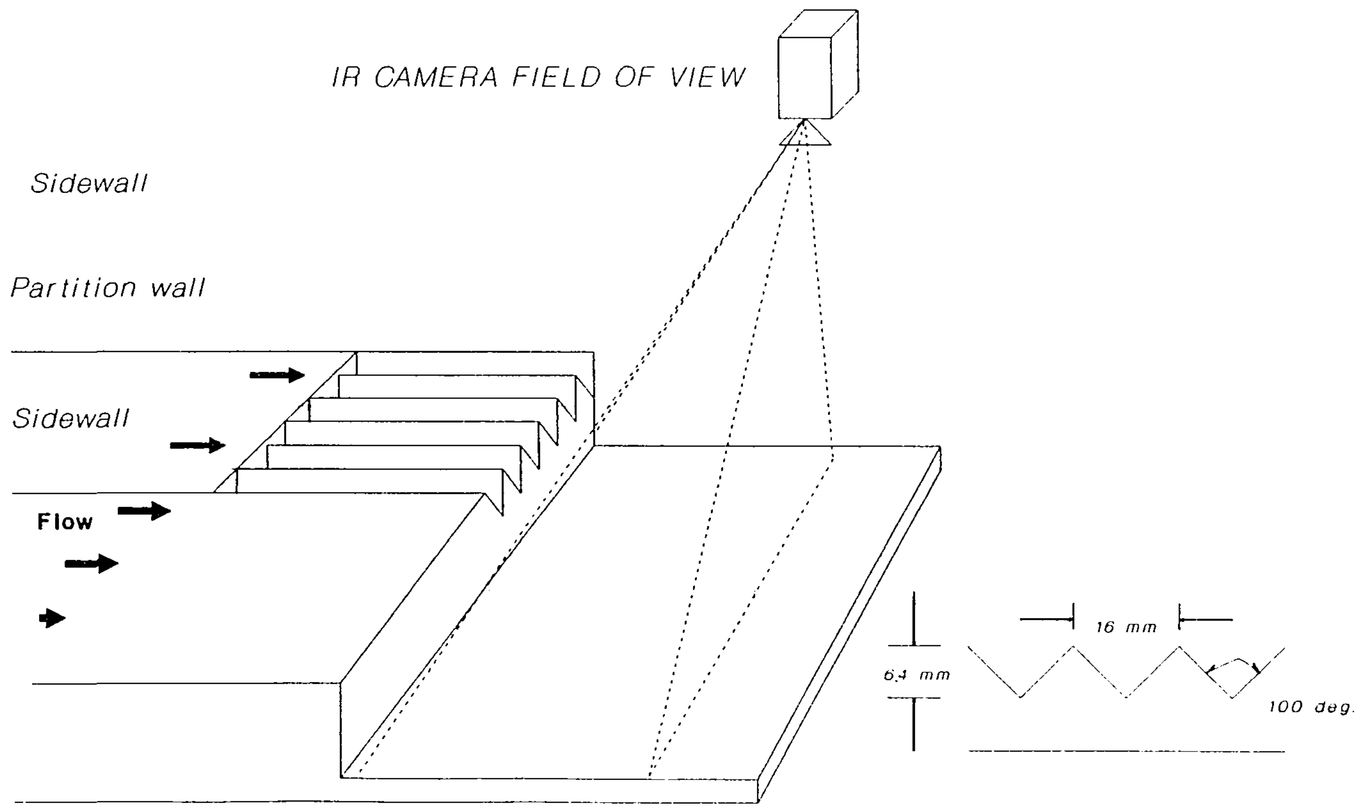

Fig. 2.10 Unswept rearward-facing step model for heat transfer testing

Fig. 2.11 Top view of the 30° swept rearward-facing step model showing pressure tap positions

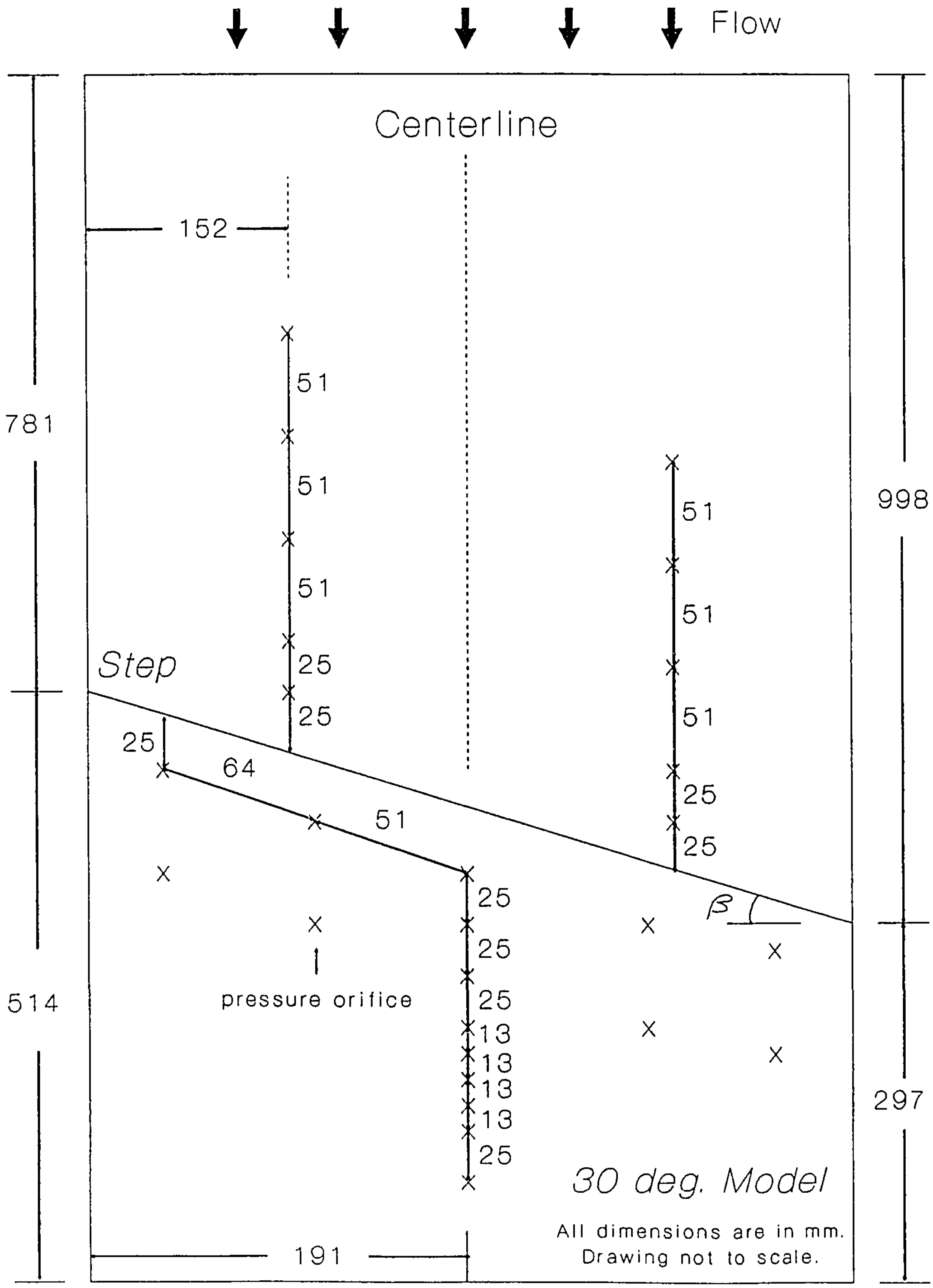

Fig. 2.12 Top view of the 45° swept rearward-facing step model showing pressure tap positions

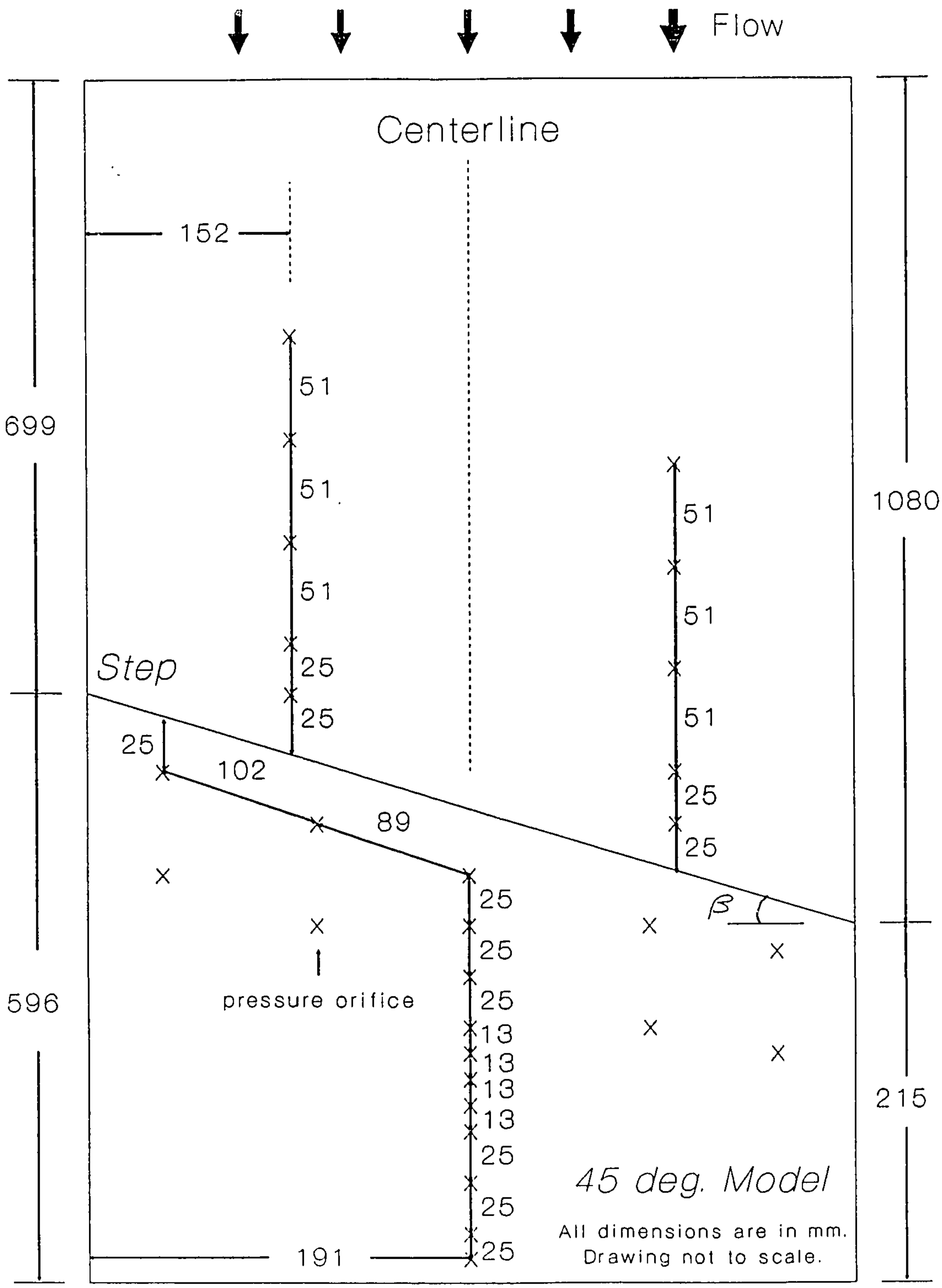

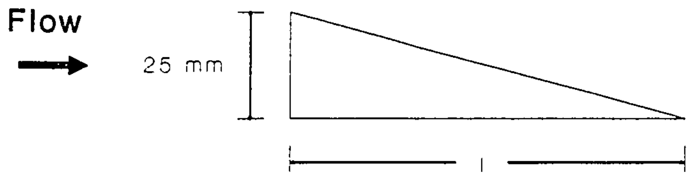

a) a triangular fence of length l.

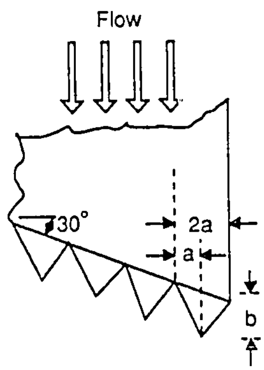

b) Triangular serrations
(a=1.3 cm, b=2.5 cm)

Fig. 2.13 Sketches of fence and serrated attachments for swept rearward-facing step models

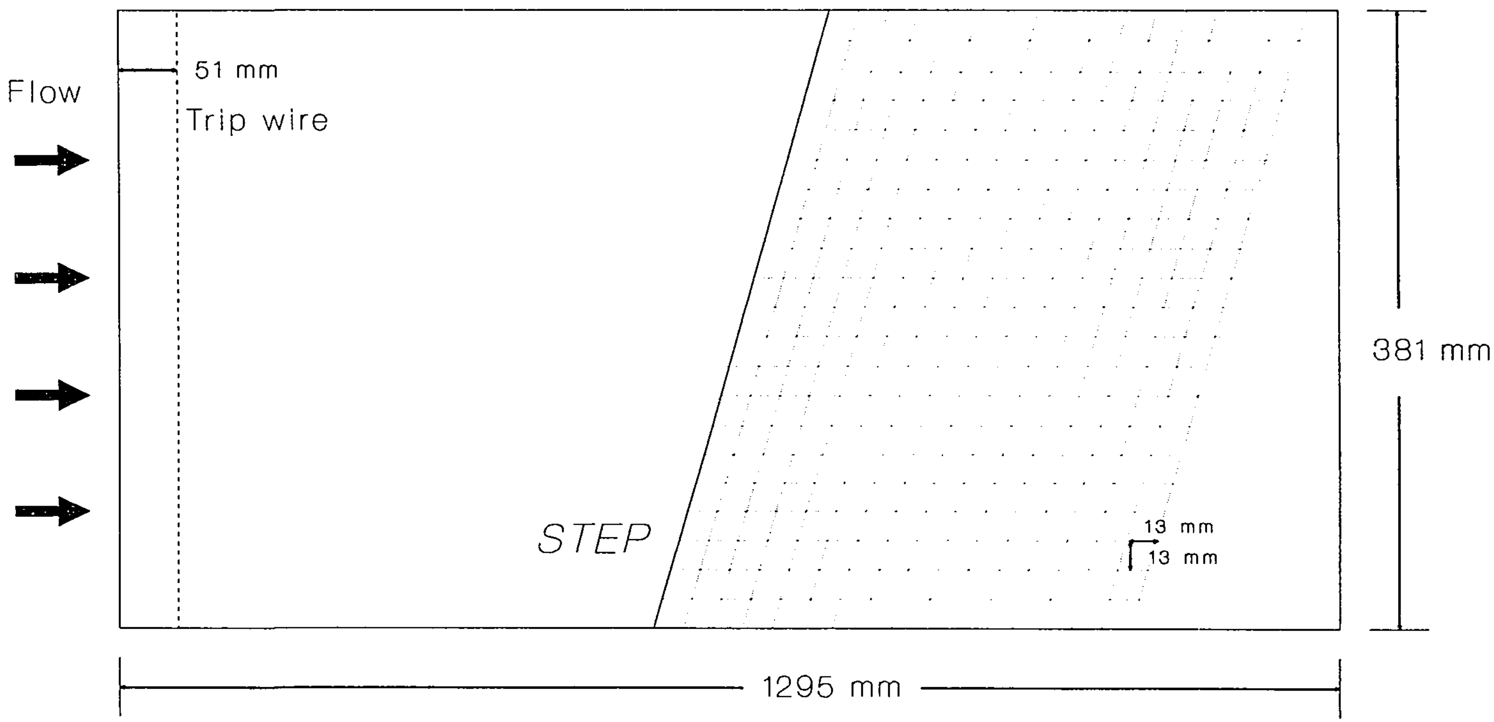

Fig. 2.14 Top view of the swept rearward-facing step showing oil-drop flow visualization grid

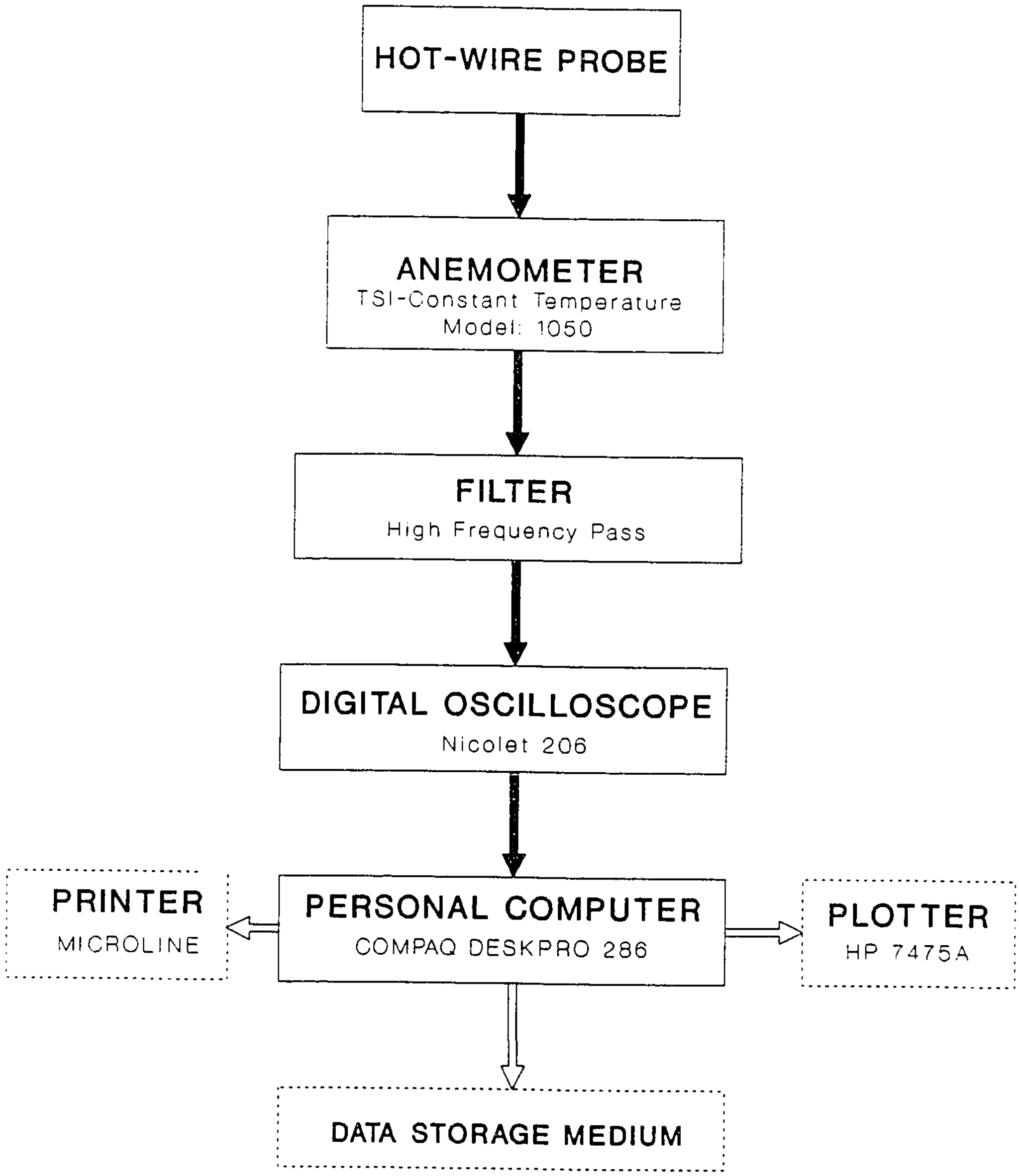

Fig. 2.15 Instrumentation block diagram for vortex-shedding frequency measurements

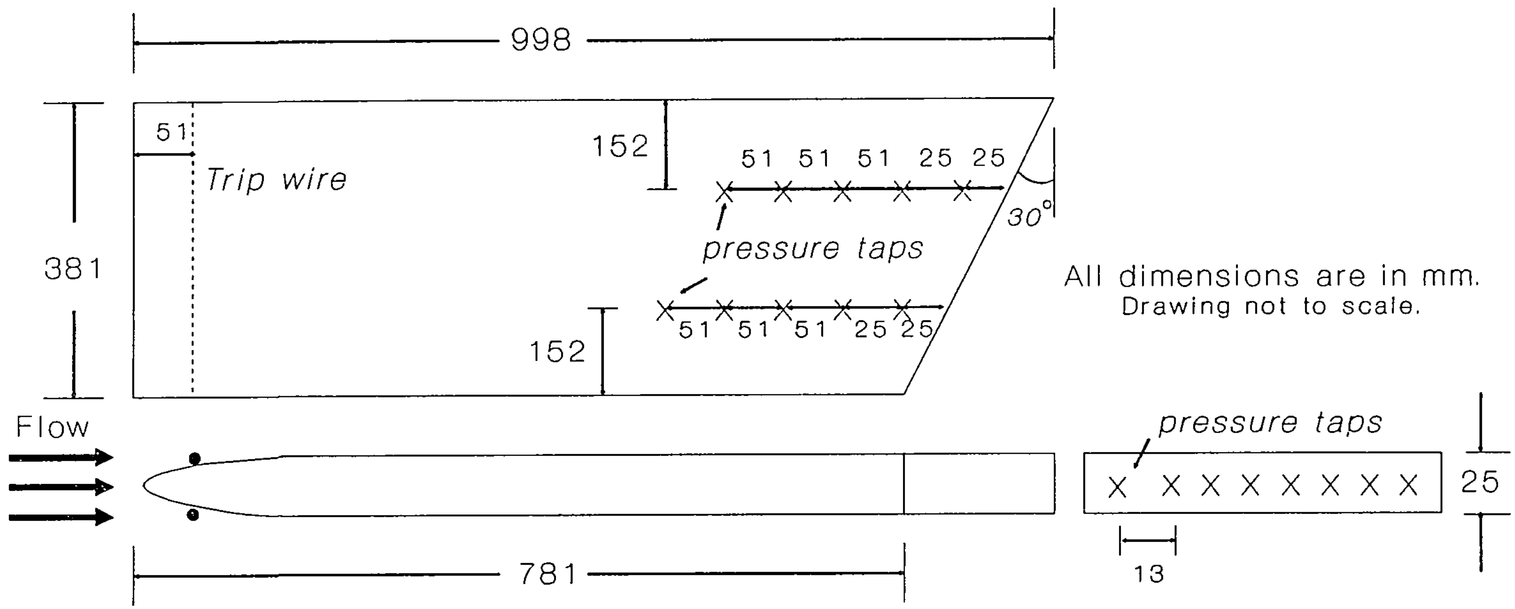

Fig. 2.16 Schematic of the flat-plate airfoil model with 30° swept base

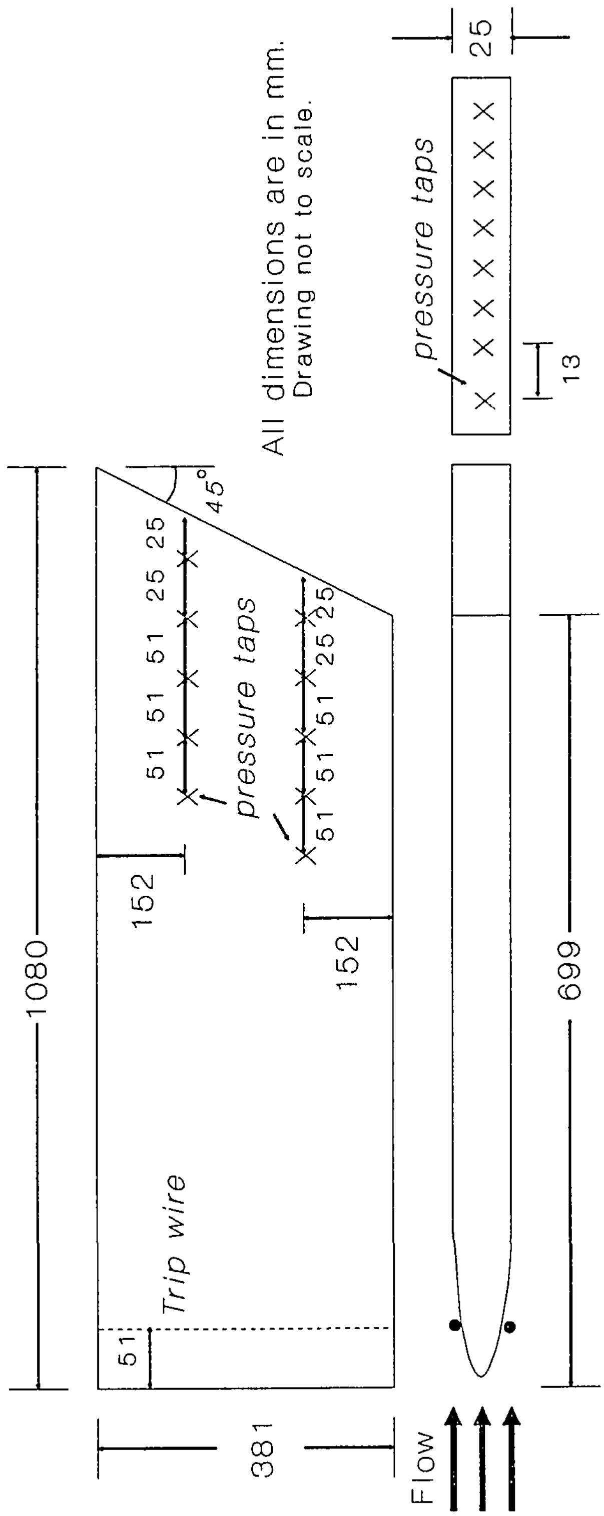

Fig. 2.17 Schematic of the flat-plate airfoil model with 45° swept base

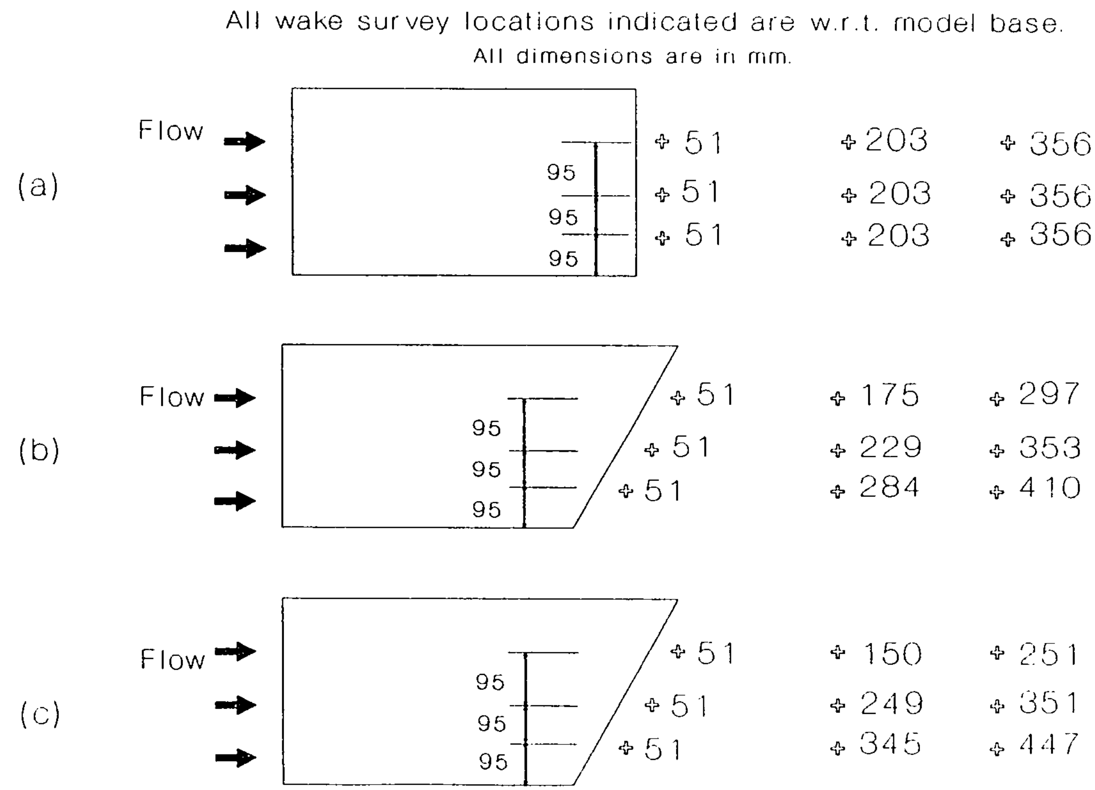

Fig. 2.18 Wake velocity defect survey locations
a) unswept model
b) 30° swept-base model
c) 45° swept-base model

Chapter 3

DISCUSSION OF REARWARD-FACING STEP RESULTS

3.1 2–D Rearward-Facing Step

3.1.1 Base Pressure

Spanwise base pressure variation at two Reynolds numbers (V = 18.5 m/sec and 43.1 m/sec) for flow over a rearward-facing step is plotted in figure 3.1. These data indicate a uniformity of base pressure at both speeds with almost no dependence of the base pressure coefficient, C_{pb}, on the Reynolds number. Noticeable in this figure is the confinement of model sidewall effects on the base pressure to about 10% of the span of the model at either end.

In figures 3.2–3.7, the coefficients of base and surface pressure as a function of spanwise position at several locations downstream of the step are plotted for various modifications (see table 3.1) made to the model. It is evident from figure 3.2, for the unmodified rearward-facing step model, that there is spanwise uniformity for the base as well as surface pressure. Surface pressure reaches a minimum value at about three step heights downstream of the step base. Pressure recovery starts somewhere between three to five step heights downstream of the base and the pressure continues to increase up to ten step heights downstream. A similar behavior is observed for the step model modified with 25.4 cm long deep rectangular grooves, as shown in figure 3.3. In this case, however, the pressure recovery begins upstream of the baseline location — about two to three step heights downstream of the base for this configuration. In addition, the maximum pressure recovery for this configuration is similar to the baseline value. Modification of the baseline models with V-grooves exhibited similar surface pressure variations as the model with deep rectangular grooves, as shown in figures 3.4 and 3.5. In the latter case, the pressure recovery, after five step heights from the base, is not as high as with V-grooves, although the maximum pressure recovery is similar. The rearward-facing step model modified with wishbone and doublet vortex generators showed a significant spanwise variation in the surface pressure within one step height downstream of the base (figures 3.6 and 3.7, respectively). As a result, it is difficult to determine the precise region in which the pressure recovery process starts for these modifications, although two to three step heights appears to be the approximate location. The maximum pressure recovery for the two-dimensional step model with either wishbone or doublet vortex generators is significantly greater than the maximum level for all other configurations.

Base pressure measurements for unswept models involving V-grooves and rectangular grooves are presented in figure 3.8. No significant spanwise variation in the base pressure distribution can be identified that corresponds to the device wavelength. However, it does appear that the small spanwise variations noted may be cyclic at the same wavelength as the device spacing (2.5 cm). Although all three modifications present equal changes in the area from the baseline model, it appears that the shallow rectangular grooves have the effect of increasing the mean step base pressure above the baseline value. The other two modifications have shown no significant effect on the base pressure. Probing of the flow within and downstream of the V-grooves with a hot-wire anemometer indicated that minimally attached flow existed in the grooves, although vortical flow was anticipated. Assuming attached flow in all three groove geometries, longitudinal momentum is added to the separated-flow region in all three cases. With the

V-grooves and the deep rectangular grooves, the momentum addition occurs further away from the dividing streamline and may result in locally segmenting the flow in the base region into alternating areas of attached and separated flow. For these two configurations, changes to the flow physics present for the baseline configuration would be driven more by geometry (determined by groove depth) than in the case with the shallow rectangular grooves. In the latter case, momentum addition occurs nearer the separating streamline and no segmenting of the separated flow likely occurs since only a short span between grooves is at the nominal base thickness. Thus, momentum addition to the higher-speed fluid in the shear layer avoids segmenting the separated flow while providing additional energy to overcome the adverse pressure gradient.

Results of base pressure measurements for the rearward-facing step modified with wishbone and doublet vortex generators are plotted in figure 3.9. Both types of modifications decrease the base pressure, with the change being significant in the case of the wishbone vortex vortex generators. The apparent non-uniformity in the base pressure foir $z/s > 0.70$ is attributed to the interference caused by the presence of the test-section traverse mechanism strut. A similar plot for base cavity and triangular serration modifications is presented in figure 3.10. Both modifications have decreased the base pressure significantly when compared to the baseline basic model. These last four modifications apparently increase the circulation in the base region with an accompanying decrease in the base pressure. The asymmetric end effects shown in figure 3.10 for the wishbone and doublet modifications are unexpected.

3.1.2 Surface Pressure

Streamwise surface pressure variation at midspan for the 2–D rearward-facing step model with various modifications are presented in figures 3.11 to 3.18.

Surface pressure for the baseline rearward-facing step reaches its minimum and maximum at three and seven step heights downstream of the base, respectively (figure 3.11). This pattern of variation appears to be independent of the Reynolds number in the range examined.

Streamwise surface pressure profiles for the unswept step model with deep (7.7m×6.4m) and shallow (15.3m×3.2mm) rectangular grooves are presented in figure 3.12. The maximum level of pressure recovery for the rectangular-groove modifications is similar to the level attained with the baseline model; however, the rate of recovery is higher, upstream of the location of the maximum level achieved, for the models with grooves.

Streamwise surface pressure variation as a function of V-groove angle is presented in figures 3.13 and 3.14 for V-grooves with a depth of 6.4 mm. Similar trends were observed for the V-groove and rectangular-groove modifications, as compared to the baseline data. One exception is that pressure recovery began closest to the step for rectangular grooves, as compared to the V-groove and baseline configurations. In addition, the rate of pressure recovery immediately downstream of the step appears to increase with increasing groove angle. As groove angle increases at constant groove depth, the rate of flow of high momentum fluid into the base region increases, resulting in the variations observed. Variations in streamwise surface pressure profiles with groove depth (α = 30°) are depicted in figure 3.15. Again, the maximum pressure recovery achieved is comparable to the baseline data, while the rate of pressure recovery downstream of the step increases with increasing groove depth for the reason indicated previously. In figure 3.16, the streamwise pressure distribution for V-grooves (α = 50°, d = 6.4 mm) is shown to be somewhat dependent on free-stream speed. The level of pressure recovery achieved at U_∞ = 43 m/s is higher than the level achieved at U_∞ = 19 m/s, although the level upstream of the step and immediately downstream of the step is identical for these two cases.

Surface pressure measurements for modifications involving wishbone and doublet vortex generators are presented in figure 3.17. In both cases, the maximum level of pressure recovery achieved was higher than the baseline level. The exact location of the maximum pressure is not determinable from the streamwise pressure distributions because of the inadequate number of pressure orifices in that region. The streamline surface pressure for the vortex generator configurations has almost relaxed back to the baseline level at 10 step heights downstream of the step. This is an indication that the streamwise momentum enhancement to the shear-layer flow has greatly dissipated by the time this location was reached. In addition, pressure recovery for the wishbone and doublet configurations is initiated nearer the step, compared to the baseline configuration.

Finally, surface pressure profiles for tests performed with the 2.5 cm long triangular serrations and 2.5 cm deep base cavity are presented in figure 3.18. A sharp pressure rise in the immediate vicinity of the base characterizes the flow associated with these two modifications. This pressure increase is consistent with the discussions of Section 1.1.1. Higher levels of pressure recovery were achieved with the serration and cavity modifications, compared to the baseline configuration, and the location of the pressure maximum was translated in the downstream direction in the cavity configuration. This latter result was due partially to delayed separation caused by the 2.5 cm long horizontal extension to the surface upstream of the step in order to form the base cavity.

3.1.3 Reattachment Distance

Results of oil-drop flow-visualization tests to determine flow reattachment distance are tabulated in table 3.8. Some of the tests were repeated to increase the certainty with which the reattachment region was determined. A reattachment region was identified as compared to a reattachment line, because the location of the reattachment line is time-dependent for a 2–D rearward-facing step flow. The stationary oil drops, indicative of a stagnation region, were used to identify the reattachment region in the present tests. It appears from these tests that the 2–D rearward-facing step modified with V-grooves (α = 50°, d = 6.4 mm) had the shortest reattachment length. Modifications with triangular serrations and a base cavity had the effect of increasing the reattachment distance, due to separation delay. In general, modifying the step with vortex generating devices (i.e., wishbones and doublets) and grooves resulted in shorter flow reattachment distance. However, it should be noted that grooves appear to be more effective than the vortex generating devices.

A review of the data of table 3.8 and figure 3.8 to 3.10 indicates that a reduction in reattachment length is generally accompanied by a decrease in base pressure (increase in circulation in the base region). It was reasoned that an increase in circulation would result in an increase in the convective heat transfer rate from the model surface in the separation region. This motivation resulted in the design of the heat-transfer tests to examine the effect of V-grooves on the convective heat-transfer rate downstream of the 2–D rearward-facing step.

3.1.4 Convective Heat-Transfer Rate

The color-coded temperature images of the model test surface provided by the IR imaging system were decoded to get the temperature maps shown in figures 3.19 and 3.20. With respect to the model surface, the infrared imaging camera was positioned so that its field-of-view extended from the step base to about 20 cm downstream, thus covering the separation-flow region of the model. Inspection of the initial temperature maps of the model surfaces prior to the start of the test indicated a uniformity of surface temperatures. Temperature maps of the model test surfaces 90 seconds after the start of the tests are presented in figures 3.19 and 3.20 for steps heights of 1.0 cm and 2.5 cm, respectively. Comparison of the temperatures of the model test surfaces, with grooved and non-grooved surfaces upstream of the step, indicate higher surface temperatures for the grooved-step case. This finding, which is consistent for both step heights tested, implies an increase in the convective heat-transfer rate in the separated-flow region of a rearward-facing step with grooved upstream surface. The increase in the convective heat-transfer rate observed in the separated-flow region could be caused by the introduction of fluid of higher momentum into this region by the action of the attached flow in the grooves.

3.2 Swept Rearward-Facing Step

3.2.1 Base Pressure

In figures 3.21–3.35, results of base pressure measurements for swept (β = 30° and β = 45°) rearward-facing steps with various modifications are presented. In each figure the base pressure coefficient as a function of the non-dimensional distance along the baseline of the step is presented. In addition, the surface pressure coefficient at one and three step heights downstream of the step is plotted to examine its variation in the direction parallel to the step baseline. Variation in the pressure coefficient along the baseline of the step is one indication of the presence of three-dimensional flow in this region.

Baseline base pressure distribution is presented in figure 3.21 for the 30° swept rearward-facing step. The spanwise surface pressure distribution at two positions downstream of the step is also presented. The adverse pressure gradient in the base region is predictable since the cross-sectional area of the test section increases in the downstream direction due to the presence of the swept step. The favorable pressure gradient at x/h = 3 over the upstream 50% of the span is due to the flow relaxing as it proceeds downstream from the geometry-driven adverse pressure-gradient region.

The pressure distribution in the base region for the 30° swept rearward-facing step with shallow (15 mm by 3 mm depth) rectangular grooves is presented in figure 3.22. The most noticeable difference between the present and baseline configurations is the higher favorable pressure gradient at x/h = 3 over the upstream 50% of the span for the rectangular groove configuration. Base and surface pressure distributions are in figure 3.23 for the V-groove modification (α = 50° and d = 6.4 mm). Although the base pressure distribution is similar to baseline for this configuration, the surface pressure distribution downstream of the base is not. While the surface pressure distributions at x/h = 1 and 3 for the baseline configuration are coincident with the base pressure distribution. The pressure distribution at x/h = 1 for the 30° swept step with V-grooves has a significantly lower adverse pressure gradient than the base. In addition, the pressure gradient at x/h = 3 is favorable over the entire span. The attached flow in the V-grooves energizes the low-momentum flow in the base region and impedes the spanwise flow. The lower pressure levels at x/h = 1 and 3 suggest increased circulation in the base region due to a smaller separated-flow region. Apparently, the introduction of periodic three-dimensional flow structures (via surface grooves) into a highly three-dimensional separated flow has weakened the three-dimensionality of the flow downstream of the base.

The spanwise pressure variation in the base region for the 30° swept step with normal and reversed (apex facing upstream) wishbone vortex generators is displayed in figures 3.24 and 3.25, respectively. The adverse pressure gradient at the base for the two wishbone configurations is higher along the upstream half of the span than along the downstream half, and the pressure level is lower, partially due to a blockage effect caused by the physical presence of the wishbone devices. The vortices generated by the wishbone vortex generators are apparently stronger when the devices are placed in the reversed orientation, since these devices cause larger deviations from the baseline results in the latter case. At x/h = 3 with the wishbone in the reversed orientation (figure 3.25), the surface pressures are much higher than the baseline case and the pressure gradient has been reduced to zero at that location. The results with reversed wishbones are similar qualitatively (but not quantitatively) with the results obtained with the V-groove modification examined previously. The results with doublet vortex generators (figure 3.26) are similar to those with the wishbone vortex generators in their normal orientation (figure 3.24). The pressure distributions (figure 3.27) with triangular serrations (also expected to produce streamwise vortices) are very close to the baseline results.

Base-pressure distributions for the 30° swept rearward-facing step are compared in figure 3.28 for V-groove and rectangular-groove modifications; in figure 3.29 for vortex-generator modifications; and in figure 3.30 for serration and fence modifications. The groove modifications caused higher base pressures (figure 3.28) due to the larger cross-sectional flow area resulting from groove geometry. However, the base pressure gradient is similar to the baseline levels for these two modifications. The base pressure distributions associated with the wishbone and doublet vortex generators (figure 3.29) are generally lower than or equal to the baseline distribution. These differences were due partially to blockage effects from these solid devices, as well as effects from the longitudinal vortical structures introduced into the separated-flow region. Triangular serrations (figure 3.30) caused lower pressure levels, possibly due to increased base circulation. The fence configurations (figure 3.30) resulted in significant variations to the spanwise pressure distribution caused by the turning of the spanwise vortical flow in the separation region into the streamwise direction by each fence. At the same time, each fence served as the origin of a region of spanwise vortical flow, as determined from oil-drop flow visualizations.

The baseline base pressure distribution is presented in figure 3.31 for the 45° swept rearward-facing step. The spanwise surface pressure distribution in the vicinity of the base is also presented. The adverse pressure gradient in the base region for this sweep angle is highly variable over the span of the model. The high initial adverse pressure gradient over the initial 30% of the span is probably due to end effects, including the effect of the wall on the developing spanwise separated vortical flow. Away from the wall at the upstream end of the base, the pressure gradient approaches an asymptotic value. As expected from consideration of the rate of flow cross-sectional area change as a function of the longitudinal coordinate, the level of the pressure gradient in the base region for the 45° swept step is lower than the value for the 30° swept step.

The spanwise pressure variation in the base region for the 45° swept step with V-grooves ($\alpha = 50°$, d = 6.4 mm) and for the reversed wishbone vortex generators are presented in figures 3.32 and 3.33, respectively. These two modifications resulted in the most significant changes to the baseline pressure distribution for the 30° swept step. However, as shown in figures 3.31 to 3.33, the changes are not as significant for these modifications when applied to the 45° swept step. The spanwise flow in the separation region becomes more significant as the step sweep angle is increased. Flow control of this highly three-dimensional separated flow is more difficult to accomplish at the higher sweep angle of 45°. This is evident from figures 3.32 and 3.33, when compared to the baseline data of figure 3.31.

The spanwise base pressure variation for the 45° swept rearward-facing step with wishbone vortex generators is compared to the baseline distribution in figure 3.34. The more pronounced departure from the baseline configuration is attained with the reversed wishbones. The lower pressure level with the reversed wishbones, compared to the normal wishbone and baseline configurations, is indicative of higher circulation in the base region for the reversed wishbone vortex generators. The base pressure distribution with the reversed wishbones also reaches the asymptotic pressure gradient level nearer the upstream end of the base, compared to normal wishbone and baseline distributions.

Figure 3.35 depicts the effect of V-groove and fence modifications on the base pressure distribution. Base pressure with V-grooves are generally higher than the baseline values, due to the cross-sectional flow area consideration. Similar to the case with reversed wishbone vortex generators, the spanwise pressure gradient for the V-groove modification reaches its asymptotic value nearer the upstream end of the base, compared to the baseline case. The fences create a pressure distribution characteristic of a separated flow divided into several smaller separated regions. However, fences result in a significant reduction to the pressure coefficient. Such a reduction is normally undesirable, unless it occurs on the suction surface of an airfoil, or in some similar application. Usually, increased negative surface pressures in a region of separated flow translate into a higher drag coefficient for the body on which it occurs.

3.2.2 Surface Pressure

Longitudinal surface pressure distributions were obtained for the 30° and 45° swept rearward-facing step models and are presented in figures 3.36 to 3.46. These surface pressure data were collected from two rows of pressure taps upstream of the step (at z/s = 0.4 and 0.6) and from a single row of pressure taps downstream of the step (at z/s = 0.5). Pressure recovery for the 30° swept step with rectangular grooves is similar to the baseline level (figure 3.36). For the wishbone modification, the pressure recovery is slightly less than baseline (figure 3.37). The pressure recovery with reversed wishbone vortex generators is significantly less than baseline (figure 3.38); however, the rate of pressure recovery near the base is much higher. The level of pressure recovery with doublet vortex generators (figure 3.39), triangular serrations (3.40), and streamwise fences (3.41) is similar to the baseline level, with similar recovery rates.

In addition, pressure recovery levels and rates for the 45° swept-step model with V-groove (figure 3.42), wishbone (figure 3.43), and reversed wishbone (figure 3.44) modifications are similar to baseline values. In comparison, the pressure recovery rates are higher than baseline values for the 45° swept step with four 5 cm or 15 cm long flow fences (figures 3.45 and 3.46). These fences are equally spaced (at z/s = 20%, 40%, 60%, and 80%) spanwise along the base of the model and inhibit the spanwise flow, with the longer fences being more effective in this respect. The longer fences also result in a higher level of pressure recovery compared to baseline and lower pressures in the base region of the step.

3.2.3 Reattachment Distance

Photographs of the flow pattern left on the downstream section of the rearward-facing step were used to determine the flow reattachment line for selected modifications. Sample oil-drop flow-visualization photographs are presented in figures

3.47 and 3.48. In figures 3.49–3.53, the reattachment line for each model tested is plotted as the nondimensional (w.r.t. step height) distance normal to the step as a function of distance along the step baseline.

The reattachment line associated with flow over the 30° swept rearward-facing step with V-grooves (α = 50°, d = 6.4 mm) is compared with the baseline reattachment line in figure 3.49. A maximum reduction in the baseline reattachment line of approximately 15% was obtained with V-grooves; however, the serrated attachment (figure 3.50) is an example of a modification that did not significantly affect the reattachment line.

The reattachment line for the 45° swept-step model with V-grooves and vortex generators (wishbones and doublets) is shown in figures 3.51 and 3.52, respectively. Consistent with the results pertaining to the streamwise pressure distributions, the devices that were effective with the 30° swept-step model are not effective with the 45° swept-step model. The wishbone and doublet vortex generators have no significant effect on the baseline reattachment line with β = 45°. The spanwise flow in the separated region contains more momentum at β = 45° than at β = 30° and is therefore more difficult to control. The installation of fences at the base of the 45° swept-step model resulted in a significant reduction in the reattachment distance as a function of spanwise position. As shown in figure 3.53, the single separation region was divided by the fences into several smaller regions of separated flow, with the significant overall effect depicted.

Table 3.1 Reattachment distances for the 2–D rearward-facing step model with various modifications

Modification	Reattachment Distance, R/h
Baseline	5.4-5.9
Rectangular grooves	
Deep (7.7 mm×6.4 mm deep)	4.6-5.4
V-grooves (d = 6.4 mm):	
$\alpha = 30°$	5.4-5.7
$\alpha = 40°$	5.0-5.2
$\alpha = 50°$	4.5-4.9
Vortex generators (2.5 cm spacing)	
Wishbone ($h_w = 6.4$ mm)	5.0-5.4
Doublet ($h_w = 3.8$ mm)	4.8-5.2
Triangular serrations:	
1.3 cm long (1.3 cm spacing)	6.4-6.6
2.5 cm long (2.5 cm spacing)	6.2-6.4
Base cavity:	
1.3 cm deep	6.4-6.8
2.5 cm deep	7.0-7.2

Fig. 3.1 Spanwise base pressure variation for the unswept rearward-facing step model ($\beta = 0°$)

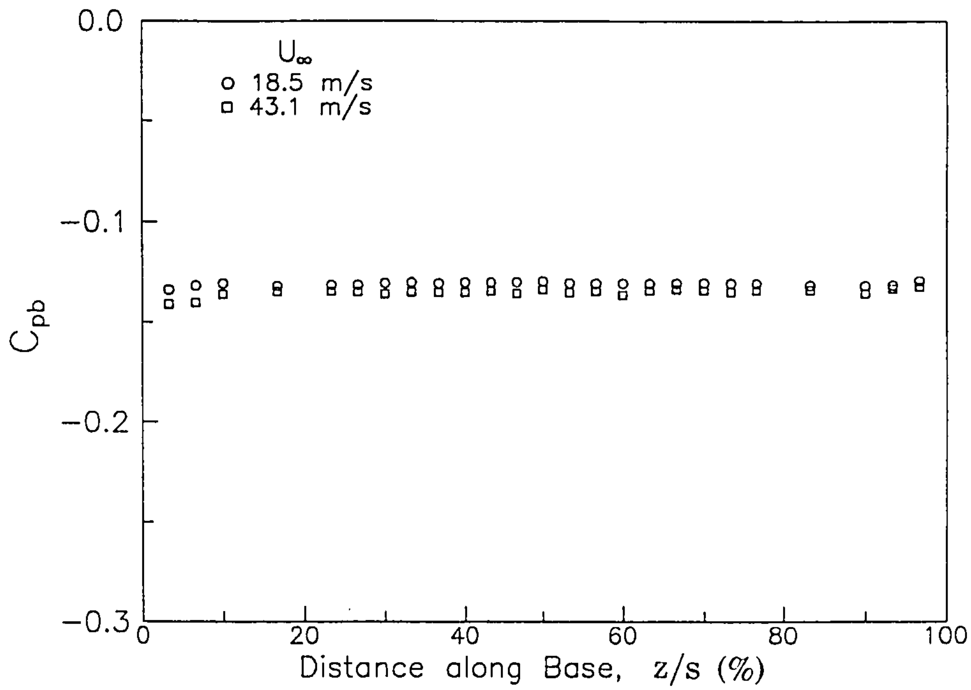

Fig. 3.2 Spanwise base and surface pressure variation at varying streamwise positions downstream of the baseline unswept rearward-facing step model

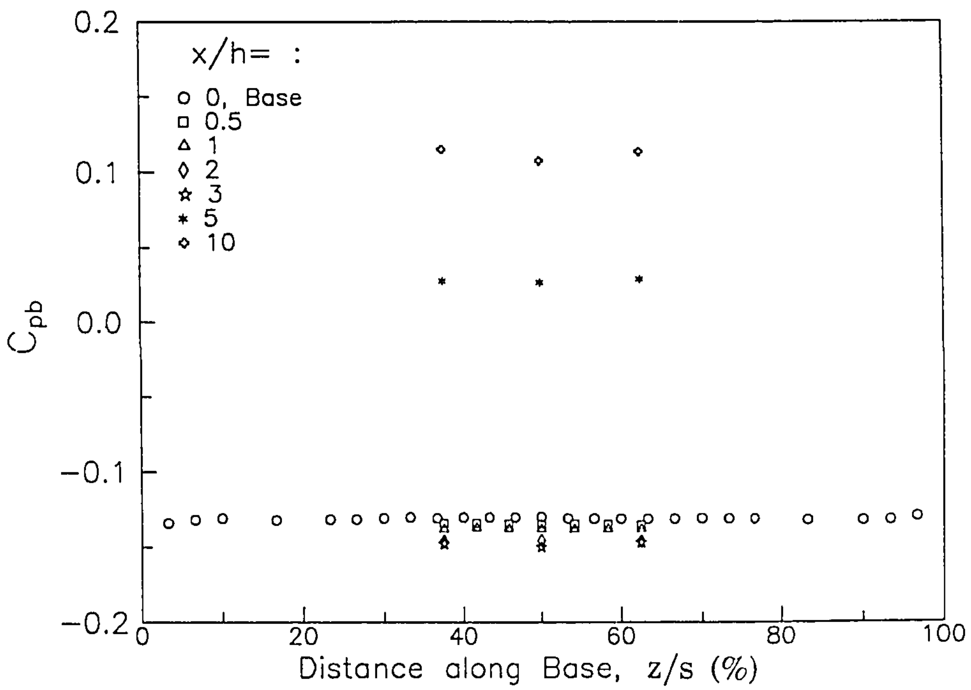

Fig. 3.3 Spanwise base and surface pressure variation at varying streamwise positions downstream of the unswept rearward-facing step with rectangular grooves (w_r = 7.7 mm, d = 6.4 mm)

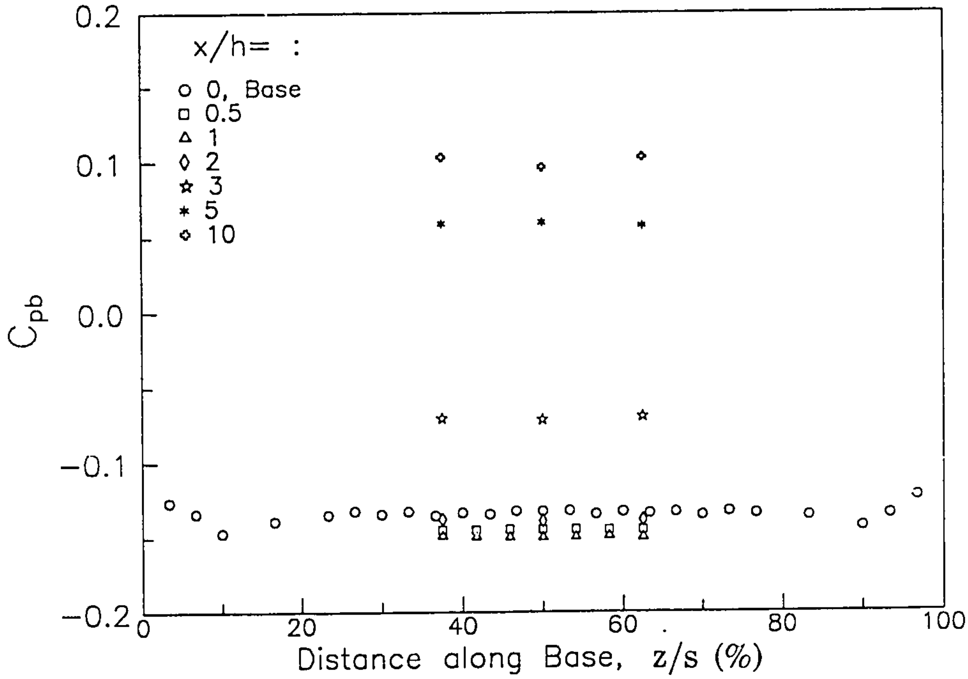

Fig. 3.4 Spanwise base and surface pressure variation at varying streamwise positions downstream of the unswept rearward-facing step with V-grooves (α = 30°, d = 9.5 mm)

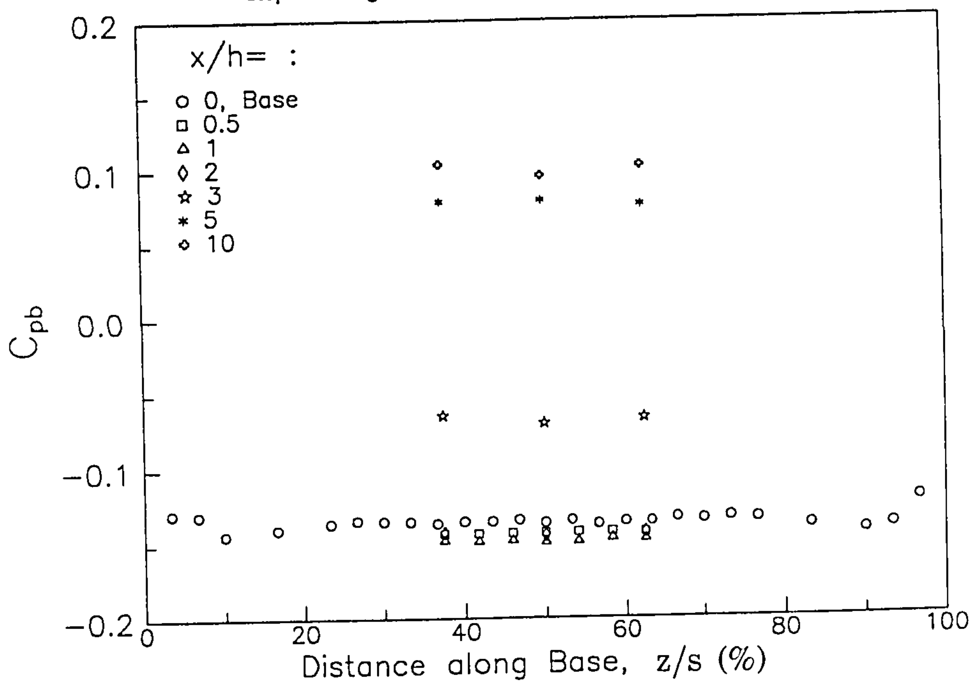

Fig. 3.5 Spanwise base and surface pressure variation at varying streamwise positions downstream of the unswept rearward-facing step with V-grooves (α = 50°, d = 6.4 mm)

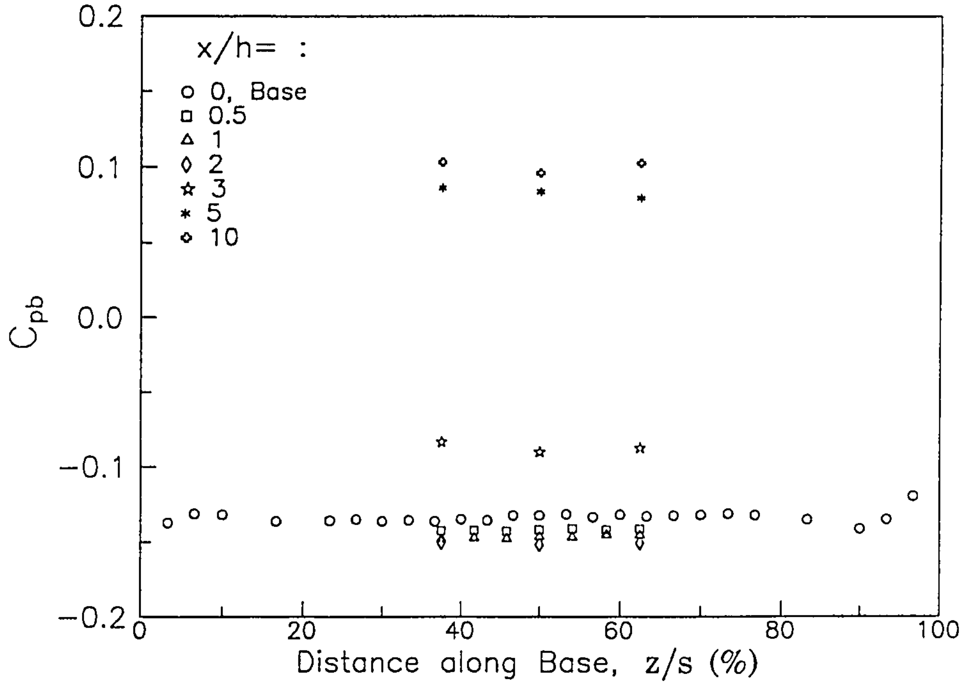

Fig. 3.6 Spanwise base and surface pressure variation at varying streamwise positions downstream of the unswept rearward-facing step with wishbone vortex generators (h_w = 6.4 mm)

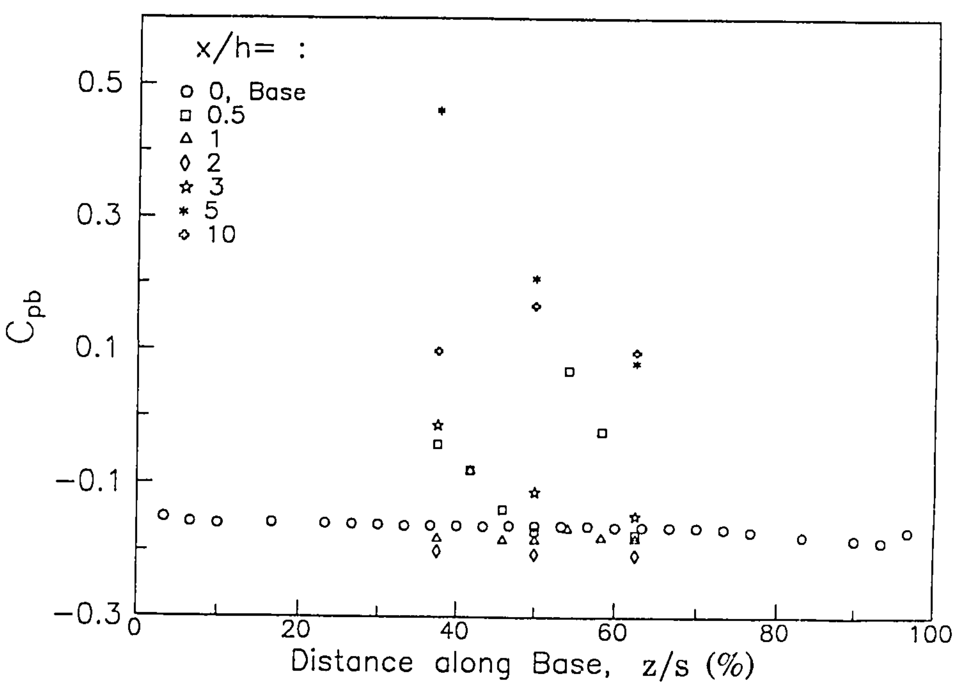

Fig. 3.7 Spanwise base and surface pressure variation at varying streamwise positions downstream of the unswept rearward-facing step with doublet vortex generators (h_w = 3.8 mm)

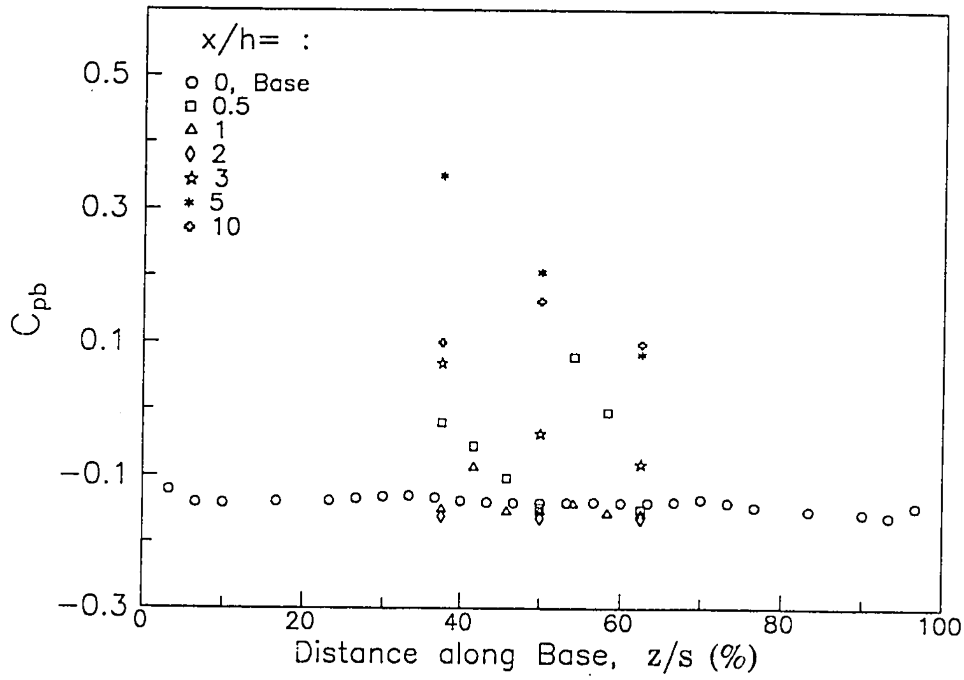

Fig. 3.8 Base pressure variation for the unswept rearward-facing step with V-groove and rectangular groove modifications

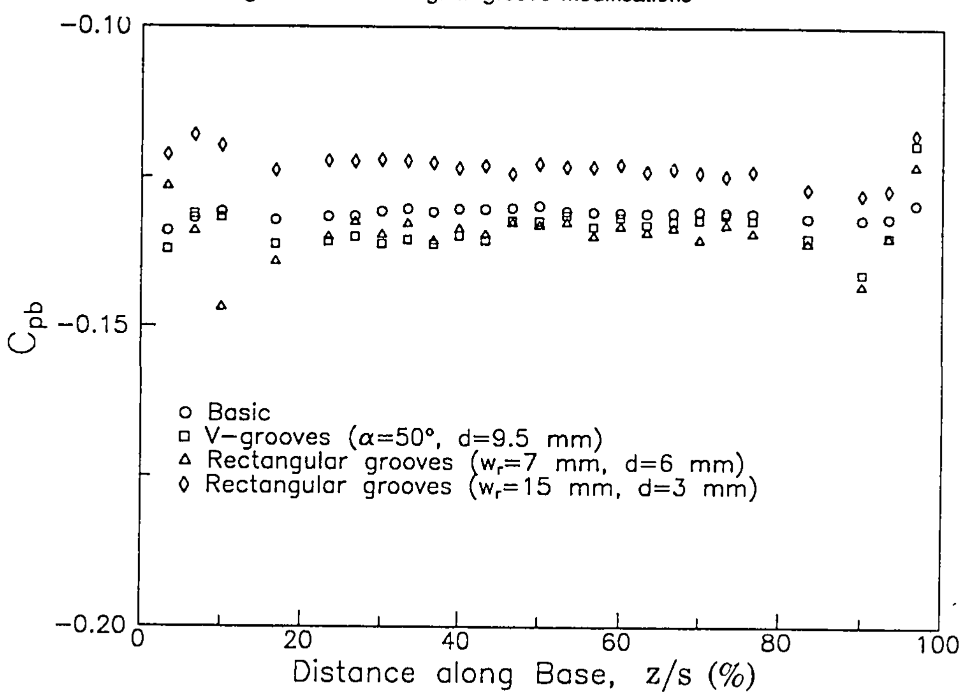

Fig. 3.9 Base pressure variation for the unswept rearward-facing step modified with wishbone and doublet vortex generators

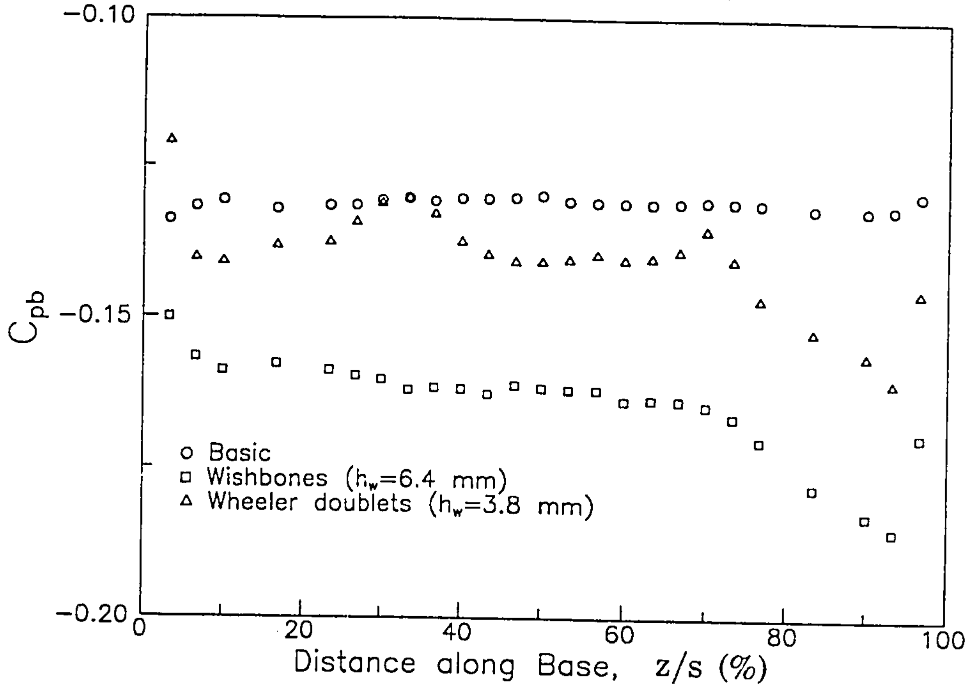

Fig. 3.10 Base pressure variation for the unswept rearward-facing step with base cavity and triangular serration modifications

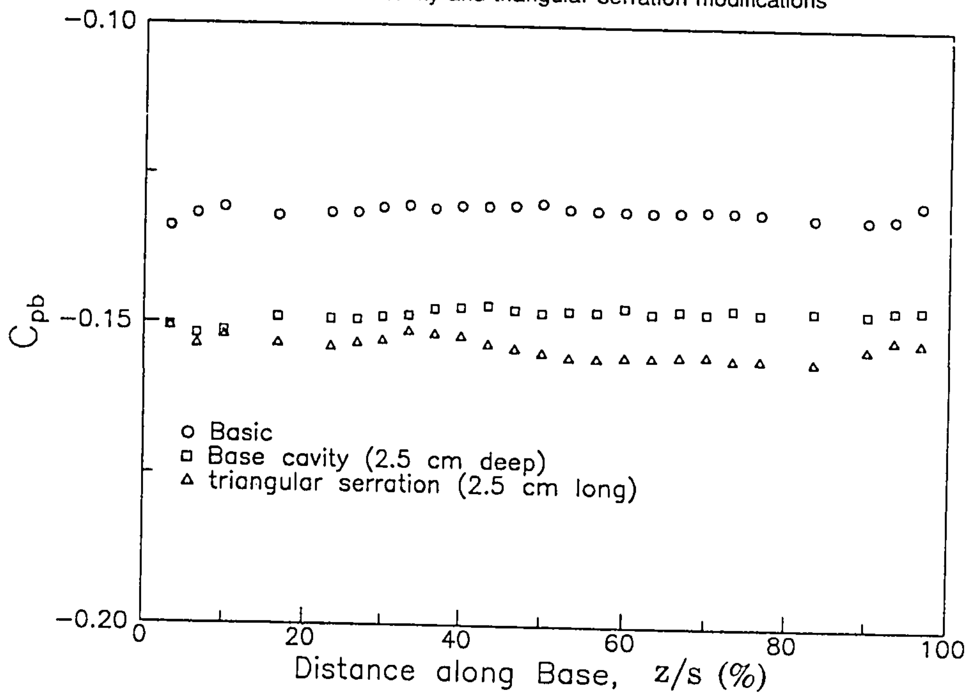

Fig. 3.11 Streamwise surface pressure variation for the unswept baseline rearward-facing step model

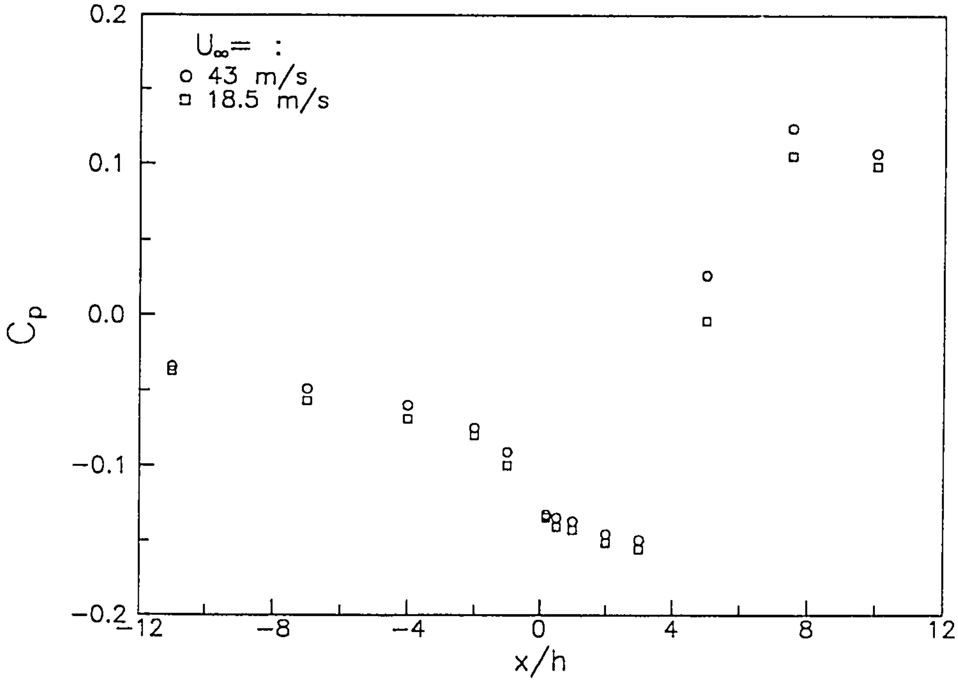

Fig. 3.12 Streamwise surface pressure variation for the unswept rearward-facing step with rectangular grooves

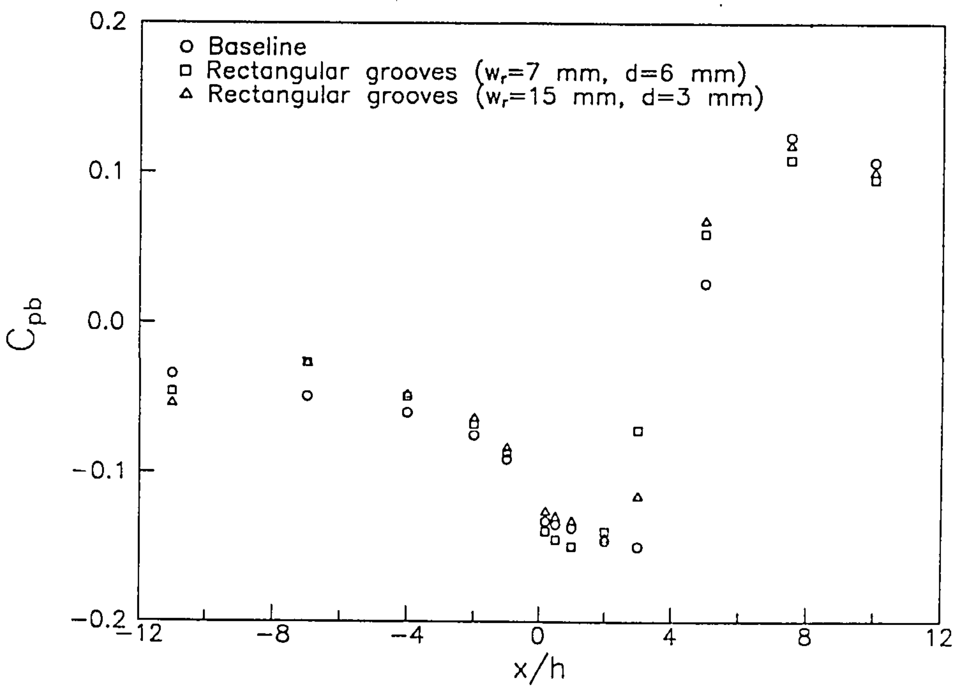

Fig. 3.13 Streamwise surface pressure variation for the unswept rearward-facing step with V-grooves (α = 10°, 20°, and 30°; d = 6.4 mm)

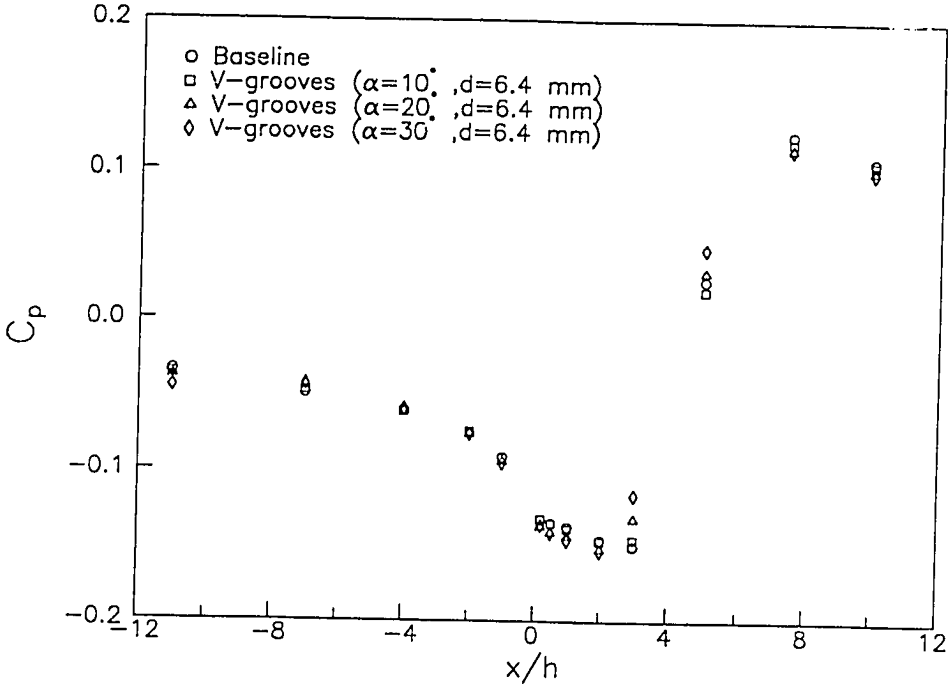

Fig. 3.14 Streamwise surface pressure variation for the unswept rearward-facing step with V-grooves (α = 30°, 40°, and 50°; d = 6.4 mm)

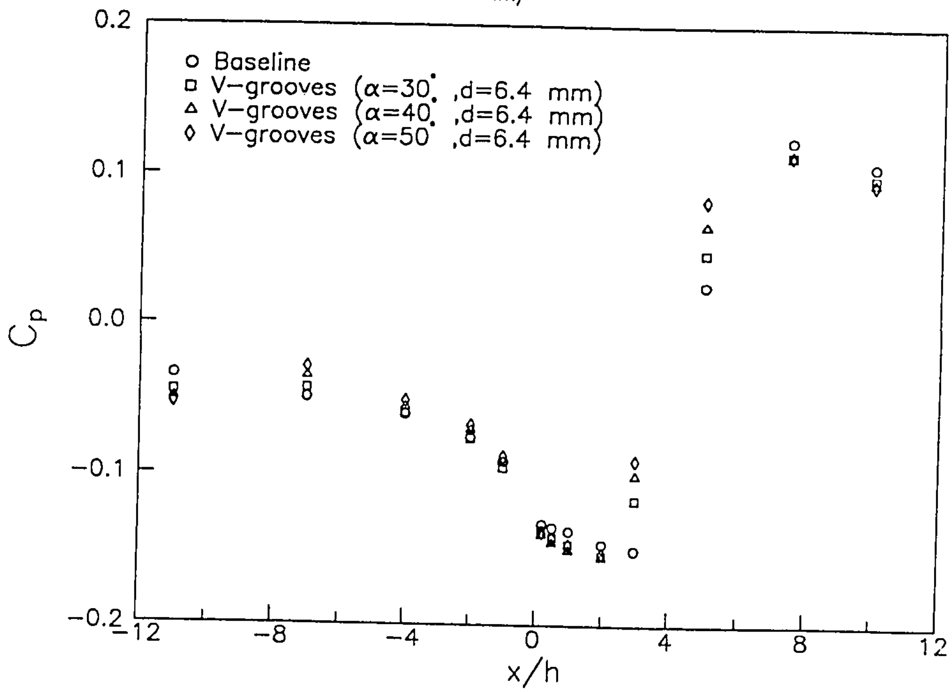

Fig. 3.15 Streamwise surface pressure variation for the unswept rearward-facing step with V-grooves (α = 30°; d = 6.4 and 9.5 mm)

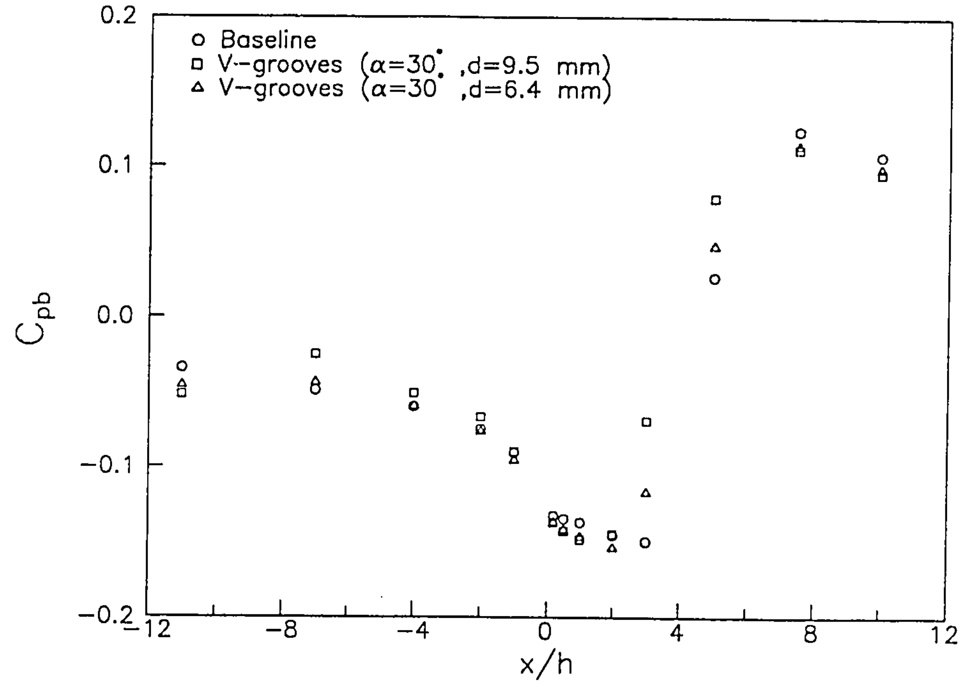

Fig. 3.16 Streamwise surface pressure variation for the unswept rearward-facing step with V-grooves (α = 50°, d = 6.4 mm) at U_∞ = 18.5 and 43 m/s

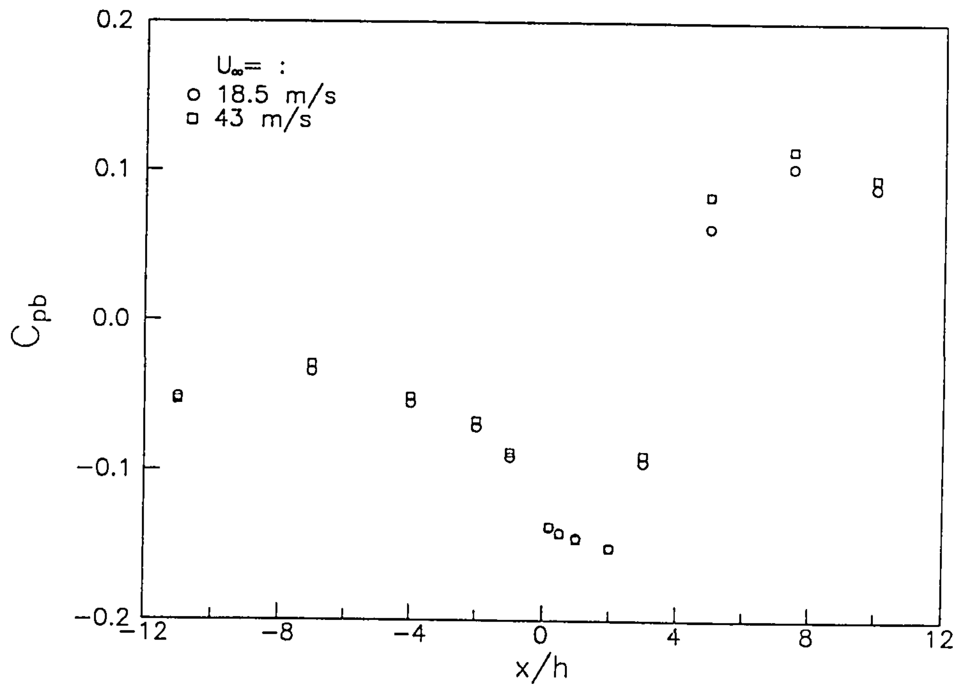

Fig. 3.17 Streamwise surface pressure variation for the unswept rearward-facing step with wishbone and doublet vortex generators

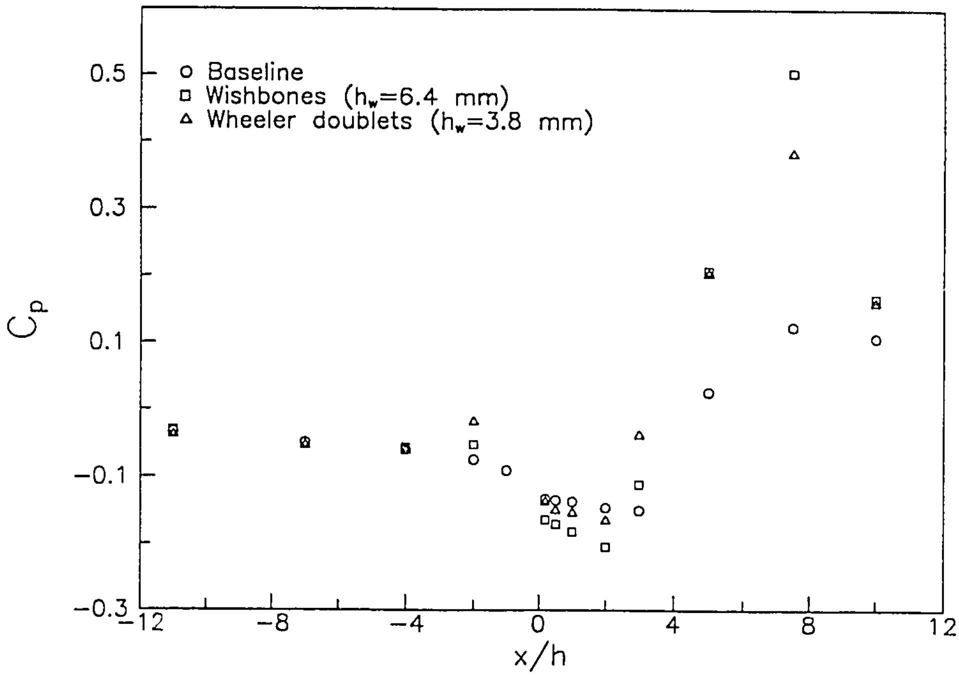

Fig. 3.18 Streamwise surface pressure variation for the unswept rearward-facing step with triangular serrations and base cavity

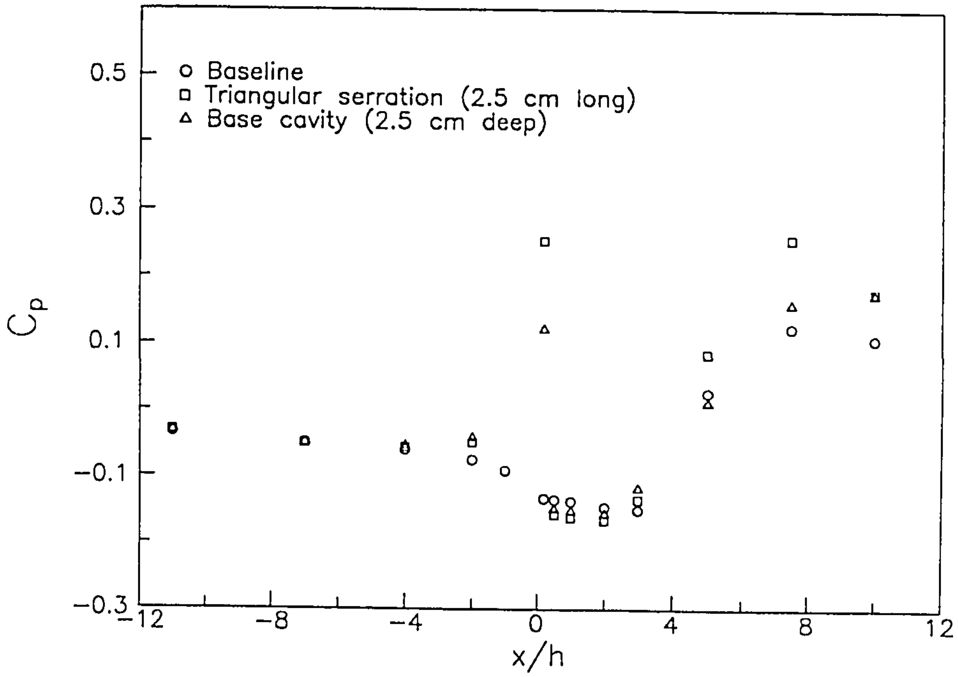

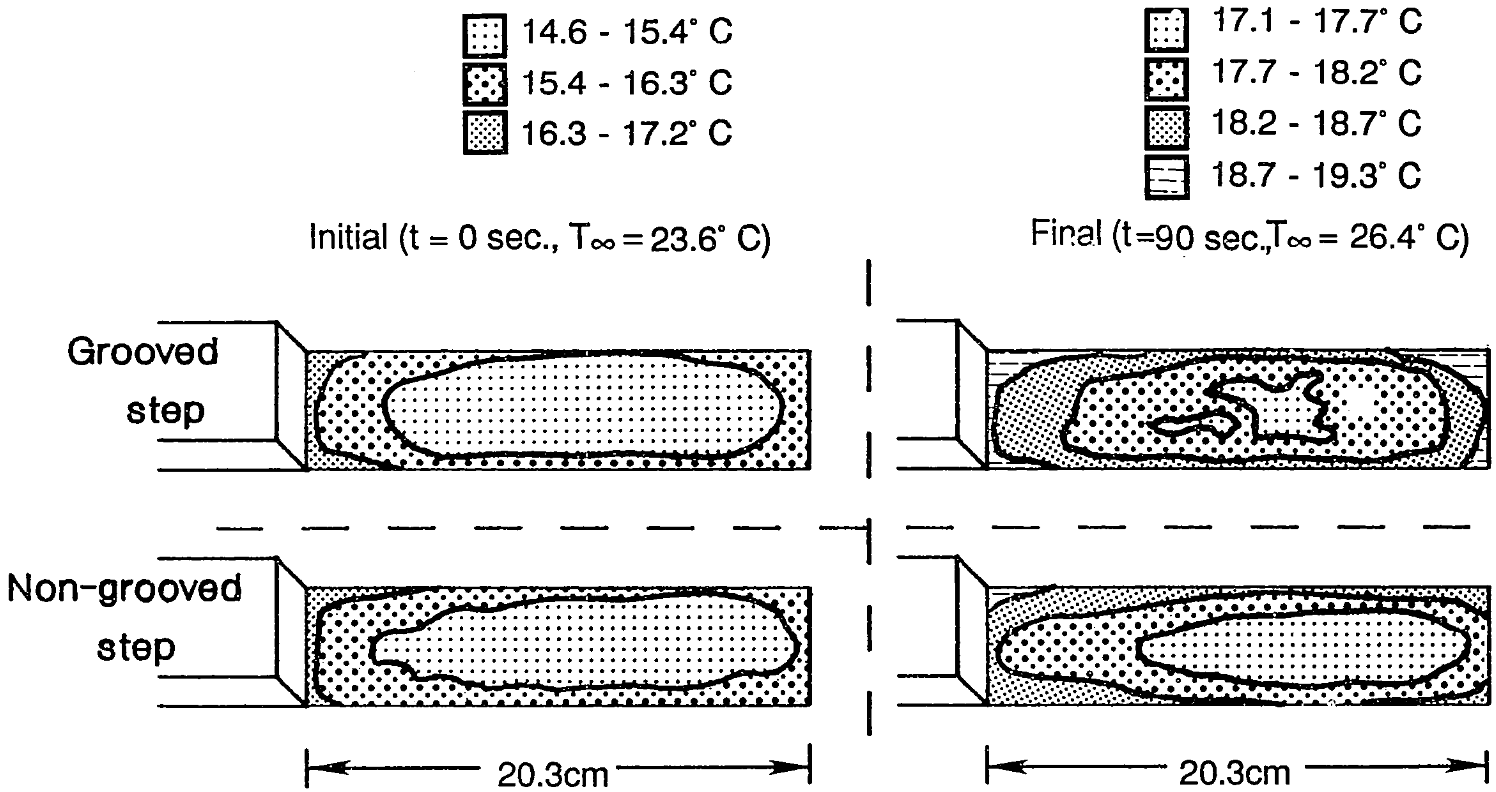

Fig. 3.19 Temperature contours in the separated-flow region for the 1.0 cm step (U_∞ = 9 m/s)

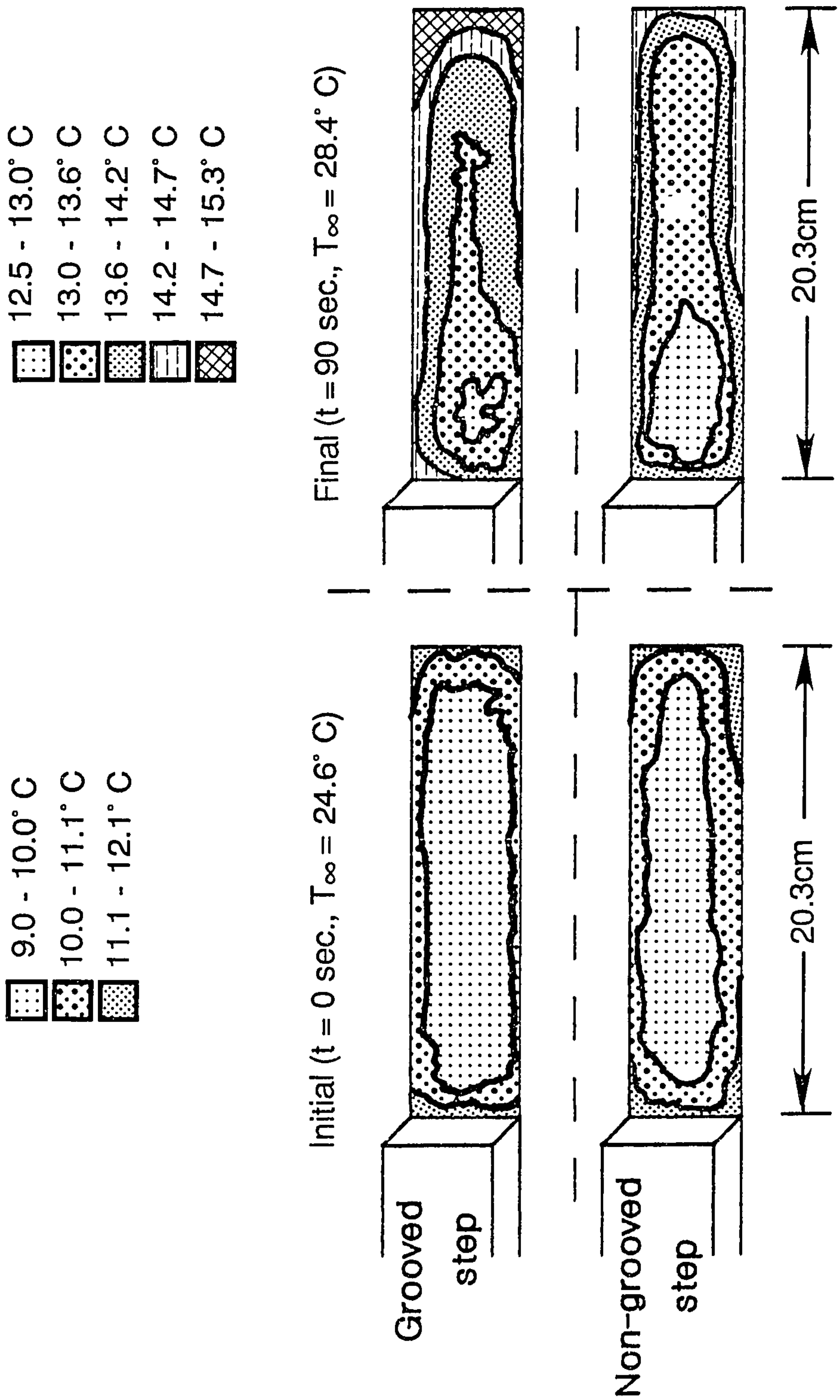

Fig. 3.20 Temperature contours in the separated-flow region for the 2.5 cm step (U_∞ = 9 m/s)

Fig. 3.21 Spanwise base and surface pressure variation at varying streamwise positions downstream of the baseline swept (β = 30°) rearward-facing step

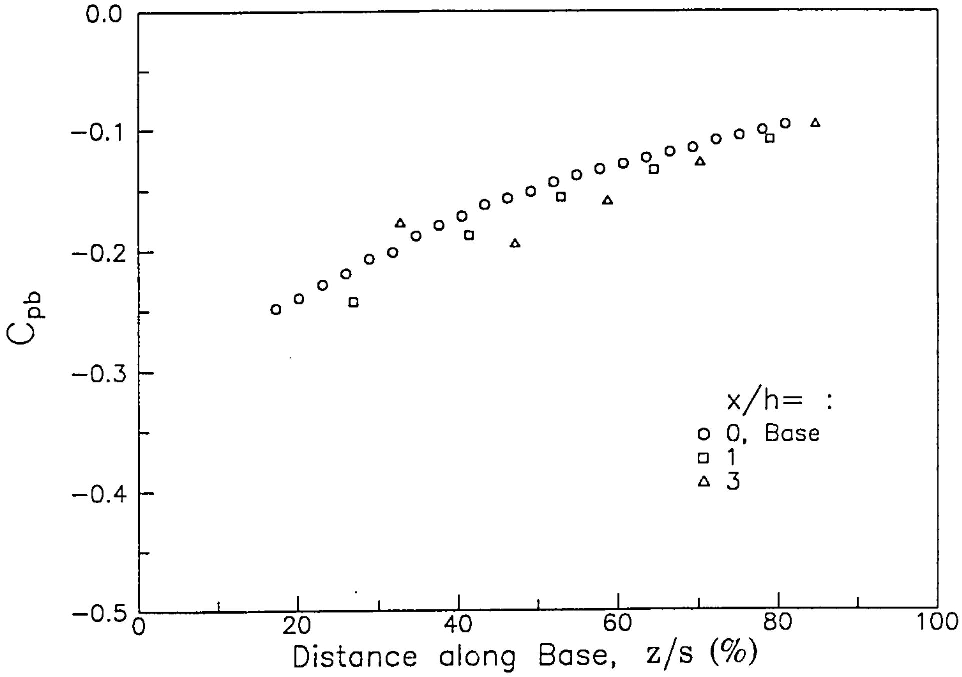

Fig. 3.22 Spanwise base and surface pressure variation at varying streamwise positions downstream of the swept (β = 30°) rearward-facing step with shallow rectangular grooves (w_r = 15 mm, d = 3 mm)

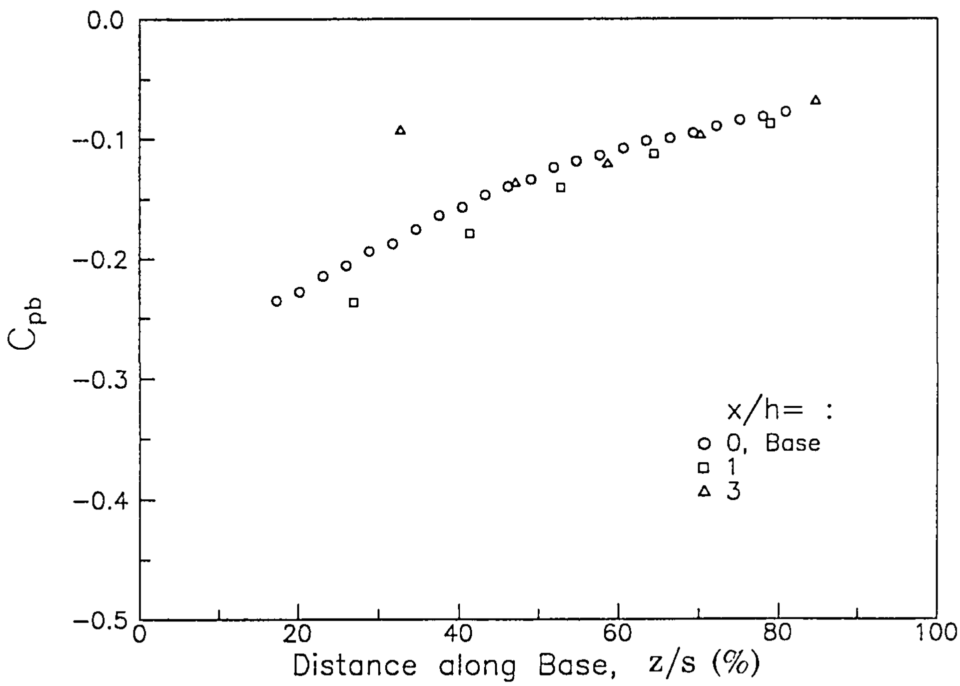

Fig. 3.23 Spanwise base and surface pressure variation at varying streamwise positions downstream of the swept (β = 30°) rearward-facing step with V-grooves (α = 50°, d = 6.4 mm)

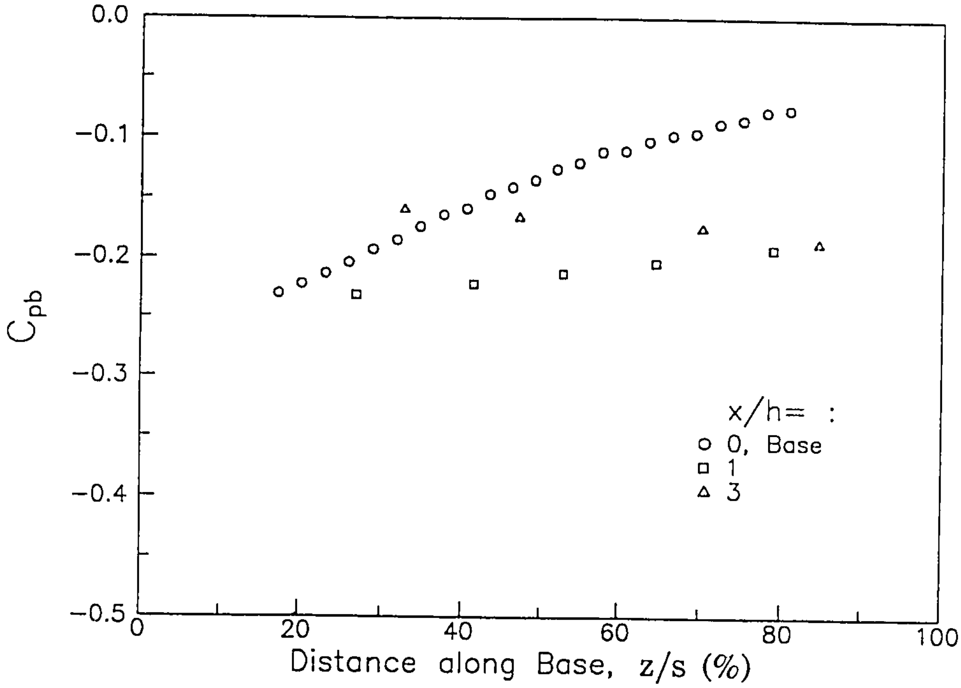

Fig. 3.24 Spanwise base and surface pressure variation at varying streamwise positions downstream of the swept (β = 30°) rearward-facing step with wishbone vortex generators (h_w = 6.4 mm)

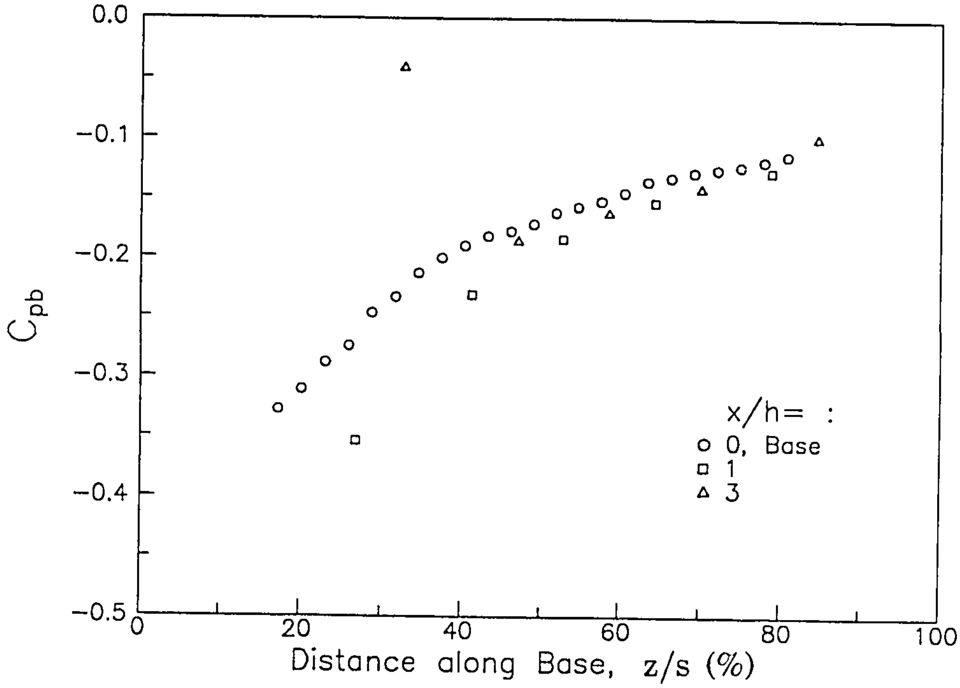

Fig. 3.25 Spanwise base and surface pressure variation at varying streamwise positions downstream of the swept (β = 30°) rearward-facing step with reversed wishbone vortex generators (h_w = 6.4 mm)

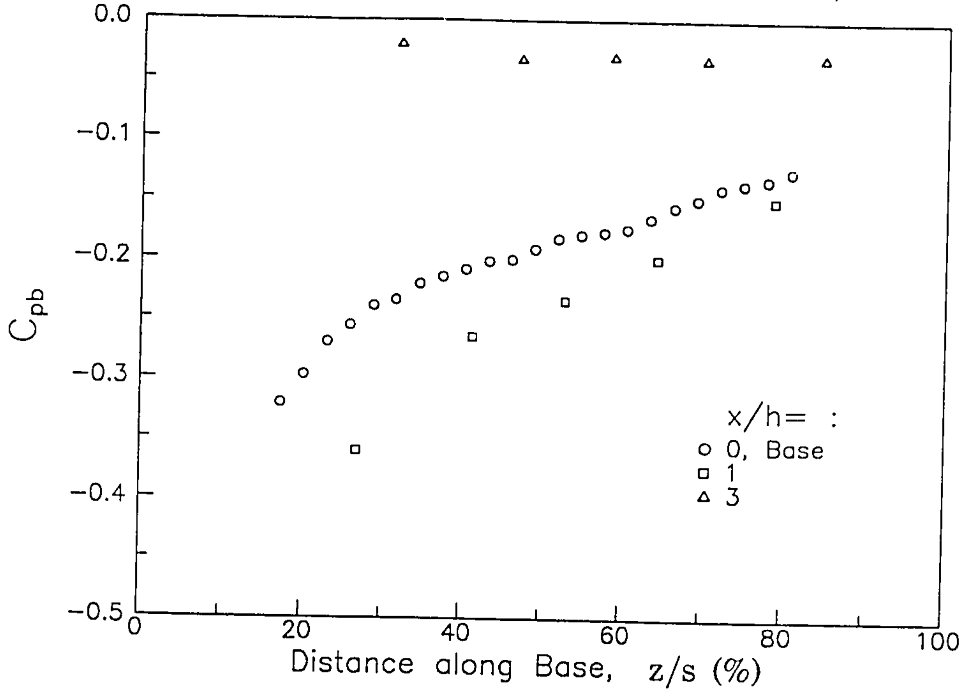

Fig. 3.26 Spanwise base and surface pressure variation at varying streamwise positions downstream of the swept (β = 30°) rearward-facing step with doublet vortex generators (h_w = 3.8 mm)

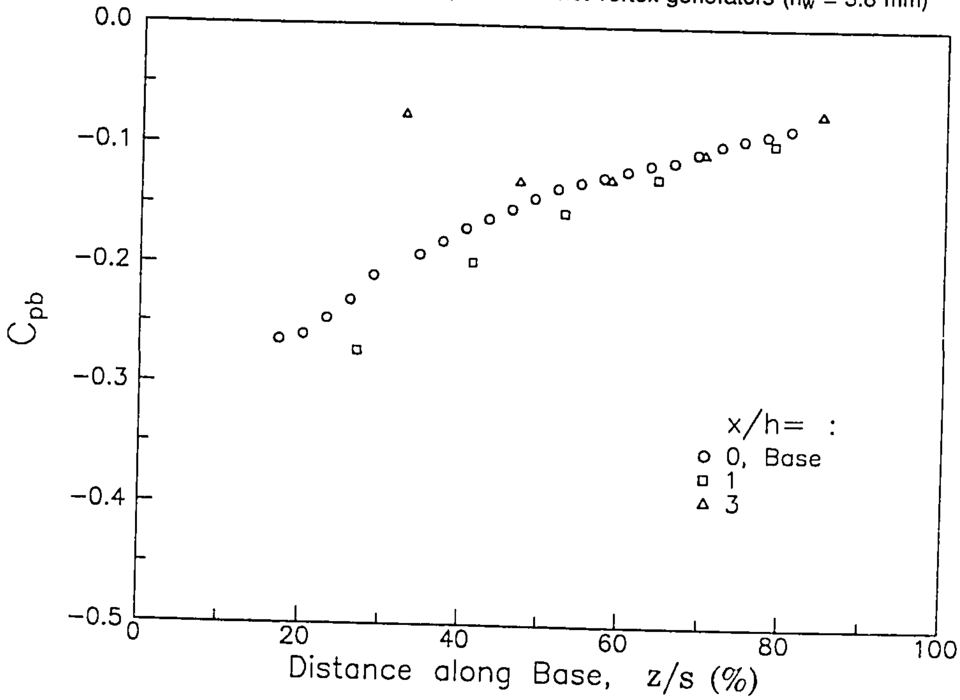

Fig. 3.27 Spanwise base and surface pressure variation at varying streamwise positions downstream of the swept (β = 30°) rearward-facing step with triangular serrations (2.5 cm long)

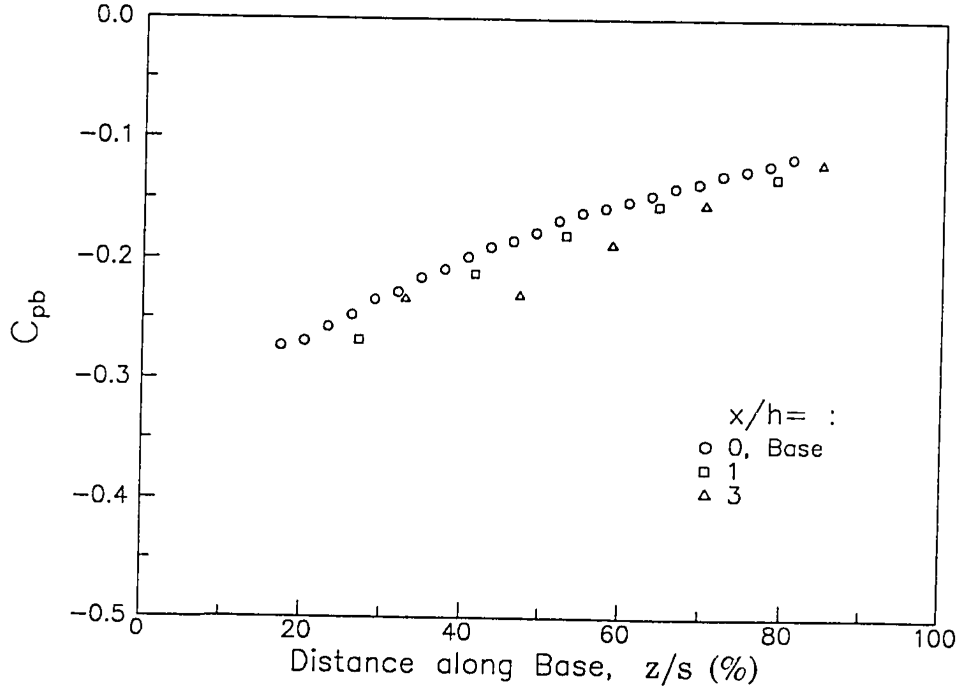

Fig. 3.28 Spanwise base pressure variation for the swept (β = 30°) rearward-facing step with grooves

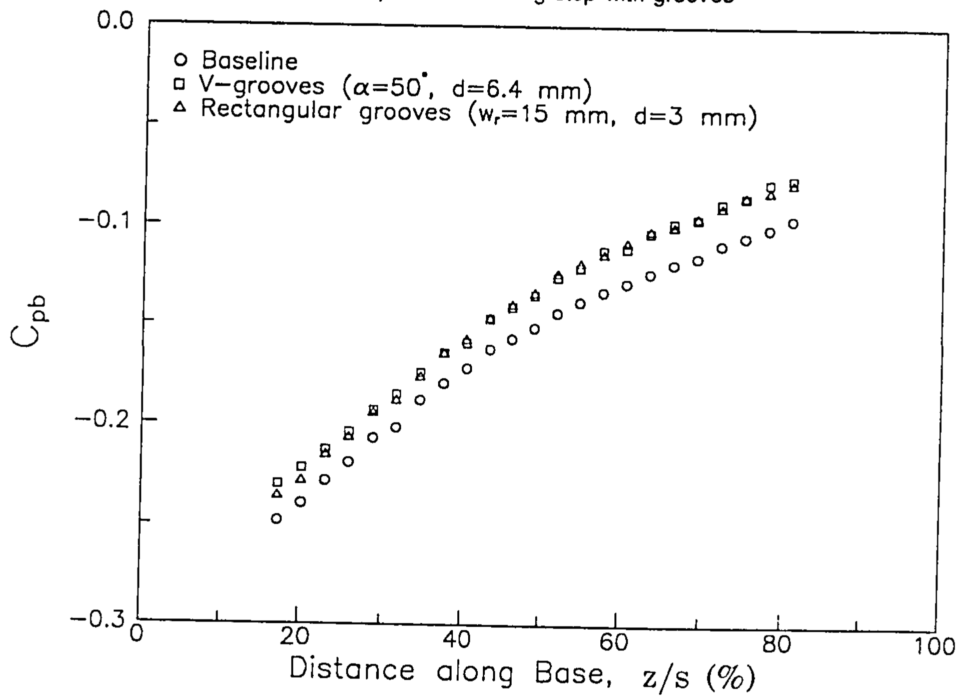

Fig. 3.29 Spanwise base pressure variation for the swept (β = 30°) rearward-facing step with vortex generators

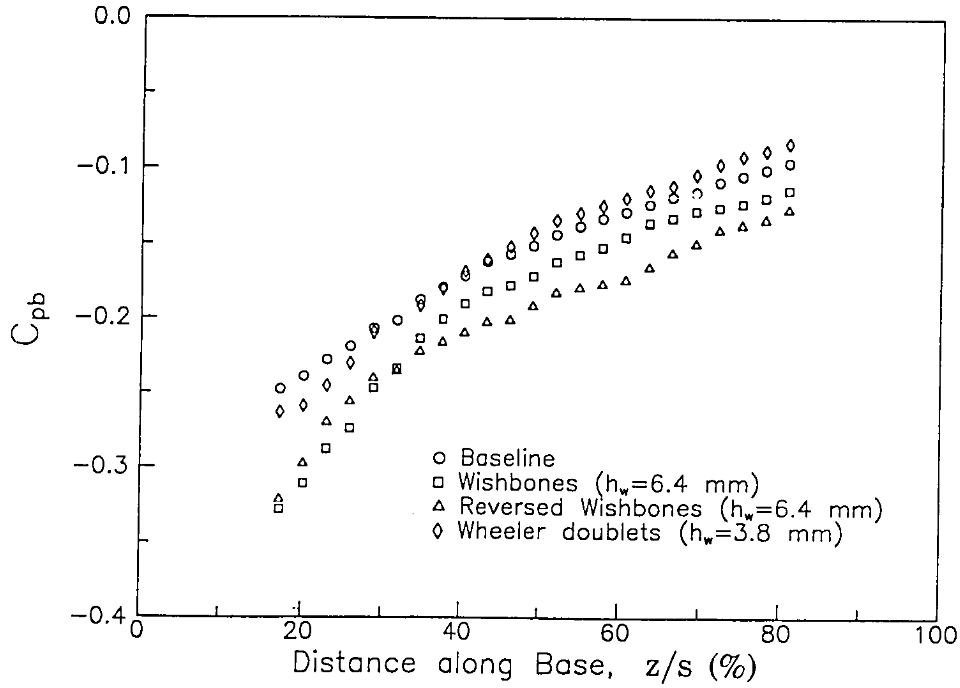

Fig. 3.30 Spanwise base pressure variation for the swept (β = 30°) rearward-facing step with serrations and fences

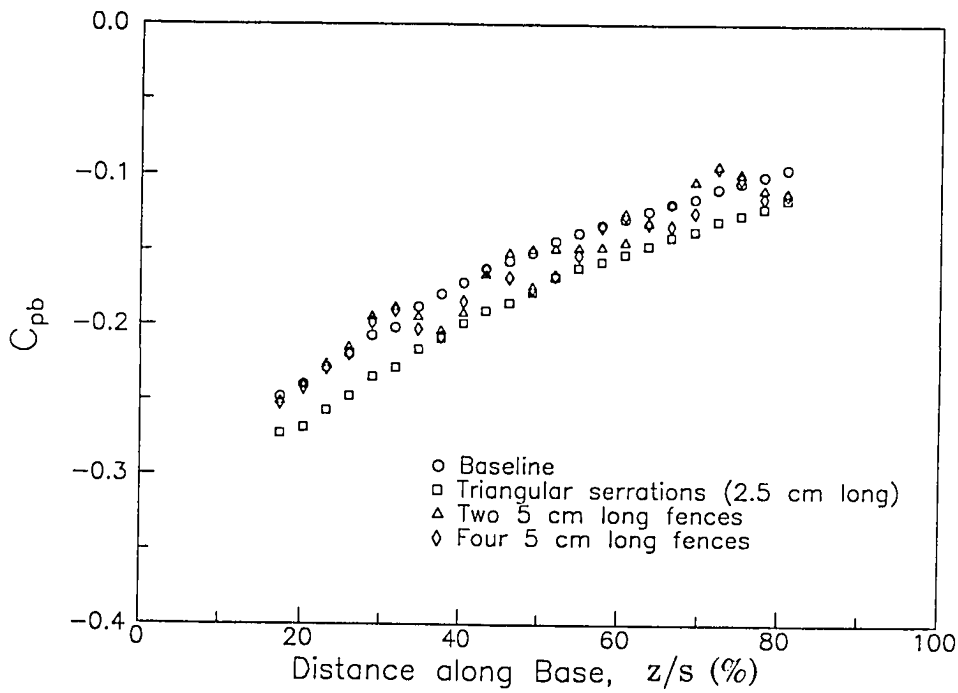

Fig. 3.31 Spanwise base and surface pressure variation at varying streamwise positions downstream of the baseline swept (β = 45°) rearward-facing step

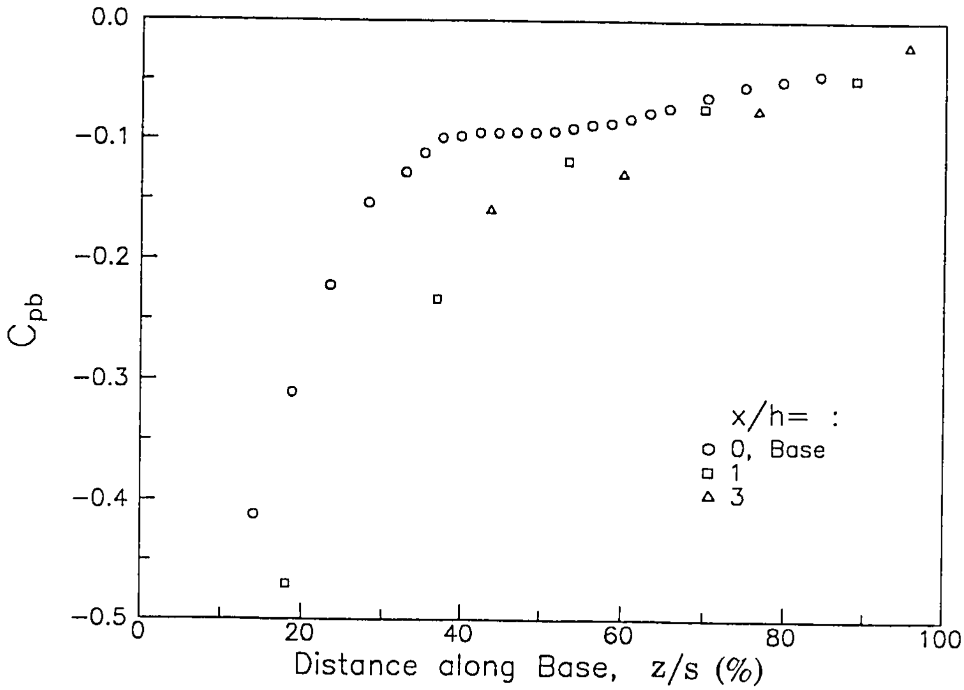

Fig. 3.32 Spanwise base and surface pressure variation at varying streamwise positions downstream of the swept (β = 45°) rearward-facing step with V-grooves (α = 50°, d = 6.4 mm)

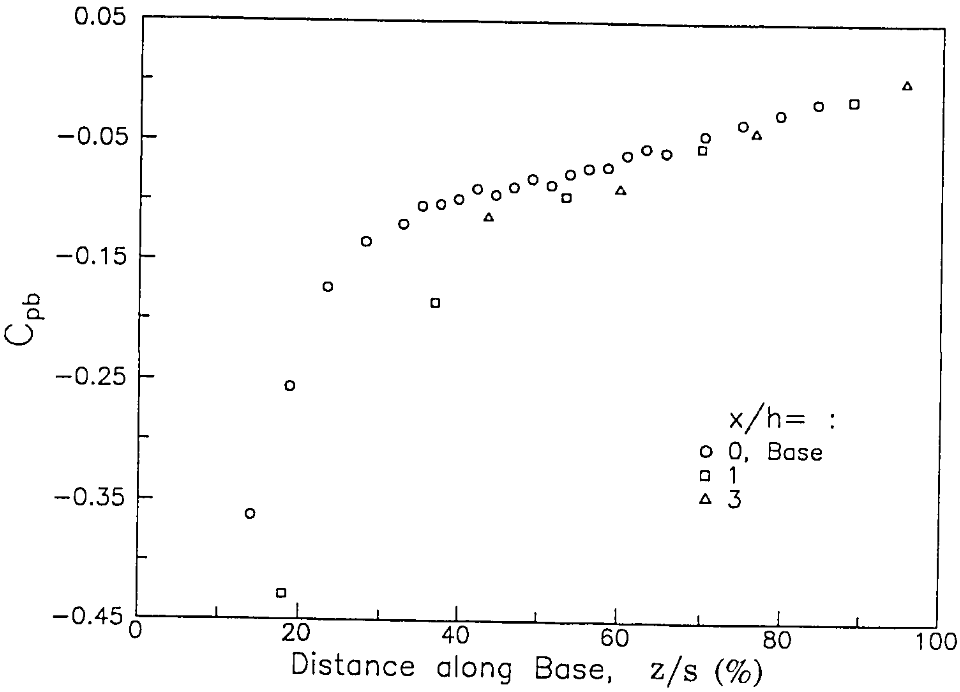

Fig. 3.33 Spanwise base and surface pressure variation at varying streamwise positions downstream of the swept (β = 45°) rearward-facing step with reversed wishbone vortex generators (h_w = 6.4 mm)

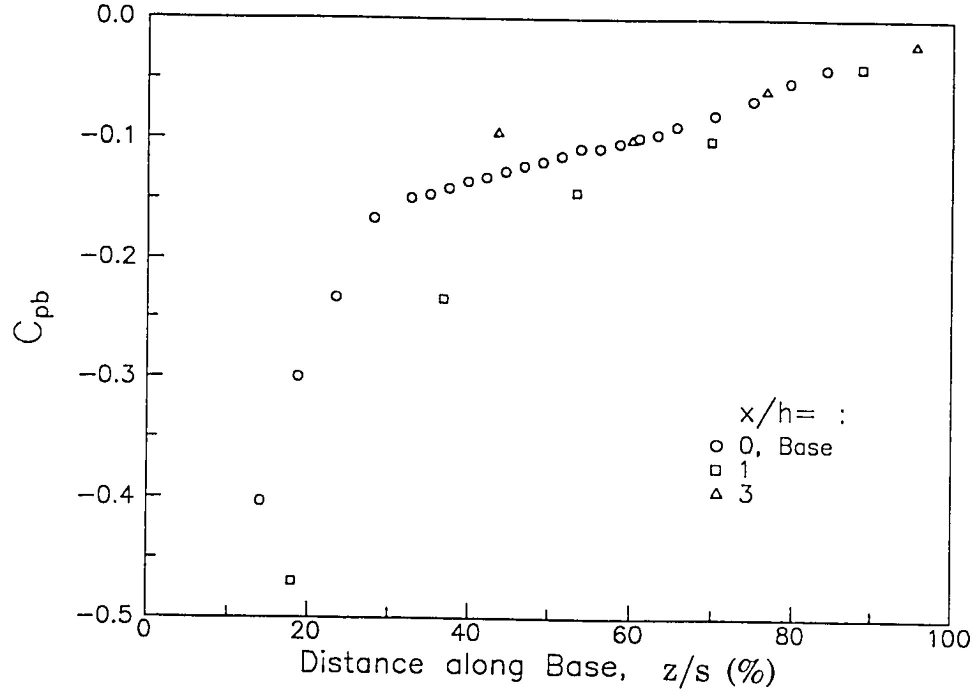

Fig. 3.34 Spanwise base pressure variation for the swept (β = 45°) rearward-facing step with wishbone vortex generators

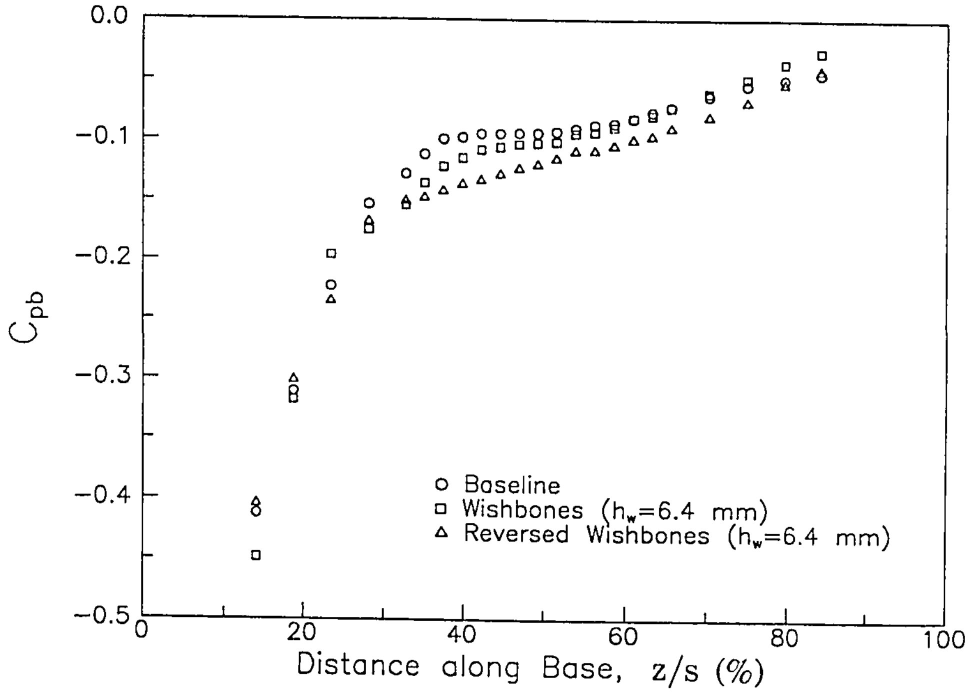

Fig. 3.35 Spanwise base pressure variation for the swept (β = 45°) rearward-facing step with V-grooves and fences

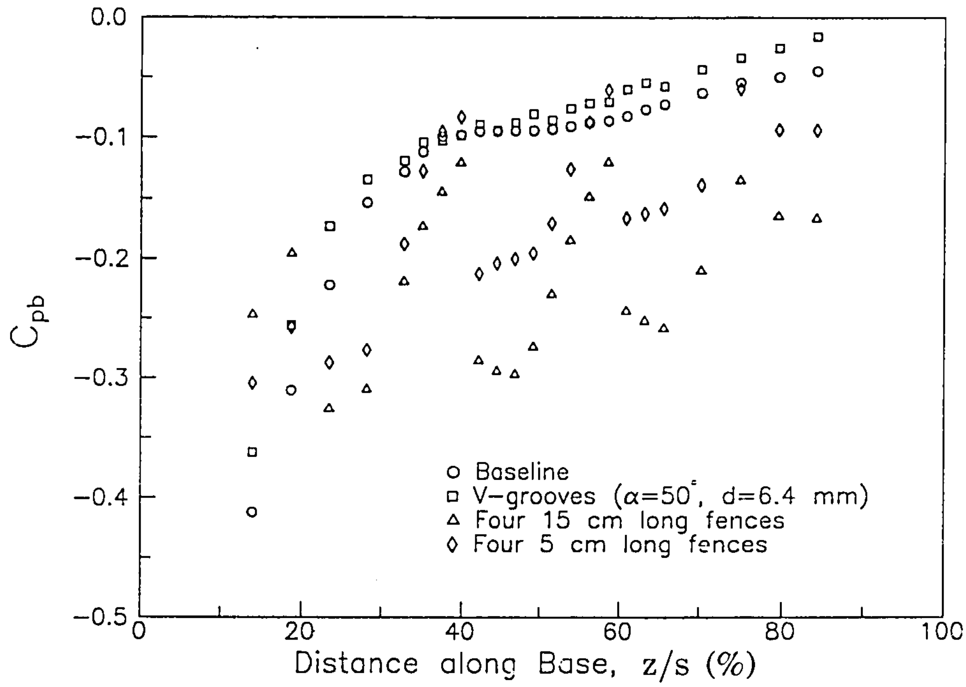

Fig. 3.36 Streamwise surface pressure variation for the swept rearward-facing step (β = 30°) with rectangular grooves (w_r = 15 mm, d = 3 mm)

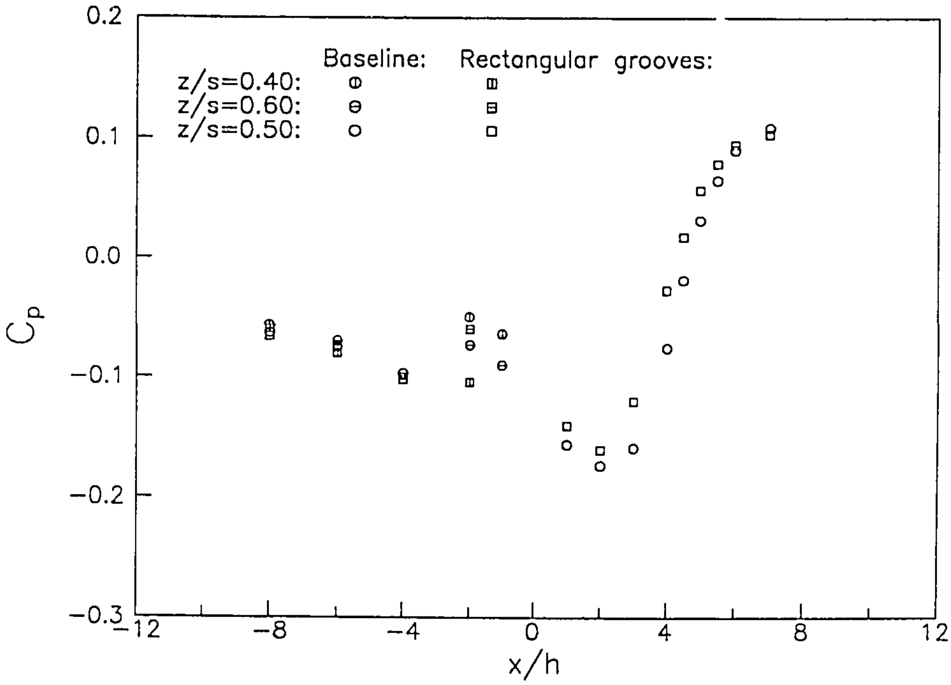

Fig. 3.37 Streamwise surface pressure variation for the swept rearward-facing step (β = 30°) with wishbone (h_w = 6.4 mm) vortex generators

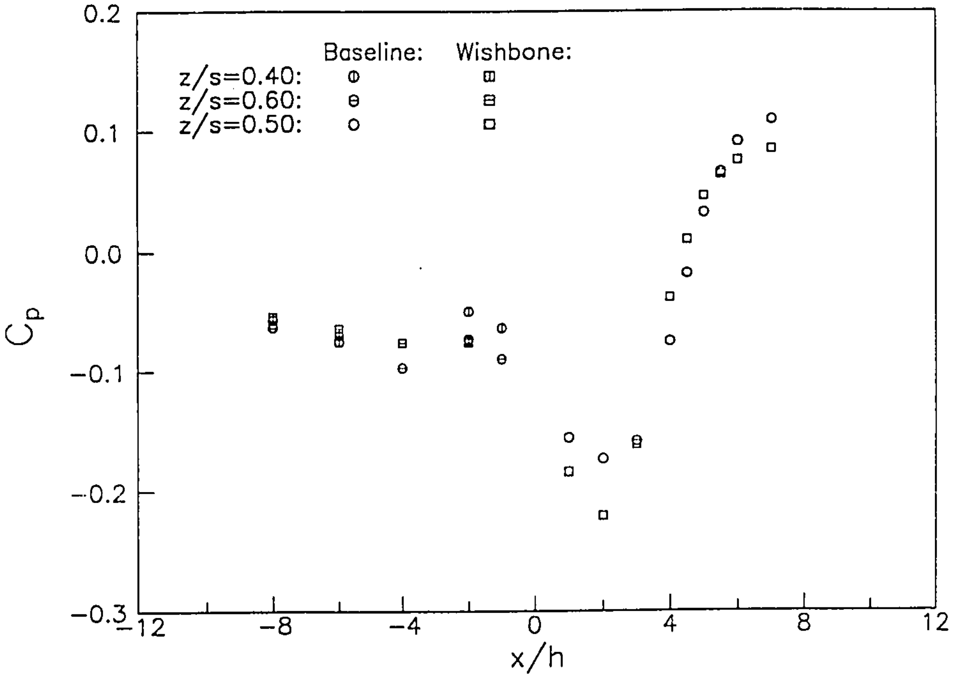

Fig. 3.38 Streamwise surface pressure variation for the swept rearward-facing step (β = 30°) with reversed wishbone (h_w = 6.4 mm) vortex generators

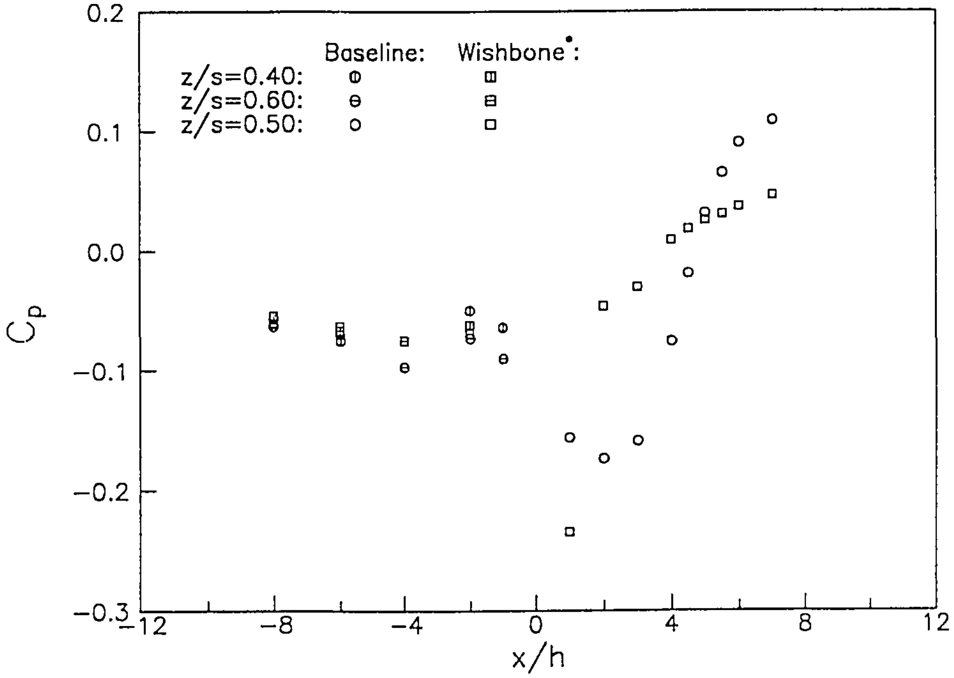

Fig. 3.39 Streamwise surface pressure variation for the swept rearward-facing step (β = 30°) with doublet (h_w = 3.8 mm) vortex generators

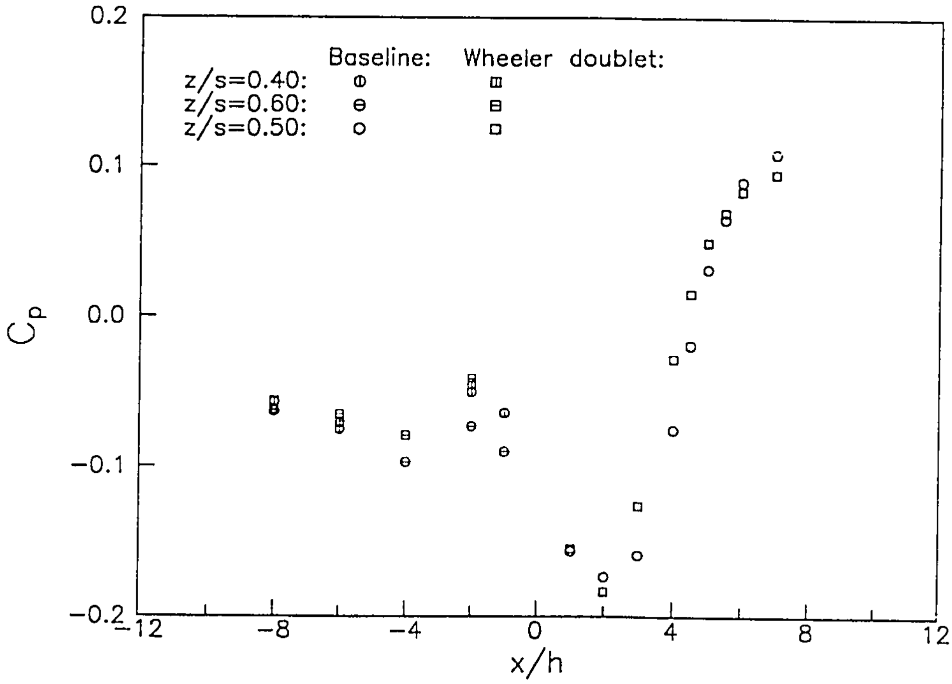

Fig. 3.40 Streamwise surface pressure variation for the swept rearward-facing step (β = 30°) with triangular serrations (2.5 cm long)

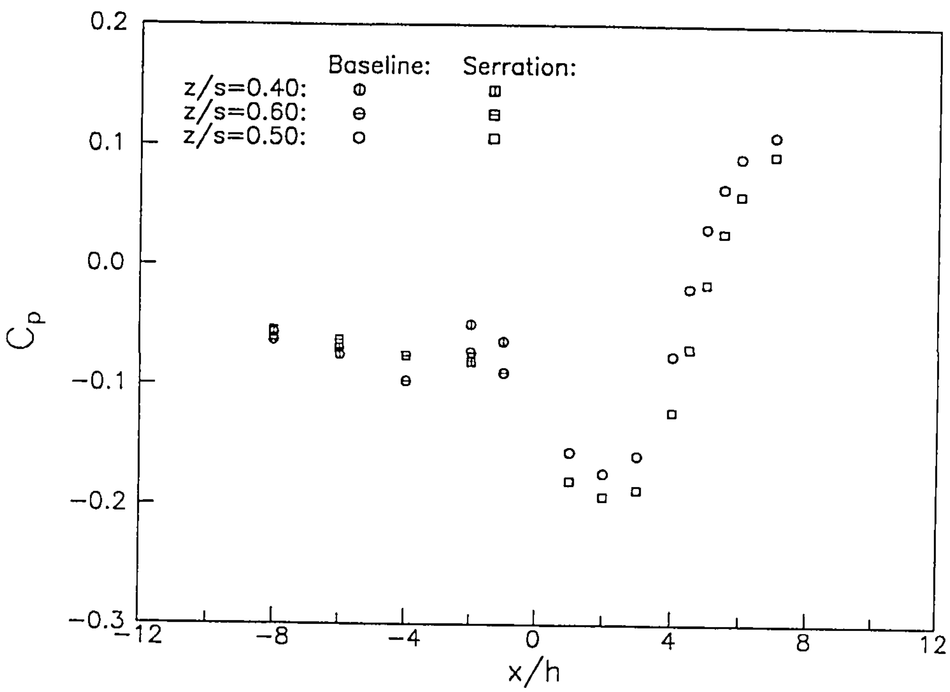

Fig. 3.41 Streamwise surface pressure variation for the swept rearward-facing step (β = 30°) with two triangular fences (5 cm long)

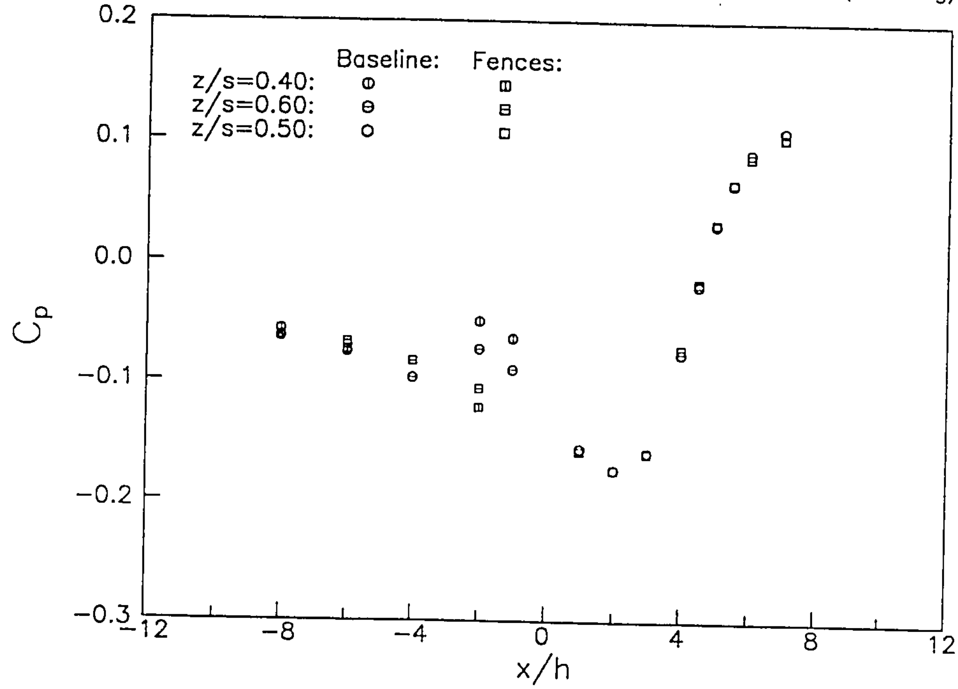

Fig. 3.42 Streamwise surface pressure variation for the swept rearward-facing step (β = 45°) with V-grooves (α = 50°, d = 6.4 mm)

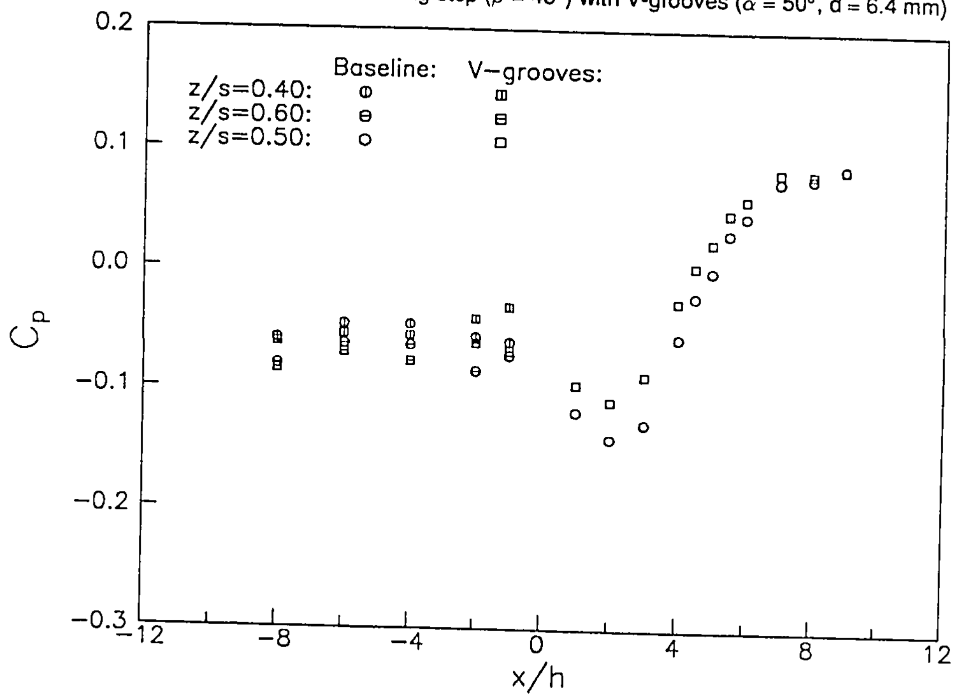

Fig. 3.43 Streamwise surface pressure variation for the swept rearward-facing step (β = 45°) with wishbone (h_w = 6.4 mm) vortex generators

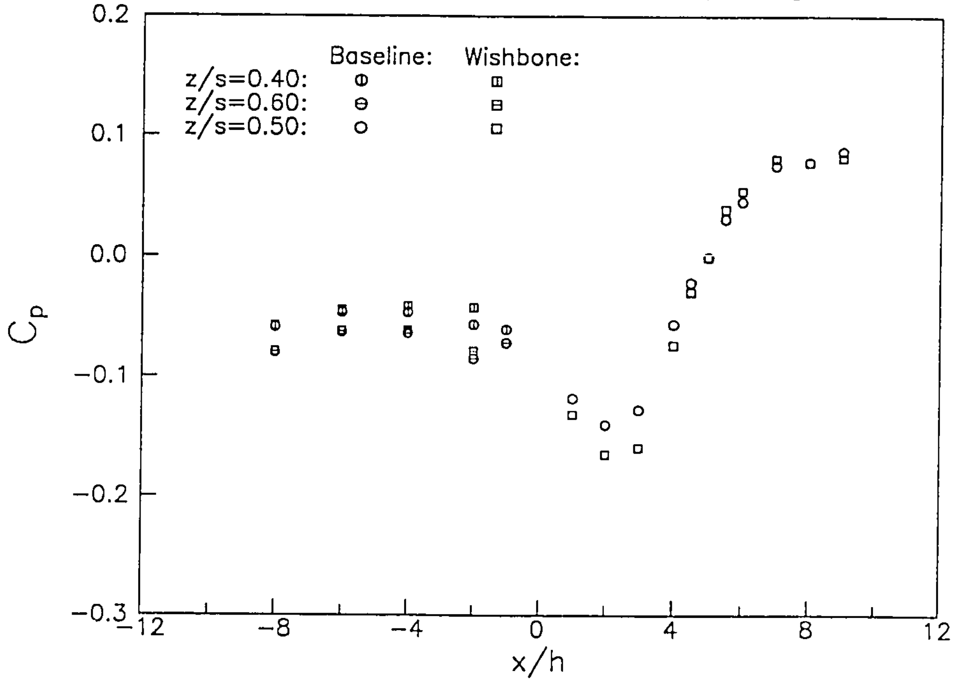

Fig. 3.44 Streamwise surface pressure variation for the swept rearward-facing step (β = 45°) with reversed wishbone (h_w = 6.4 mm) vortex generators

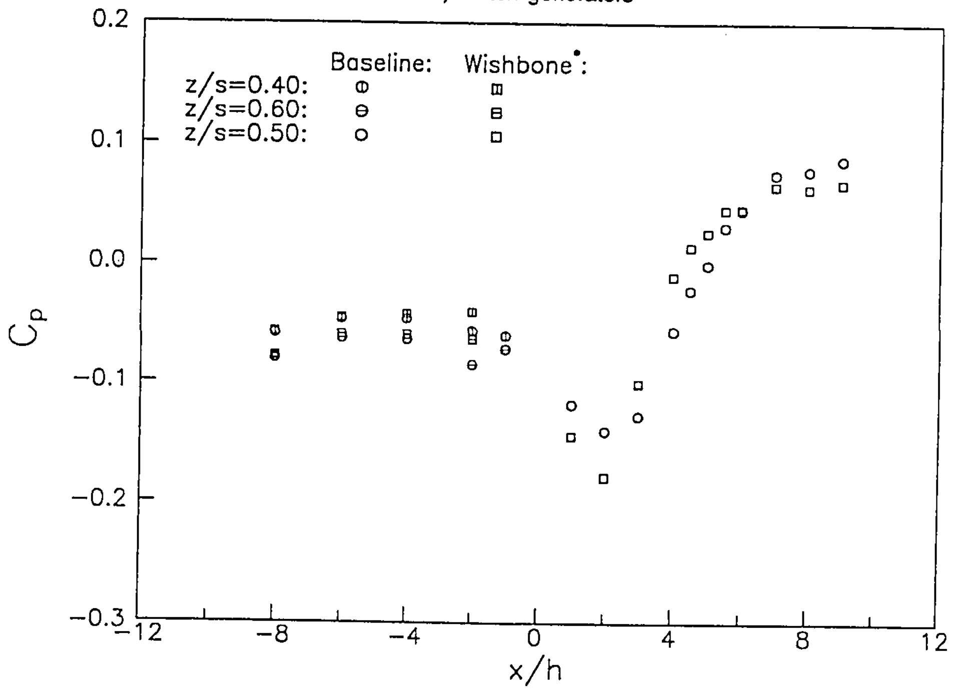

Fig. 3.45 Streamwise surface pressure variation for the swept rearward-facing step (β = 45°) with four triangular fences (5 cm long)

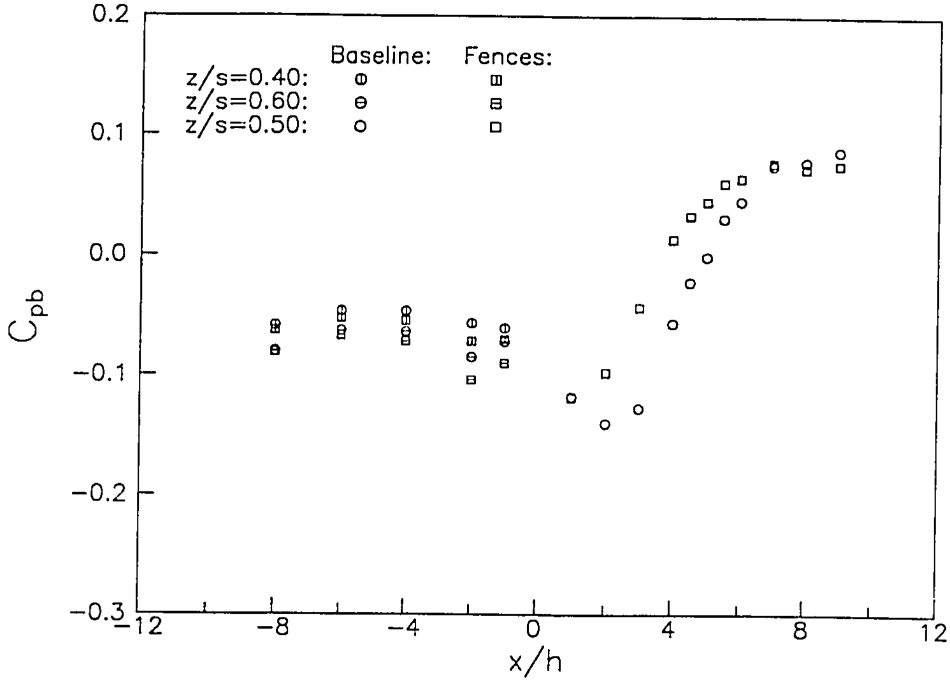

Fig. 3.46 Streamwise surface pressure variation for the swept rearward-facing step (β = 45°) with four triangular fences (15.2 cm long)

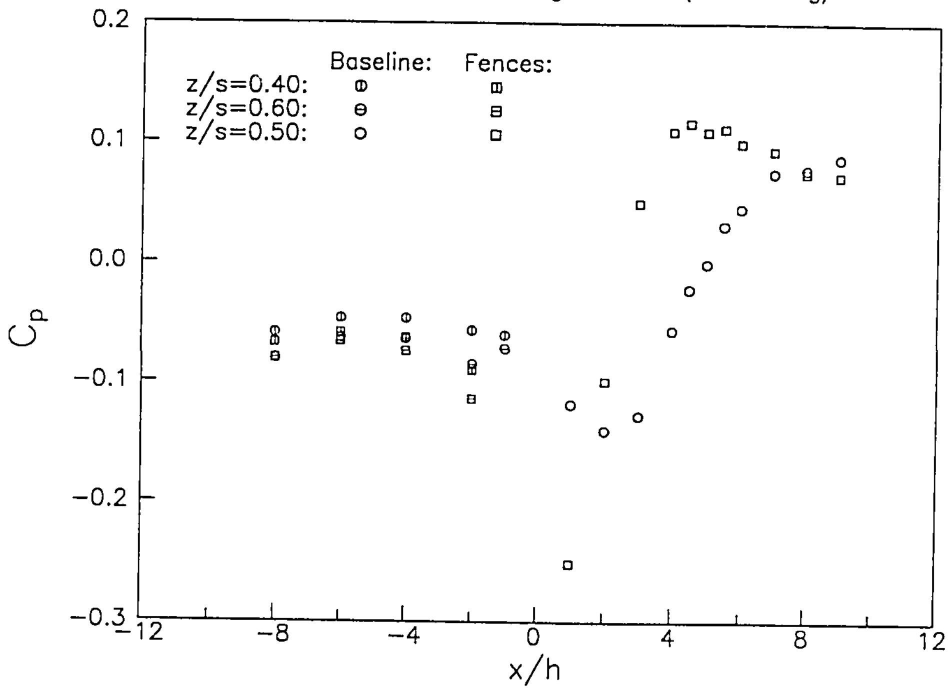

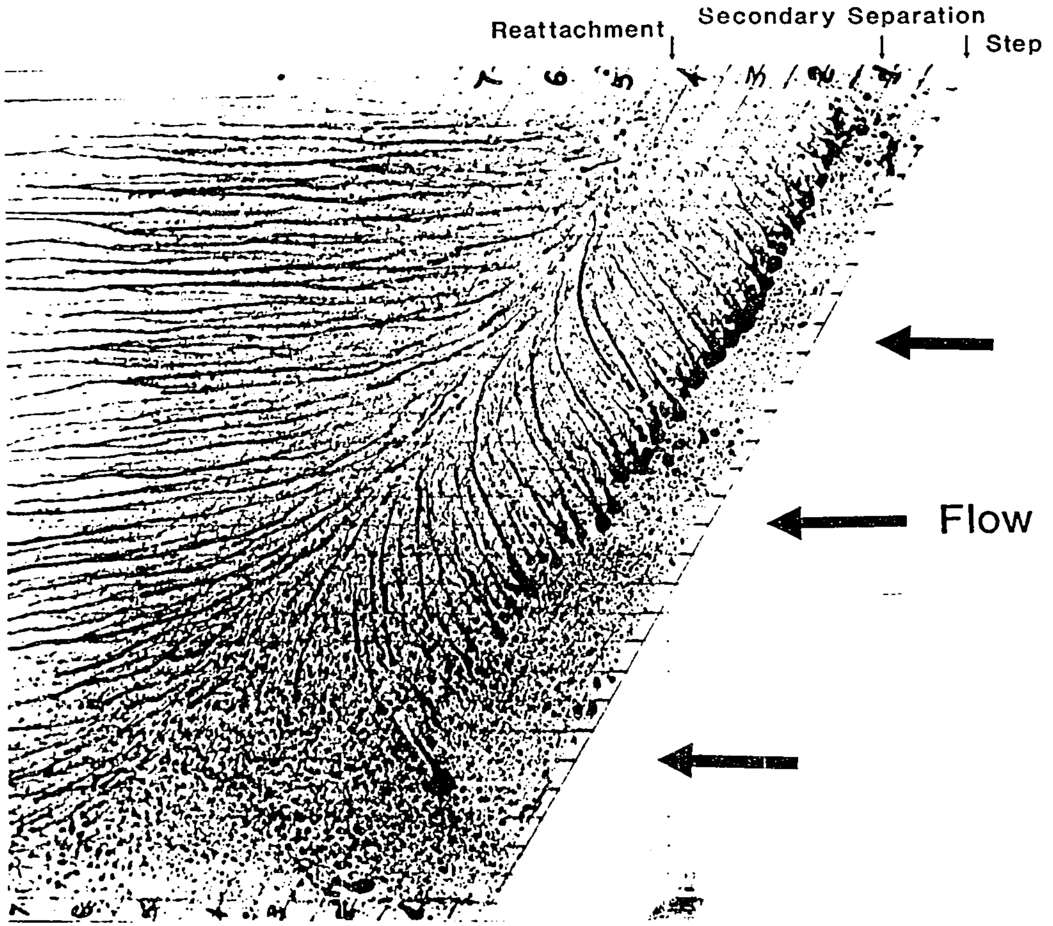

Fig. 3.47 Oil-drop flow visualization photograph for baseline rearward-facing step (h = 2.5 cm, U_∞ = 43 m/s)

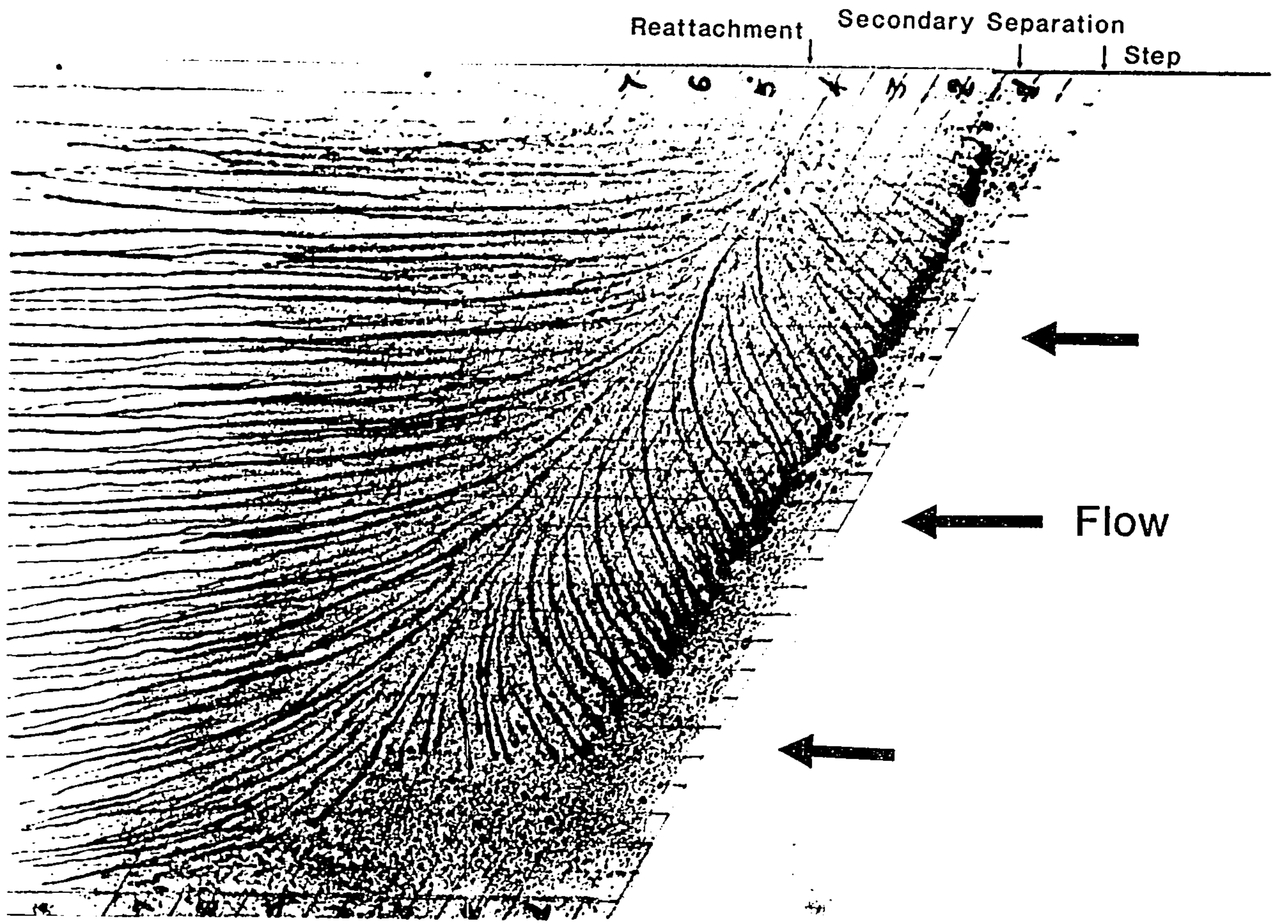

Fig. 3.48 Oil-drop flow visualization photograph for the 30° swept rearward-facing step with 50° V-grooves (h = 2.5 cm, U_∞ = 43 m/s)

Fig. 3.49 Reattachment line for flow over the swept (β = 30°) rearward-facing step with V-grooves (α = 50°)

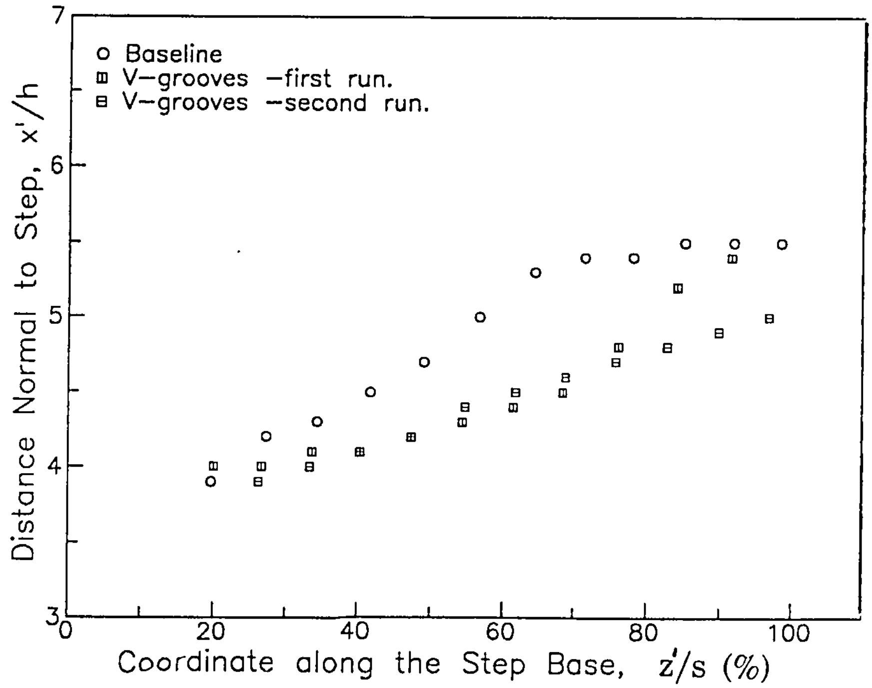

Fig. 3.50 Reattachment line for flow over the swept (β = 30°) rearward-facing step with triangular serrations

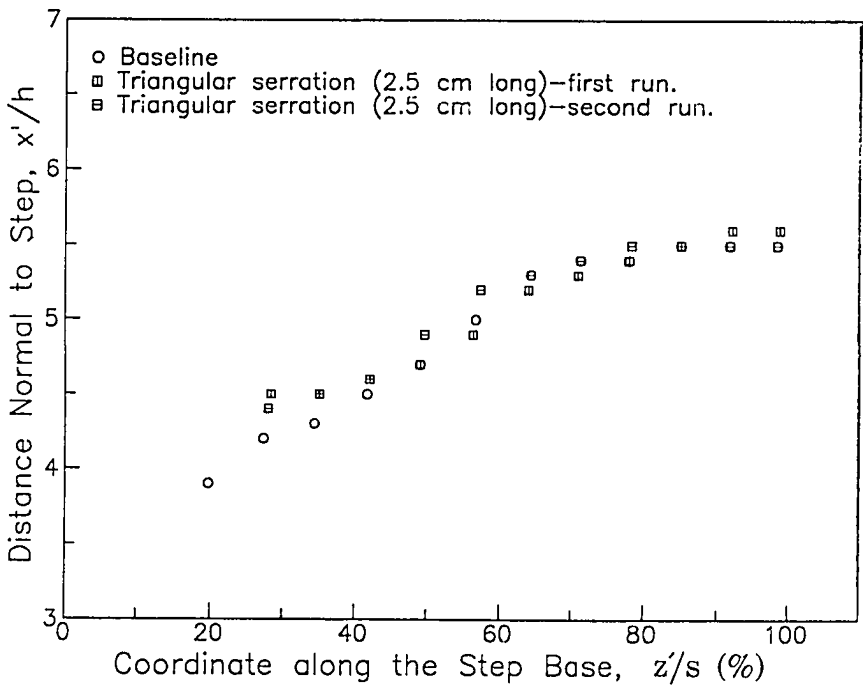

Fig. 3.51 Reattachment line for flow over the swept (β = 45°) rearward-facing step with V-grooves (α = 50°)

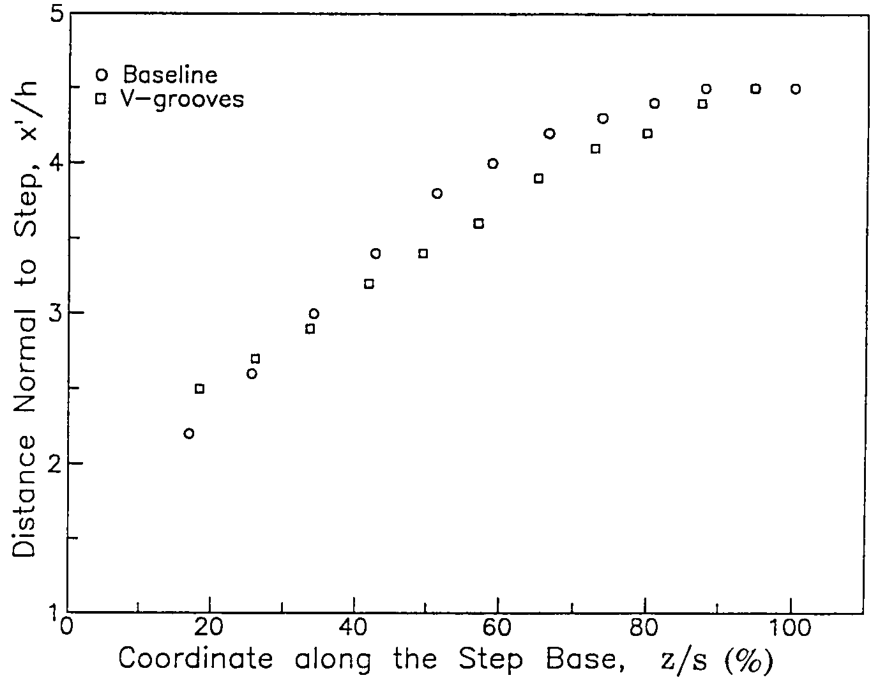

Fig. 3.52 Reattachment line for flow over the swept (β = 45°) rearward-facing step with wishbone and doublet vortex generators

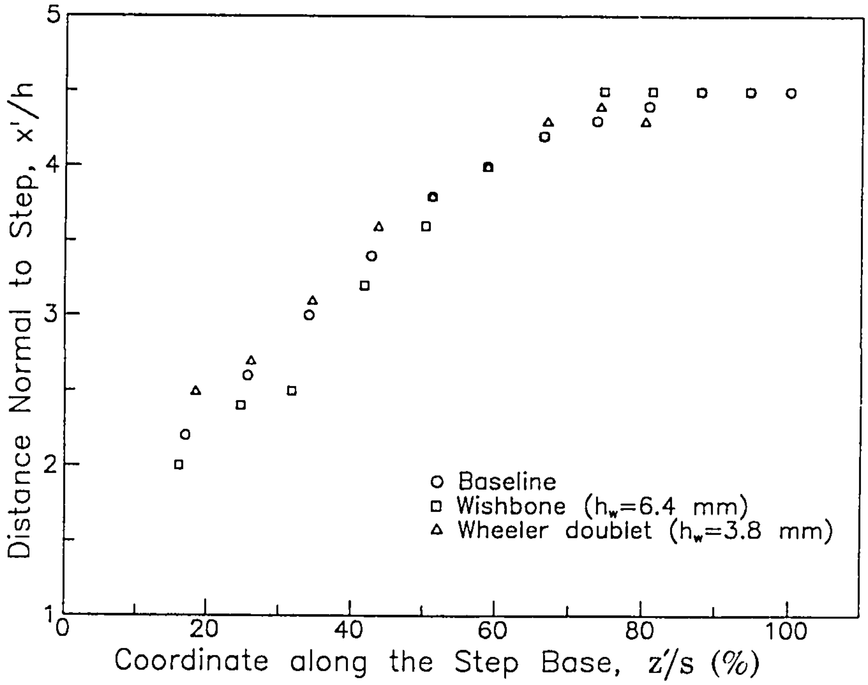

Fig. 3.53 Reattachment line for flow over swept (β = 45°) rearward-facing step with triangular fences

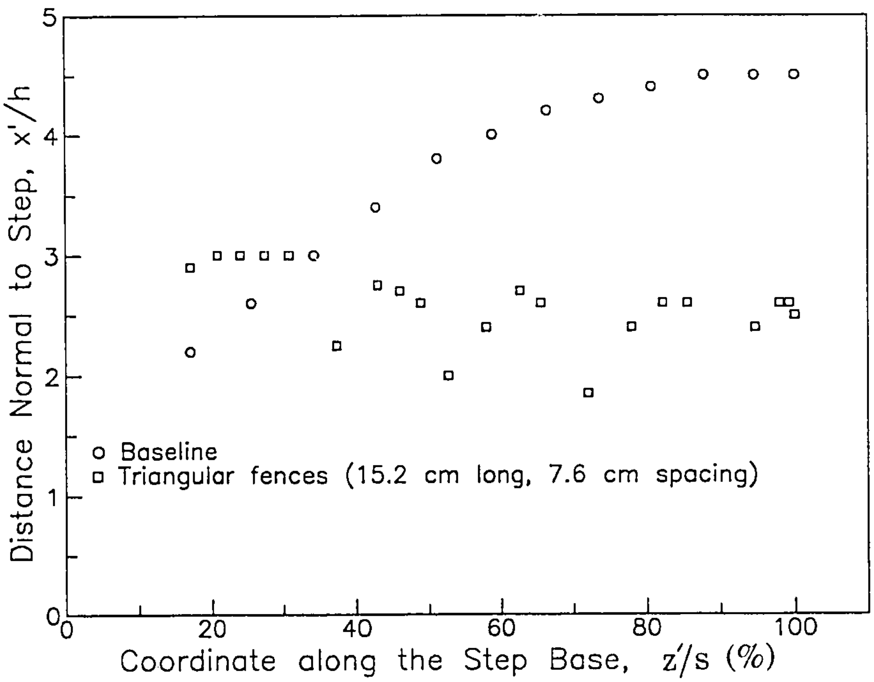

Chapter 4

DISCUSSION OF FLAT-PLATE AIRFOIL RESULTS

4.1 2–D Flat-Plate Airfoil

Boundary-layer velocity profiles at three spanwise locations for the top and bottom surfaces of the model at 2.54 cm upstream of the base are presented in figures A.5 and A.6 for a free-stream speed of 17 m/s. Comparison of the profiles on each surface at the three locations indicates spanwise uniformity in the flow. Figures A.7 and A.9 contain velocity profiles at midspan for the top and bottom surface at free-stream speeds of 17 and 43 m/s, respectively. The close agreement between the two profiles is an indication of uniform flow over the model. The related power-law velocity profiles for these data confirm (figures A.8 and A.10) the turbulent nature of the flow in the boundary layer.

4.1.1 Base Pressure

In figure 4.1, the base pressure variation for V-grooves of varying depth (α = 30°) as a function of model span is shown. A trend toward increasing base pressure with increasing V-groove depth is evident from the plot. Grooves with d > 7.9 mm apparently create a more uniform two-dimensional pressure variation along the base. Similar data establishing a groove angle effect (d = 6.4 mm) is shown in figure 4.2. Grooves with the largest total included angle in the interval tested had the largest pressure increase compared to the baseline level. The largest groove angles had the effect of creating a more uniform pressure distribution along the model base. End effects are more pronounced with decreasing groove depth and groove angle. Apparently, the introduction of three-dimensional flow structures via V-grooves causes the flow to become more truely two-dimensional. In addition, the effect of groove angle on base pressure was most significant for groove angles of 30° or higher. Maximum increases in base pressure (50 to 60%) were obtained with α = 50° (d = 6.4 mm) and d = 9.5 mm (α = 30°). This level of base pressure increase is comparable to that obtained by Bearman [13] for active bleed through the base of a two-dimenisonal blunt trailing-edge airfoil. At Mach number of 0.1 and a flow coefficient, C_q of 0.13, Bearman obtained a 65% increase in base pressure coefficient. Flow coefficient defined similarly for the present study, is the ratio of volumetric flow rate through the grooves (Q_G) to the product of freestream velocity times base area. The value of flow coefficient calculated for the present test (50° grooves) was 0.13 assuming uniform flow through the grooves.

The average base-pressure coefficient, $\overline{C_{pb}}$, was calculated for each groove angle tested (d = 6.4 mm) from the C_{pb} data using area weighting. The average base-pressure coefficient calculated for each model is plotted as a function of groove angle for free-stream speeds of 17 m/sec and 42 m/sec in figure 4.3. There is almost a linear relationship between the mean base pressure and groove angle for the range of the angles tested.

Results of further testing to examine the effect of groove length on the base pressure are presented in figures 4.4 and 4.5 for V-grooves with α = 50°. According to these results, shortening the groove length had the effect of increasing the base pressure. This increase in base pressure, however, does not appear to be significant between the 5 cm long grooves and the 25 cm long grooves tested initially. Inspection of the base pressure profiles for the V-grooves of various lengths (α = 50°) in figures 4.3 and 4.4 indicates that shortening the V-groove length below 5 cm results in an increase in the base pressure down to a groove length of 6.4 mm. Tests with 6.4 mm long grooves resulted in a significant drop in the base pressure below the values obtained with the 25 cm long V-grooves. The optimum groove length appears to be approximately 13 to 25 mm. Testing V-grooves with $\alpha = 30°$ and d = 6.4 mm also indicated that shortening the groove length increased the base pressure. The optimum groove length for these latter tests was also 13 mm (figure 4.6). Further testing with deep rectangular grooves (7.7 mm$\times$6.4 mm) indicated an optimum groove length of approximately 50 mm for the highest base pressure (figure 4.7). Reducing or increasing the groove length from that value resulted in a drop in the base pressure.

The base pressure distribution is more uniform for the optimum groove length than for the other lengths examined. In addition to the effect produced from the introduction of high-momentum fluid into the wake via grooves, the shorter grooves also may cause flow deflection toward the model surfaces in the vicinity of the base of the model. This flow deflection is due to the steps on the model surfaces caused by the grooves.

The end plates (side walls) associated with the 2-D wake model were extended 41 cm beyond the base of the model in order to reduce end effects. At that time, a few modifications were re-tested and additional modifications were tested for the first time. These data are presented in figure 4.8 to 4.11. The new data for the V-groove modifications (figure 4.8) appear to be more symmetrical about the model centerline and more uniform than the old data (figures 4.1 and 4.2). However, qualitative comparisons between the new data are similar to the comparisons between old data sets. For example, the mean base pressures associated with all groove modifications are significantly higher than the baseline data. In addition, the groove angle effect and the groove depth effect previously examined are verified (figure 4.8).

Additional test modifications included wishbone and doublet vortex generators (h_w = 2.8 mm) with the same lateral spacing as utilized previously (2.5 cm). However, the smaller of these devices were not very effective, although the smaller doublets were more effective than the wishbones of the same device height (figure 4.8). These new data also indicate that the wishbones (h_w = 6.4 mm) and doublets (h_w = 3.8 mm) increased the base pressure of the 2-D blunt trailing-edge airfoil model significantly over the mean baseline level (maximum increase of approximately 50% with wishbones for h_w = 6.4 mm).

Base pressure profiles are presented in figure 4.10 for the 2-D wake model with base cavity and serration modifications. The 2.5 cm long triangular serrations (2.5 cm spacing) had a more significant effect on base pressure than the 1.3 cm long (1.3 cm spacing) serrations. However, the shallow base cavity (1.3 cm depth) had a greater effect on the base pressure than the deeper cavity (2.5 cm depth). Apparently, the larger cavity depth resulted in an attenuation of the effect of the trapped vortex in the cavity, resulting in larger suction pressures. Base pressure distributions for the most effective vortex generator, V-groove, and base cavity modifications tested are presented in figure 4.11. The base cavity modification (1.3 cm depth) resulted in almost a 70% increase in the base pressure over the baseline values, compared to a 50% increase with the wishbone and V-groove modifications. In addition, the pressure distributions with the wishbone and base cavity modifications are uniform.

4.1.2 Shedding Frequency

Measurements of vortex shedding frequency (f) were performed for the unswept model with various V-shape and rectangular groove geometries. Tests were conducted with α values of 30° (d = 6.4 mm and 7.9 mm), 40° (d = 6.4 mm), and 50° (d = 6.4 mm, spacing between groove centerlines of 2.5 cm and

5.1 cm). The shedding frequency data obtained for these groove geometries exhibited significant variability attributable to differences in groove geometry. In particular, as groove cross-sectional area was increased (e.g., by increasing α at constant d), f increased beyond the value obtained for the baseline model. This was an expected result since Strouhal number (St) is a constant at a given Re for similar flows. If St ($=fh/U_\infty$) is a constant, then a decrease in the actual (h) or effective value (h*) of the base thickness should result in an increase in f for constant free-stream speed, U_∞. Strouhal numbers based on f, reference velocity, U_∞ (43 m/s), and apparent base thickness (2.54 cm) displayed a similar behavior as a function of groove cross-sectional area. However, St based on the effective base thickness (St*) exhibited different behavior when examined as a function of the ratio of effective base thickness to apparent base thickness. This latter ratio can be defined as the ratio of the actual base area with grooves to the base area without grooves. The effective Strouhal number (St*) is presented in figure 4.12 as a function of effective base thickness ratio. Figure 4.12 indicates that values of St* are almost equal for four of the seven configurations tested. Values of St* for the other three configurations appear to follow a different trend. Although the 50° V-groove model (2.5 cm spacing) had the same effective base thickness ratio as the rectangular groove model, St* is 10% higher for the former configuration. This result suggests that the mechanism causing the higher values of St* is not simply due to model area changes and resulting changes to the local free-stream speed (reference free-stream speed was measured upstream of the grooves). In addition, in one instance, a change in the effective base thickness was achieved by doubling the distance between grooves (α = 50°; 2.5 cm or 5.1 cm between groove centerlines). The configuration with the smaller spacing (lower effective base thickness ratio) achieved a 10% higher value of St*. It appears that below some critical value of effective base thickness ratio, St* follows one of the two aforesaid trends. These trends may represent two different shedding modes.

When St* is presented as a function of the mean base pressure coefficient, $\overline{C_{pb}}$, another interesting result is obtained (figure 4.13). [The mean base pressure coefficient is calculated from local C_{pb} data using area weighting where C_{pb} = (p-p_{ref})/(0.5ρ U_{∞}^2).] The effective Strouhal number remains constant at the baseline value until some critical increase in $\overline{C_{pb}}$ (above the baseline value) is achieved; i.e., until the grooves significantly alter the wake flow. This occurs for most configurations (one exception has been previously noted) at lower values of the effective base thickness ratio and results in values of St* higher than the baseline value. Previous research with V-shaped grooves has shown that they generate vortices parallel to the groove axis. Minimally, attached flow has been shown to be present in the grooves in the present research. This would appear to be a mechanism by which fluid of higher momentum is redirected to the base flow region to effect an increase in the base pressure. Configurations with equal effective base thickness ratios but with different groove depths; e.g., V-grooves with greater d than for rectangular grooves, would be expected to affect the wake flow differently. Grooves with larger values of d could deliver high momentum fluid closer to the core of the wake and result in larger increases in $\overline{C_{pb}}$. Also, grooves with equal values of d but different values of α would affect the wake flow differently. A higher volumetric flow rate of high momentum fluid would interact with the wake flow for the grooves with the higher α and would result in larger increases in $\overline{C_{pb}}$.

Effective Strouhal number as a function of effective Reynolds number is presented in figure 4.14 for V-grooves with α = 30°, 40°, and 50° (d = 6.4 mm). The Strouhal number is higher for the larger groove angles and there is a trend of increasing St* with increasing Re*.

4.2 Flat-Plate Airfoil with Swept Trailing Edge

4.2.1 Surface and Base Pressure

The streamwise surface pressure variation for the flat plate airfoil model with a 30° swept base (30° swept-wake model) is shown in figures 4.14 to 4.17 for the baseline, V-groove (α = 50°, d = 6.4 mm), and wishbone (h_w = 6.4 mm) modifications, respectively. As expected from displacement thickness considerations, a favorable pressure gradient generally existed just upstream of the base, just as for the rearward-facing step geometries. In the case of the V-groove modification (figure 4.16), however, there was a short region in which an adverse pressure gradient existed between x/h = –4 and x/h = –2. This adverse pressure gradient was due to the flow expanding in the vicinity of the 5.1 cm long V-grooves. A favorable pressure gradient also existed just upstream of the base of the 45° swept-wake model (figure 4.18).

Results of base pressure measurements involving modifications of the swept base (β = 30°) flat-plate airfoil are plotted in figures 4.19 and 4.20 as a function of non-dimensional distance along the baseline. The base pressure distributions for the doublet, wishbone, and reversed wishbone modifications (figure 4.19) are all significantly greater than the baseline level. All of these modifications appear to have a similar effect on the base flow — altering the spanwise pressure gradient along the base in a similar manner. Beyond midspan of the baseline model, there existed on adverse pressure gradient that was geometry-driven; i.e., flow expanded in the downstream direction due to increased cross-sectional flow area in the test section. However, the level of the baseline adverse pressure gradient was magnified as a result of flow alterations due to these flow control devices. These same trends are duplicated in figure 4.20 for the 30° swept-wake model with V-groove (α = 50°, d = 6.4 mm) and triangular serration (2.5 cm long, 2.5

cm spacing) modifications. The maximum increase in C_{pb} for these modifications to the swept-wake model ($\approx$ 40%) was not as great as for the unswept rearward-facing step tests, 3-D base flow is more difficult to control than 2-D base flow. The triangular fences (5 cm long, 2.5 cm spacing) decreased the base pressure, as shown in figure 4.20. Although the spanwise base flow was interrupted by the streamwise fences, trapped vortices likely existed between the fences and caused an increase in the suction pressure.

Local base pressure coefficient as a function of spanwise position for the 45° swept base flat-plate airfoil is presented in figure 4.21 for the wishbone, V-groove, and triangular fence modifications. Results are qualitatively similar to those obtained for the 30° swept-wake model in terms of an increase in the base pressure and general creation or enhancement of the adverse pressure gradient (especially over $0.4 \leq z/s \leq 0.7$) for the wishbone and V-groove modifications. The maximum base pressure increase over the baseline values for the V-grooves modification was 37% for the 45° swept-wake model (compared to 50% for the unswept model and 40% for the 30° swept-wake model). The increasing difficulty of accomplishing flow control with increasing sweep angle is verified. The fence modification produced results similar to the 30° swept-wake model — an overall decrease in the pressure distribution and an accompanying high degree of variability due to the segmenting of the base region.

4.3 Wake Survey Data

To characterize the growth of the turbulent wakes generated by selected models, wake surveys were performed as described previously. Wake total pressure surveys are shown in figures 4.22 and 4.23 at $x/h = 3$ and 8, respectively, for the 2-D wake model with deep rectangular grooves.

Shown in figure 4.22 at x/h = 3 is the thinner wake of the 2-D airfoil model with rectangular grooves, as compared to the wake of the baseline model. However, the wake of the grooved model had a greater velocity defect than the baseline model. At x/h = 8, (figure 4.23), the wakes of the two models displayed similar velocity defect profiles, and the wake of the model with rectangular grooves was still thinner. This latter result likely translates into lower total drag for the 2-D wake model with rectangular grooves.

Wake velocity defect data are presented for the baseline 30° swept-wake model in figures 4.24 to 4.26 at z/s = 0.25, 0.50, and 0.75, respectively. Shown in each figure are profiles at three streamwise locations downstream of the base of the model, with the last two positions representing measurements made in a plane perpendicular to the streamwise direction. Shown in these figures is the typical decrease in wake velocity defect and increase in wake thickness in the downstream direction. Also notable is the influence of end effects on the profile at z/s = 0.25 and x/h = 2 compared to the profiles at the same longitudinal location at z/s = 0.50 and 0.75. The profile at z/s = 0.25 (x/h = 2) displays a greater-velocity defect than the profiles at z/s = 0.50 and 0.75, which are nearly identical; indicating that the spanwise flow had reached an asymptotic state away from the wall.

Similar wake velocity surveys are exhibited in figures 4.27 through 4.32 for the 30° swept-wake model with V-groove and wishbone modifications. Compared to the baseline data, the velocity profiles associated with the V-groove modification at x/h = 2 were more uniform and did not show significant end effects (figures 4.27 to 4.29). In addition, the wake of the 30° swept-wake model with V-grooves was slightly thinner than the wake of the baseline model with comparable velocity defect at the two upstream x locations and all three locations in z. Wake velocity survey data for the 30° swept-wake model with wishbones (figures 4.30 to 4.32) departed markedly from the baseline profiles, especially at x/h = 2 (all three z locations). In addition to the variation in profile shape at that x-location, there also existed a significant increase in the maximum velocity defect compared to baseline data. Furthermore, the wake data for the wishbone modification indicated a larger wake growth rate at all z-locations, compared to the baseline configuration. These results indicate that although the base pressure is higher for the 30° swept-wake model with wishbones, the overall drag is apparently higher due to device drag.

The effect of longitudinal V-grooves and wishbone vortex generators on other characteristics of turbulent wakes generated by blunt trailing-edge airfoils of varying base sweep angle has also been studied. Plane turbulent wakes generated by models of different shapes are known to approach a unique self-preserving state. A self-preserving state is attained when the mean velocity profile normalized by the appropriate velocity and length scales is independent of streamwise position. A two-dimensional self-preserving turbulent wake in the asymptotic limit of vanishing velocity defect (w) is characterized by constant values of two parameters,

$$W = \left(\frac{\mathrm{w_o}}{U_\infty}\right)\left(\frac{x}{\theta}\right)^{1/2} \quad \text{and} \quad \Delta = \delta(x\theta)^{-\frac{1}{2}} \tag{4.1}$$

where $\mathrm{w_o}$ is the maximum velocity defect and δ is the half-wake thickness measured from the maximum velocity defect to where w = $\mathrm{w_o}/2$ in the transverse direction (see figure 4.33) [44]. Momentum thickness, θ, is defined by Sreenivasan [44] as

$$\theta = \int_{-\infty}^{\infty} \left(\frac{\mathrm{w}}{\mathrm{w_o}}\right)\left(1 - \frac{\mathrm{w}}{\mathrm{w_o}}\right) dy \tag{4.2}$$

Uniqueness of the asymptotic self-preserving state requires that the parameters W and Δ assume universal values W* (= 1.63 ± 0.02) and Δ^* (= 0.30 ± 0.005), respectively [44]. Additional parameters, I_1 and I_2, estimated from the normalized wake defect profile and defined as

$$I_n = \int_{-\infty}^{+\infty} \left(\frac{\mathrm{w}}{\mathrm{w_o}}\right)^n d\eta, \quad n = 1, 2 \quad \text{and} \quad \eta = \frac{y}{\delta} \tag{4.3}$$

are also pertinent to the analysis [44]. Integral parameters I_1 and I_2 are expected to have constant values independent of streamwise position for self-preserving profiles. Their average measured values were reported to be $I_1 = 2.06 \pm 0.01$ and $I_2 = 1.51 \pm 0.02$ [44]. An attempt was made herein to characterize wake development in this study in terms of the parameters discussed.

Momentum thickness as a function of streamwise position is shown in figures 4.34 to 4.36 for the 30° swept-wake models. In steady flow, wake momentum loss is an indication of the model profile drag. Therefore, at every streamwise position, θ must be conserved. Large streamwise variations in the measured values of θ are partly an indication of the presence of unsteady three-dimensional flow. The 30° swept-base model with V-grooves appears to have generated a more steady pseudo- two-dimensional wake and less drag, as compared to the 30° swept baseline model and the model with wishbone modifications (see figure 4.34 and 4.35), through attenuation of the spanwise flow at the base of the model and a reduction to the initial wake width. The attached groove flow imparted longitudinal momentum to the wake flow locally . This may explain why the use of V-grooves resulted in higher base pressures for blunt trailing-edge airfoils.

Sharma [19], used normalized graphs of θ, as a function of w_o, to examine wake velocity profiles for self-preservation by comparing them to theoretical curves obtained from the definition of momentum thickness and integral parameters (solid line, figure 4.37) and from the asymptotic wake relations (dashed line, figure 4.37). Similar data for the present study are also shown in figure 4.37. There is close agreement between the experimental data and the theoretical curves for all cases tested. A survey of the wake generated by the 30° swept-wake model modified by wishbones placed in the vicinity of the trailing edge resulted in measurements which depart noticeably from the other experimental data. The wishbones apparently introduced highly three-dimensional flow into the wake near the trailing edge of the model. However, the effect of the vortices generated by the wishbones seemed to diminish rapidly in the downstream direction, as evidenced by the collapsing of the data onto the theoretical curves.

Figures 4.38 to 4.40 show a comparison between the asymptotic profile $\left[\frac{w}{w_o} = \exp\left(-\eta^2 \ln 2\right)\right]$ and measured wake velocity-defect profiles at three spanwise positions for x/h = 14. There is good agreement between the asymptotic profile and the measured profiles. The 30° swept-base model modified with wishbones appears to have caused a more rapid relaxation to free-stream velocity at the edge of the wake due to increased cross-stream mixing produced by the longitudinal vortices introduced into the wake. On the other hand, the wake of the grooved model took comparatively longer for relaxation to occur at each spanwise location. In addition, near the upstream corner of the base, the 45° swept-base data deviates significantly from the asymptotic profile due to three-dimensional end effects. However, as figures 4.39 and 4.40 indicate, in this latter case, the asymptotic profile is approached at midspan. The data then deviate again from the asymptotic profile as the downstream corner of the base is approached. In general, the agreement between the asymptotic profile and measured data appears best at midspan.

Sreenivasan [45], in his study of plane turbulent wakes, observed the convergence of wake parameters Δ and W to asymptotic values Δ^* and W*. Following the approach of Sharma [19], Δ as a function of W in the present study for surveys conducted at midspan are calculated and plotted in figure 4.41 against Sreenivasan's [45] curve $(\Delta \mathrm{W} = \Delta^* \mathrm{W}^*)$ and a theoretical curve for two-dimensional asymptotic wakes [46]. All data points with the exception of those taken at x/h = 2, where there is considerable three-dimensionality in the wake, appear to approach the point (W*, Δ^*) asymptotically. The wake of the grooved 30° swept-base airfoil model appears to approach the asymptotic point faster than the other configurations, while the baseline 45° swept-base model and 30° swept-base model with wishbones approach the asymptotic self-preserving state at the slowest rates.

Average values of I_1 and I_2 for the present models and values from Sharma [19] are listed in table 4.1. The data compare reasonably well considering that the present measurements were made within x/h < 20.

By applying the integral conservation of momentum equation

$$F_b + F_s = (d/dt)\int_{cv} \rho V dV + \int_{cs} V \rho V dA \tag{4.4}$$

to a control volume around the model and utilizing the applicable wake survey data, drag of the model per unit width was calculated for the 30° swept-base model modified with wishbones and V-grooves (α = 50°). In table 4.2, these calculations are tabulated for the three spanwise survey positions for each model at the farthest upstream location. Calculation of the drag per unit width with the V-grooves at two spanwise locations show a lower drag compared to the baseline model. On the contrary, the wishbones have a higher calculated drag at two spanwise locations.

Table 4.1 Measured wake parameters, I_1 and I_2.

Model	I_1	I_2
β = 0°, Baseline	2.20±0.09	1.51±0.03
β = 30°, Baseline	2.20±0.10	1.50±0.01
β = 30°, Wishbones	2.04±0.03	1.57±0.11
β = 30°, Grooves	2.26±0.08	1.50±0.01
β = 45°, Baseline	2.22±0.15	1.53±0.12
Reference 19	2.06±0.01	1.51±0.02

Table 4.2 Calculated drag per unit span for the flat-plate airfoil with 30° swept base model and wishbone and V-groove modifications

	Drag/w (N/m)		
	z/s = 0.25 (x/h = 16.2)	z/s = 0.5 (x/h = 13.9)	z/s = 0.75 (x/h = 11.7)
Baseline	93.94	99.27	104.27
Wishbone (h_w = 6.4 mm)	96.08	98.5	107.35
V-Grooves (α = 50°, d = 6.4 mm)	97.24	93.86	92.58

Fig. 4.1 Base pressure distribution for the 2–D wake model with V-grooves of varying depth (α = 30°)

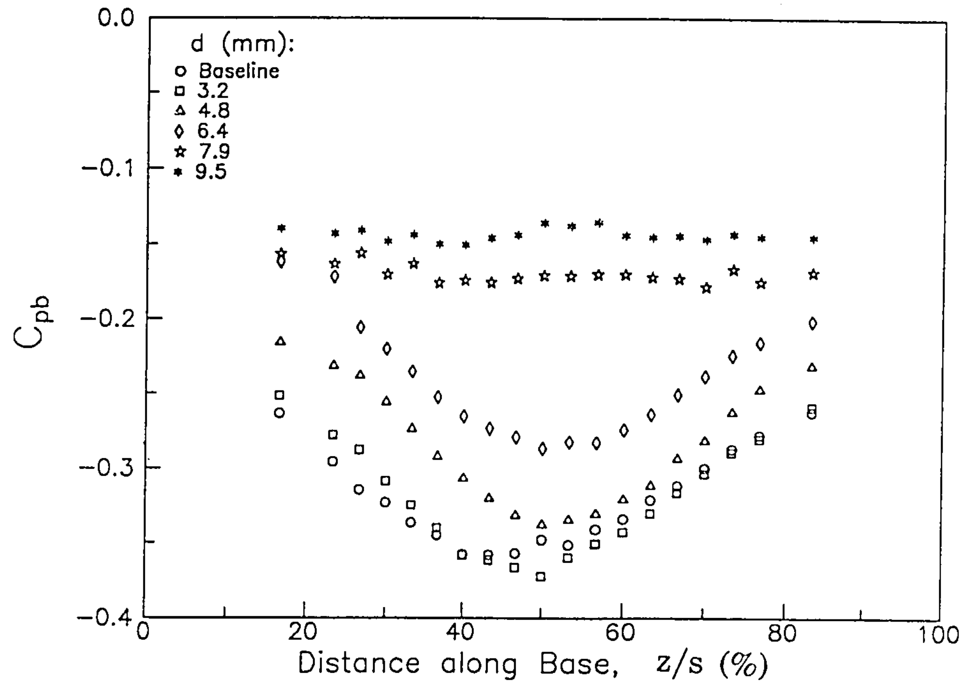

Fig. 4.2 Base pressure distribution for the 2–D wake model with V-grooves of varying angle (d = 6.4 mm)

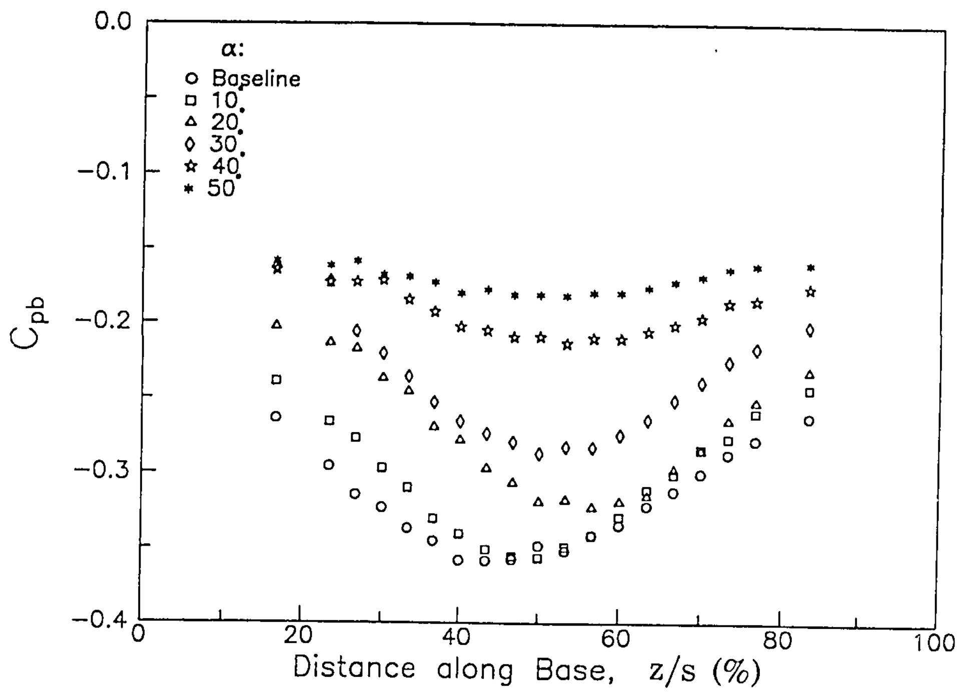

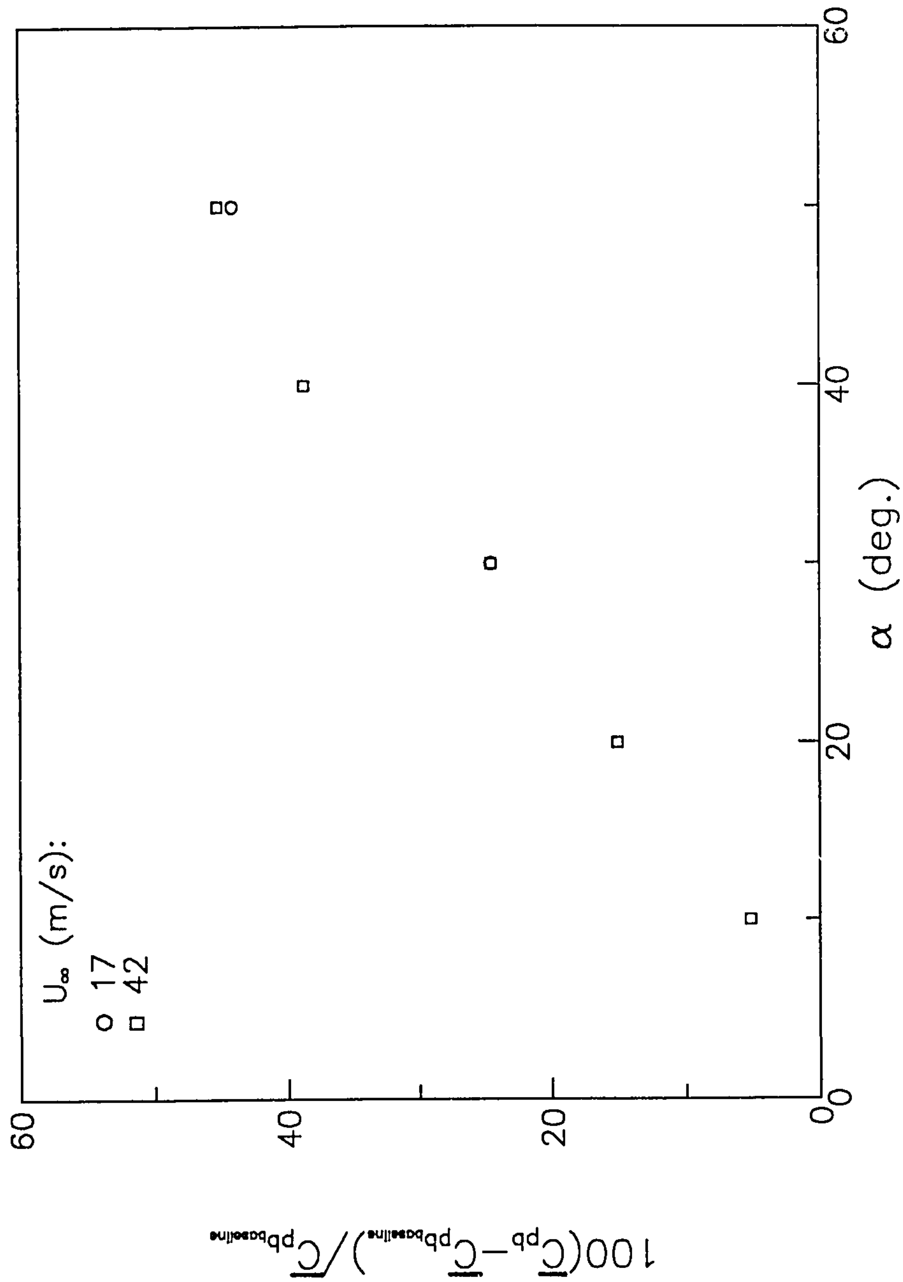

Fig. 4.3 Change in the mean base pressure coefficient for the 2–D wake model with V-grooves of varying angle (d = 6.4 mm)

Fig. 4.4 Base pressure distribution for the 2-D wake model with V-grooves of lengths between 6 and 51 mm (α = 50°, d = 6.4 mm)

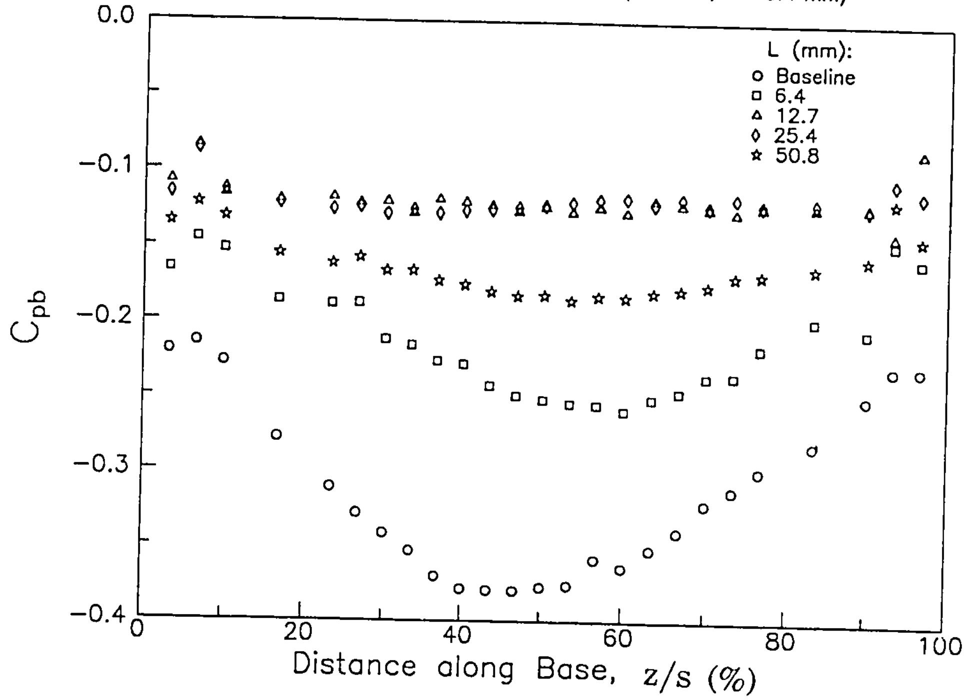

Fig. 4.5 Base pressure distribution for the 2-D wake model with V-grooves of lengths between 5 and 25 cm (α = 50°, d = 6.4 mm)

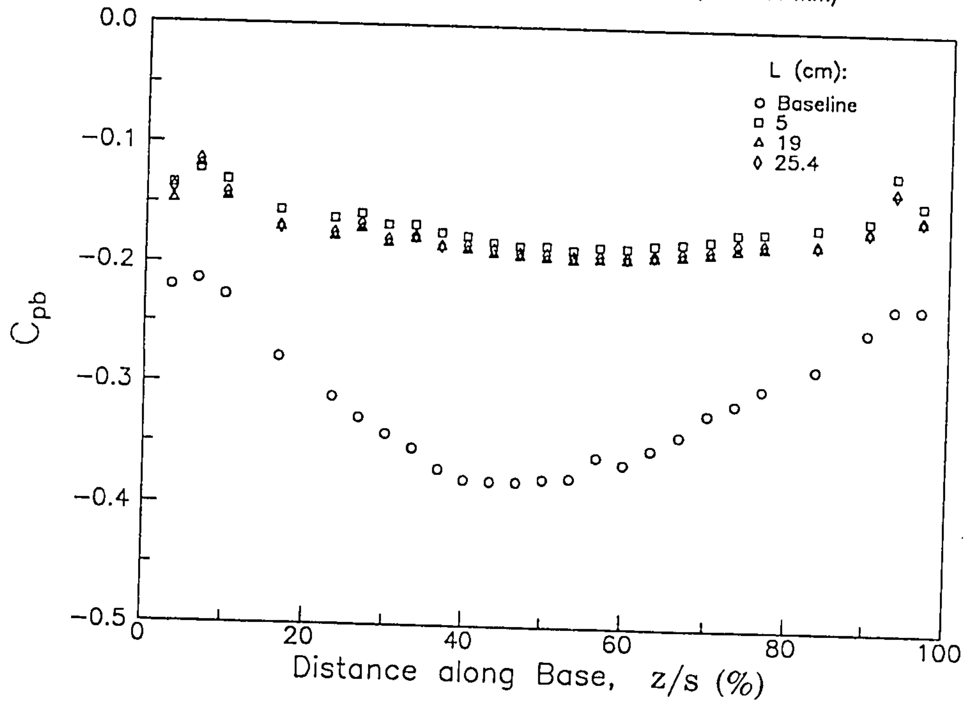

Fig. 4.6 Base pressure distribution for the 2-D wake model with V-grooves of varying length (α = 30°, d = 6.4 mm)

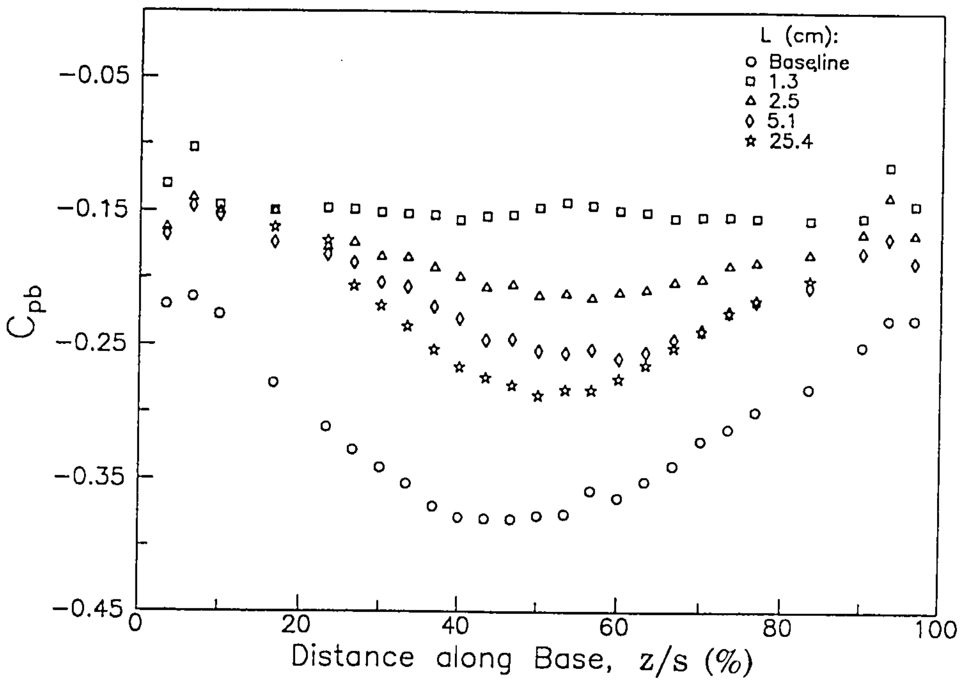

Fig. 4.7 Base pressure distribution for the 2-D wake model with rectangular grooves (7.7 mm×6.4 mm deep) of varying length

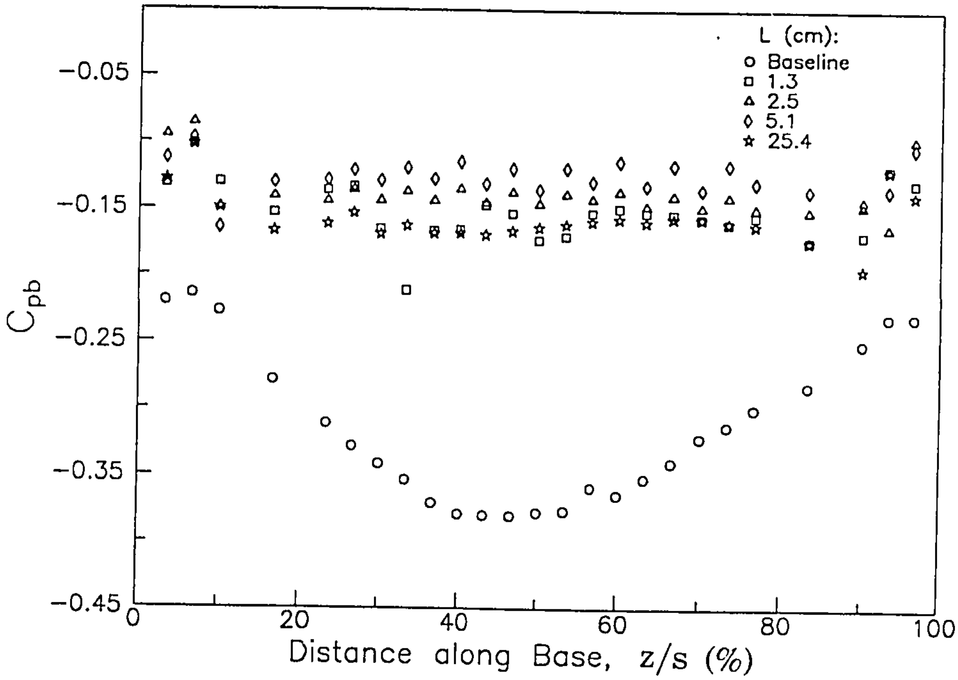

Fig. 4.8 Base pressure distribution for the 2-D wake model with extended sidewalls and various V-groove modifications

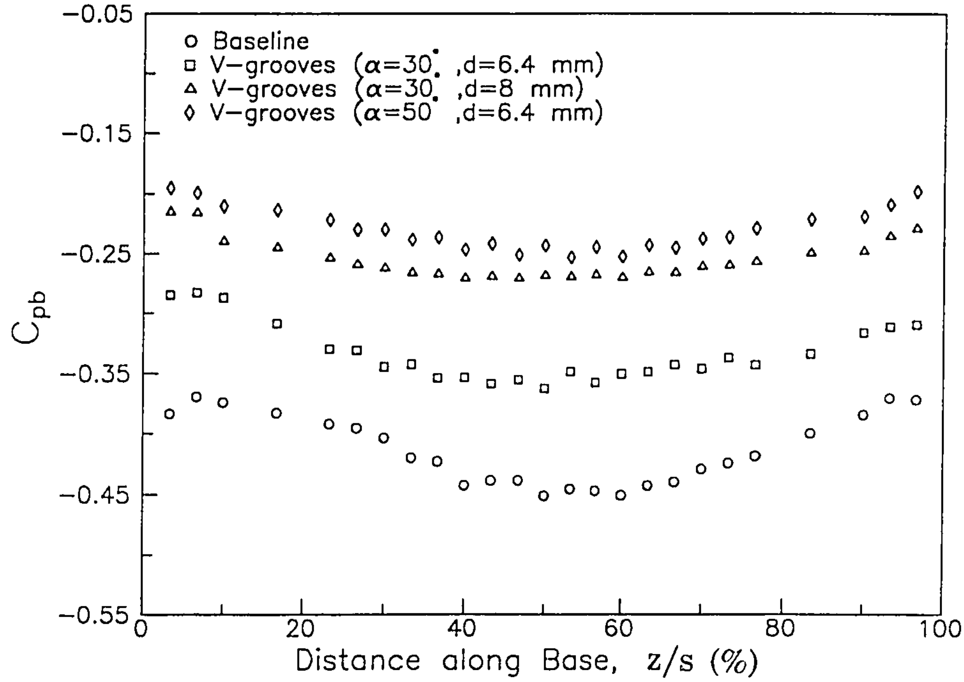

Fig. 4.9 Base pressure distribution for the 2-D wake model (sidewalls extended) with wishbone and doublet vortex generators

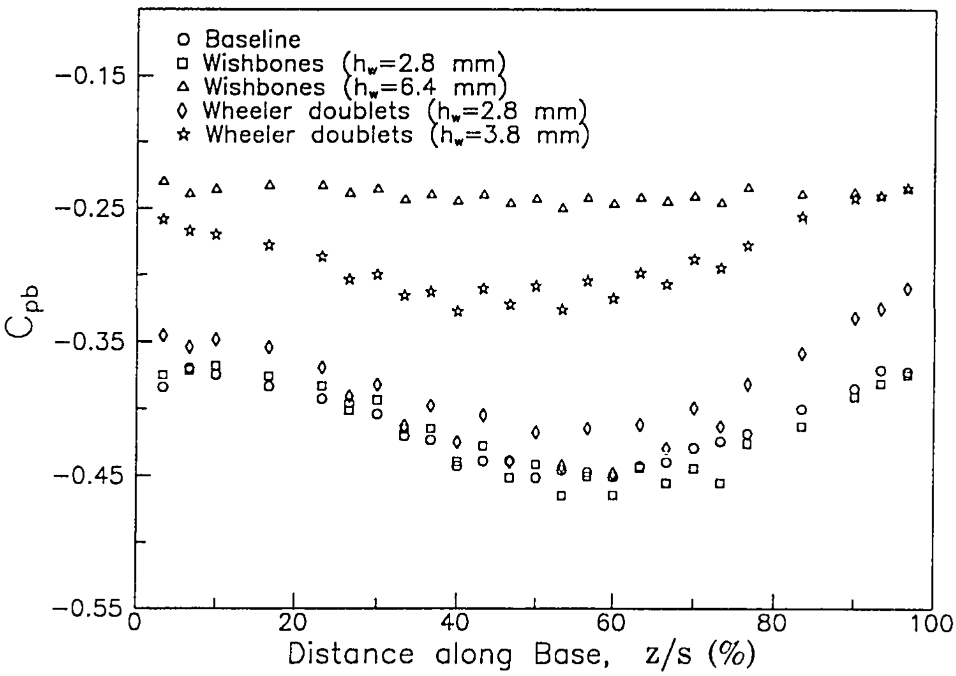

Fig. 4.10 Base pressure distribution for the 2-D wake model with extended sidewalls and base cavity and serration modifications

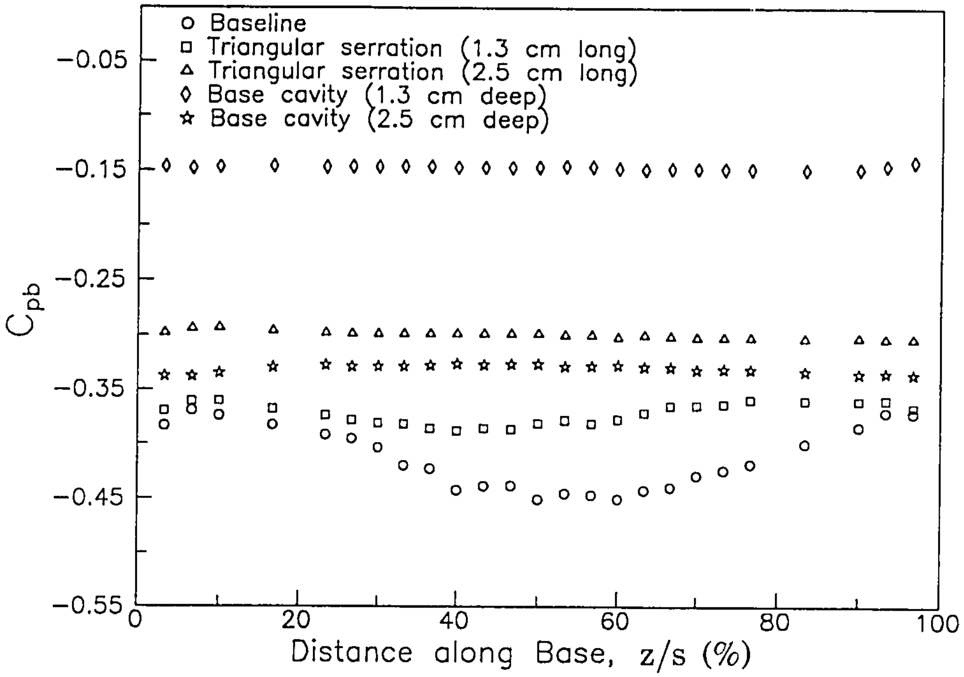

Fig. 4.11 Base pressure distribution for the 2-D wake model (sidewalls extended) with wishbone, V-groove and base cavity modifications

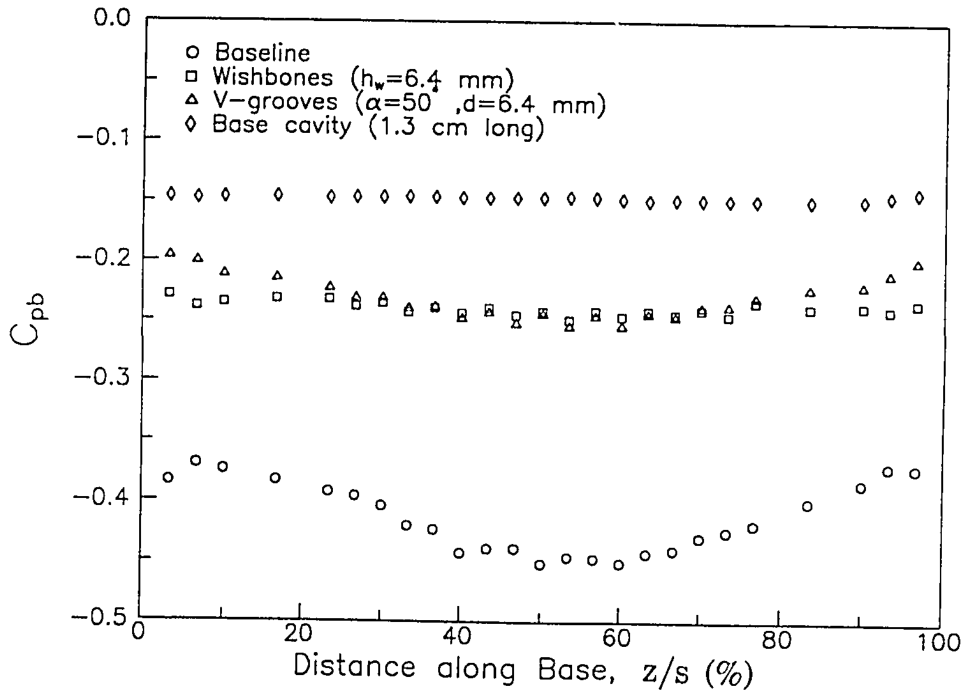

Fig. 4.12 Effective Strouhal number vs. effective base thickness ratio for the 2–D wake model with rectangular and V-shaped grooves

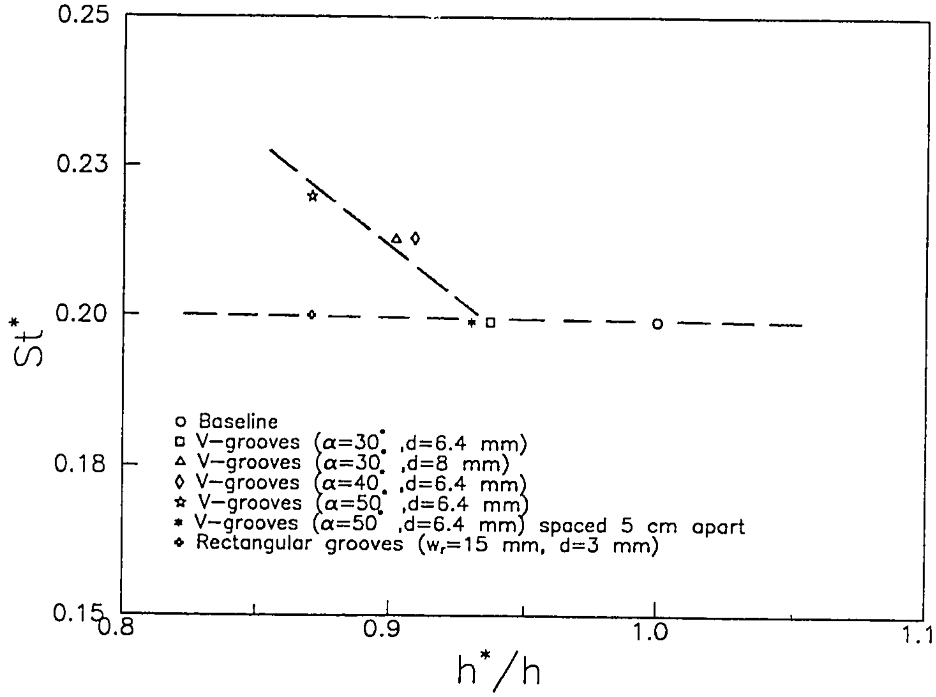

Fig. 4.13 Effective Strouhal number vs. mean base pressure for the 2–D wake model with rectangular and V-shaped grooves

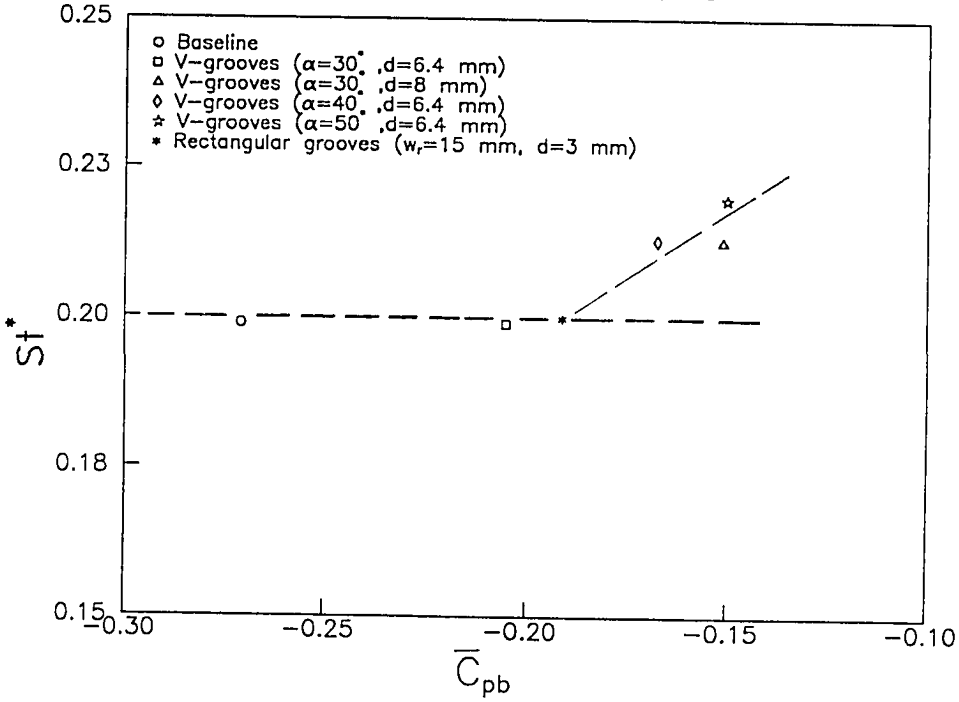

Fig. 4.14 Effective Strouhal number vs. effective Reynolds number for the 2–D wake model with V-grooves

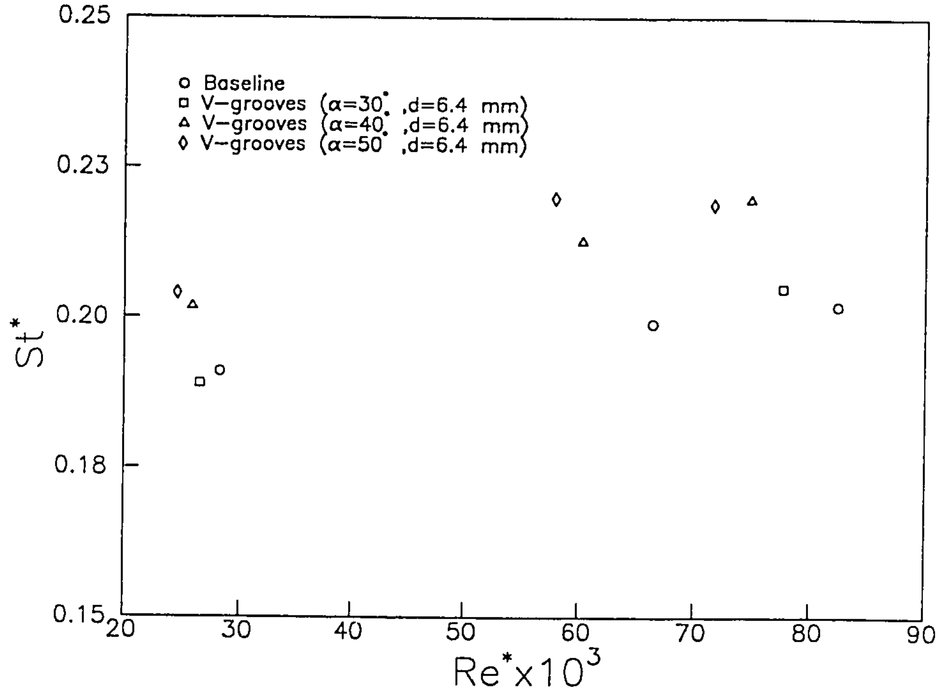

Fig. 4.15 Streamwise surface pressure variation for the 30° swept-base airfoil model

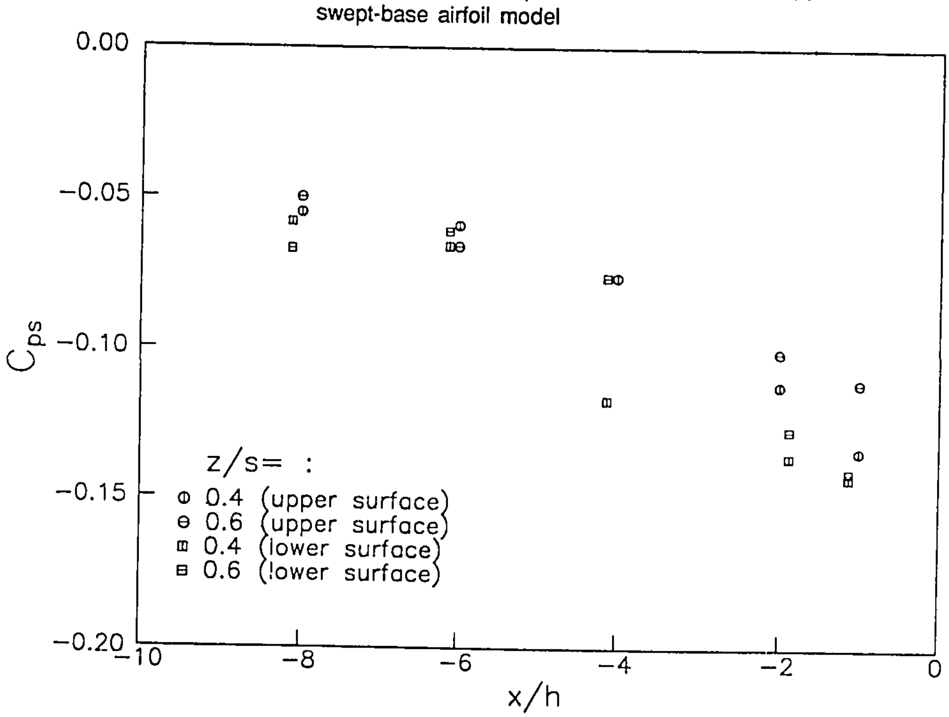

Fig. 4.16 Streamwise surface pressure variation for the 30° swept-base airfoil model with V-grooves (α = 50°, d = 6.4 mm)

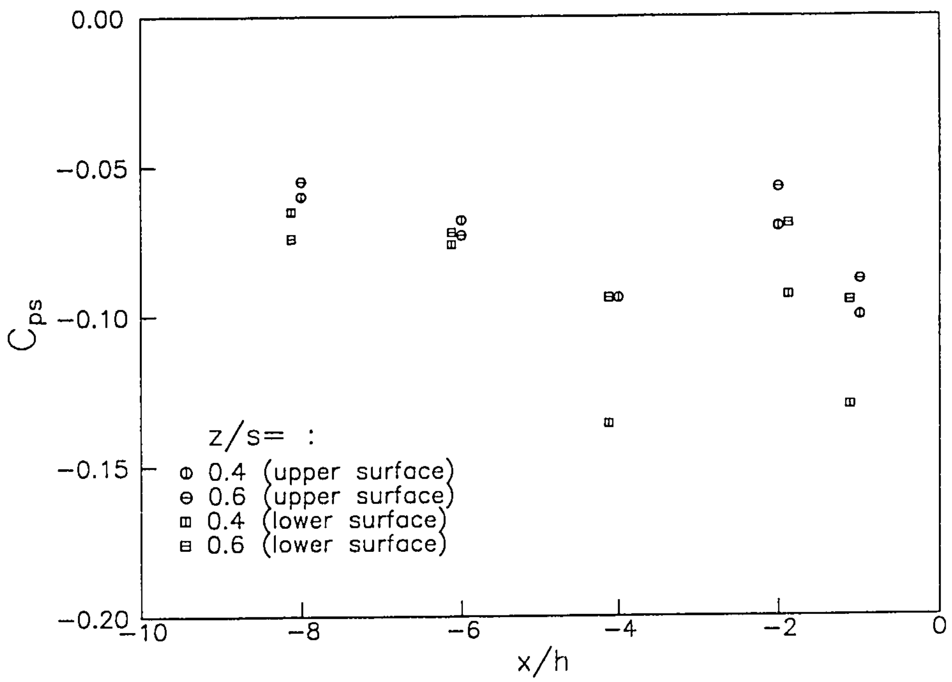

Fig. 4.17 Streamwise surface pressure variation for the 30° swept-base airfoil model with wishbone vortex generators

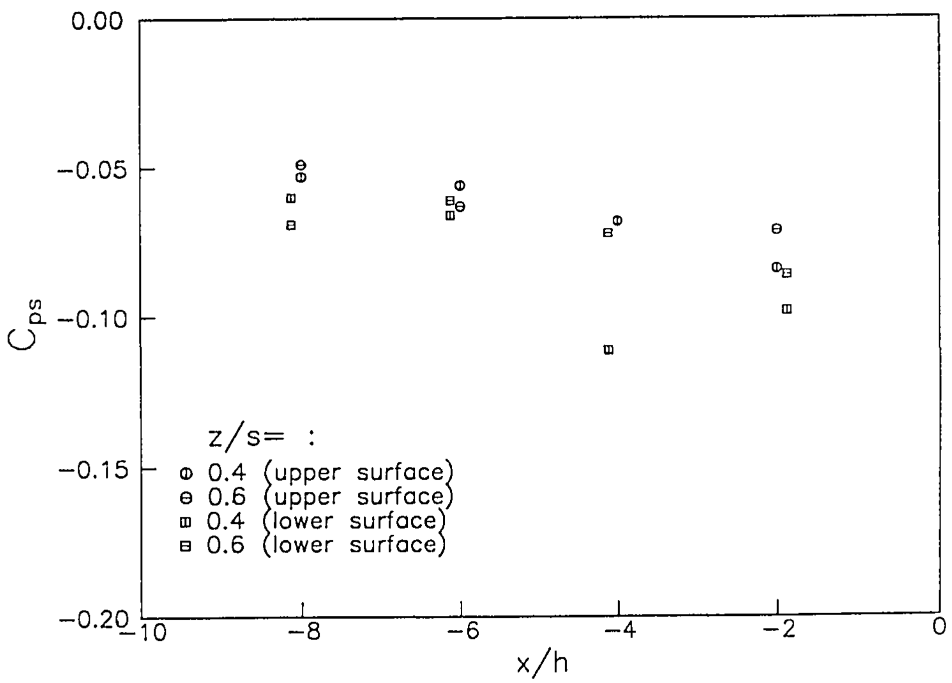

Fig. 4.18 Streamwise surface pressure variation for the 45° swept-base airfoil model

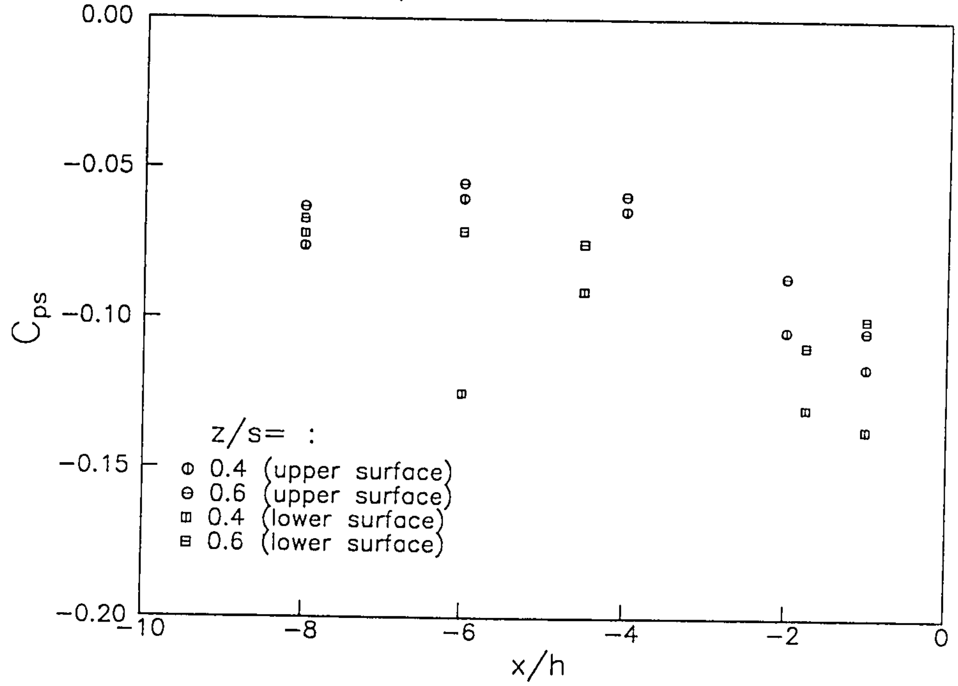

Fig. 4.19 Base pressure distributions for the 30° swept-base airfoil model with wishbone and doublet vortex generators

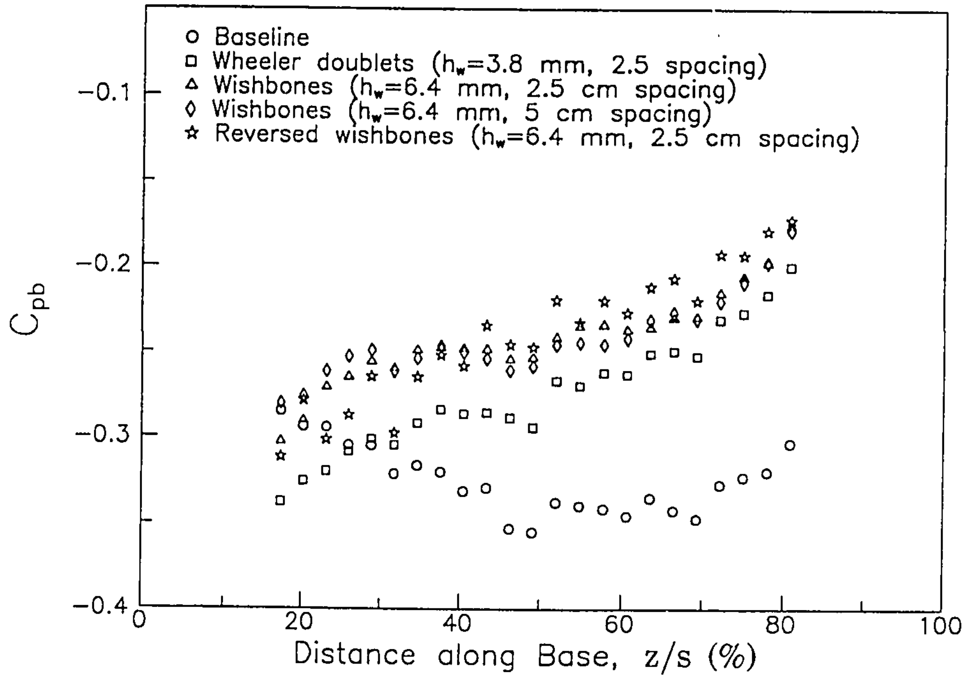

Fig. 4.20 Base pressure distributions for the 30° swept-base airfoil model with triangular serration, V-grooves, and triangular fence modifications

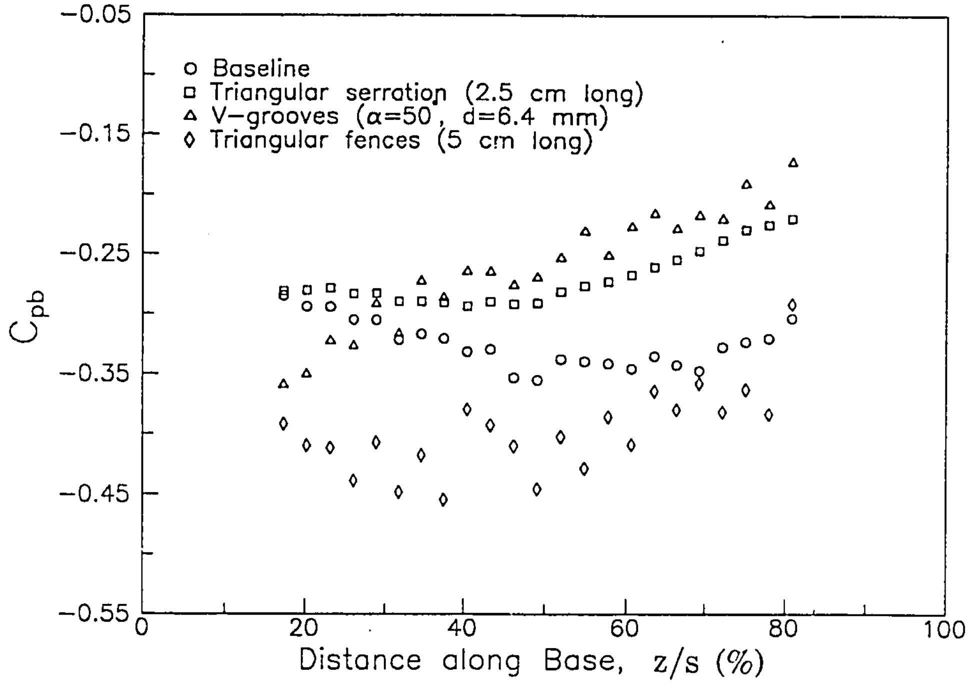

Fig. 4.21 Base pressure distributions for the 45° swept-base airfoil model with wishbone, V-groove, and triangular fence modifications

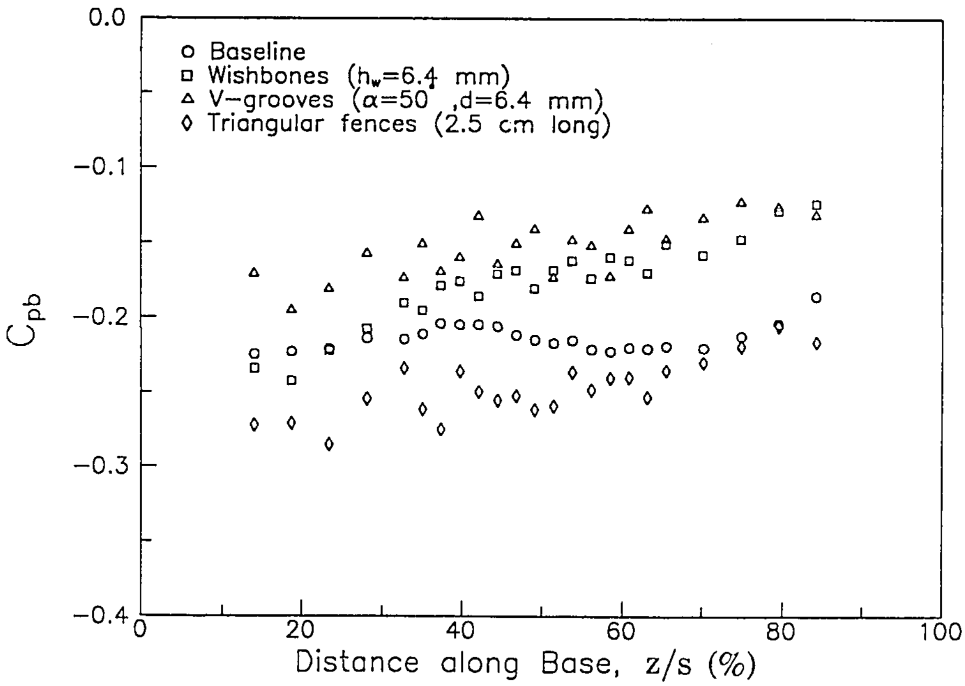

Fig. 4.22 Wake survey at x/h = 3 for the 2-D wake model with rectangular grooves (25.4 cm long)

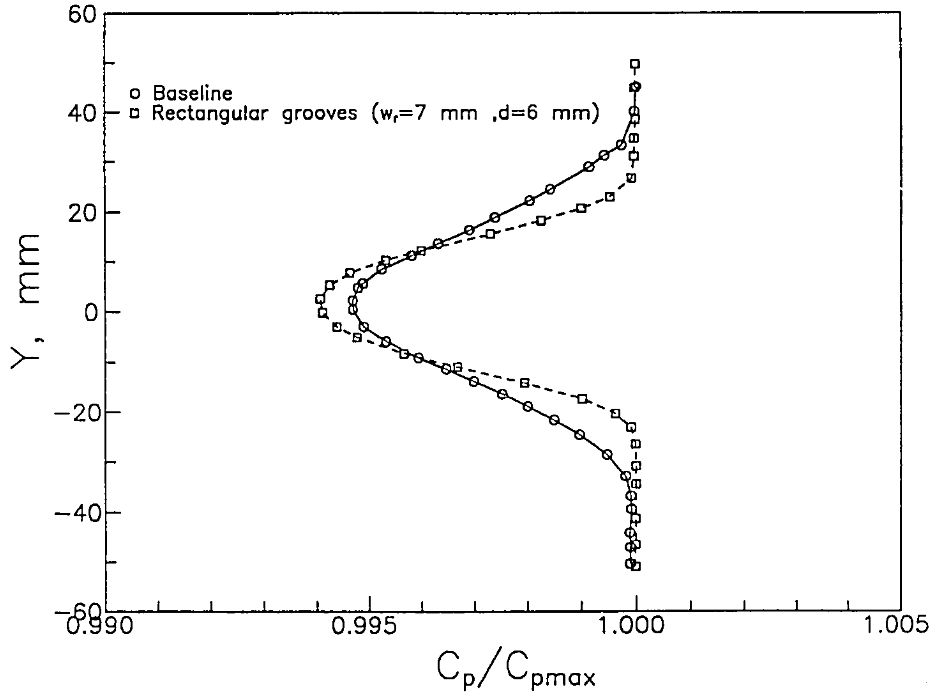

Fig. 4.23 Wake survey at x/h = 8 for the 2-D wake model with rectangular grooves (25.4 cm long)

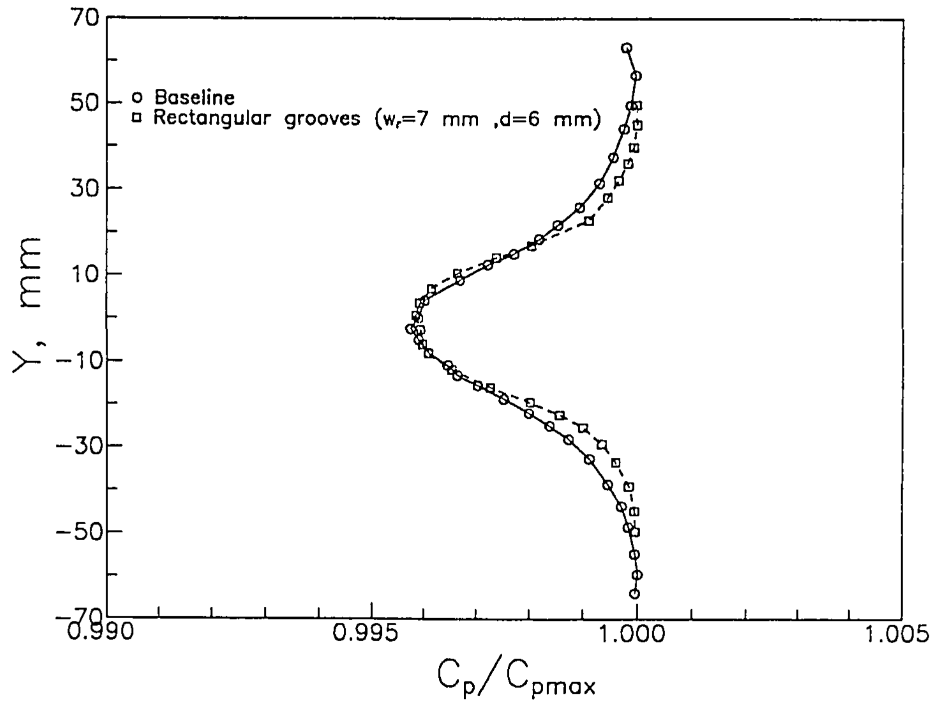

Fig. 4.24 Wake velocity defect profile for the 30° swept-base airfoil model at various streamwise positions (z/s = 0.25)

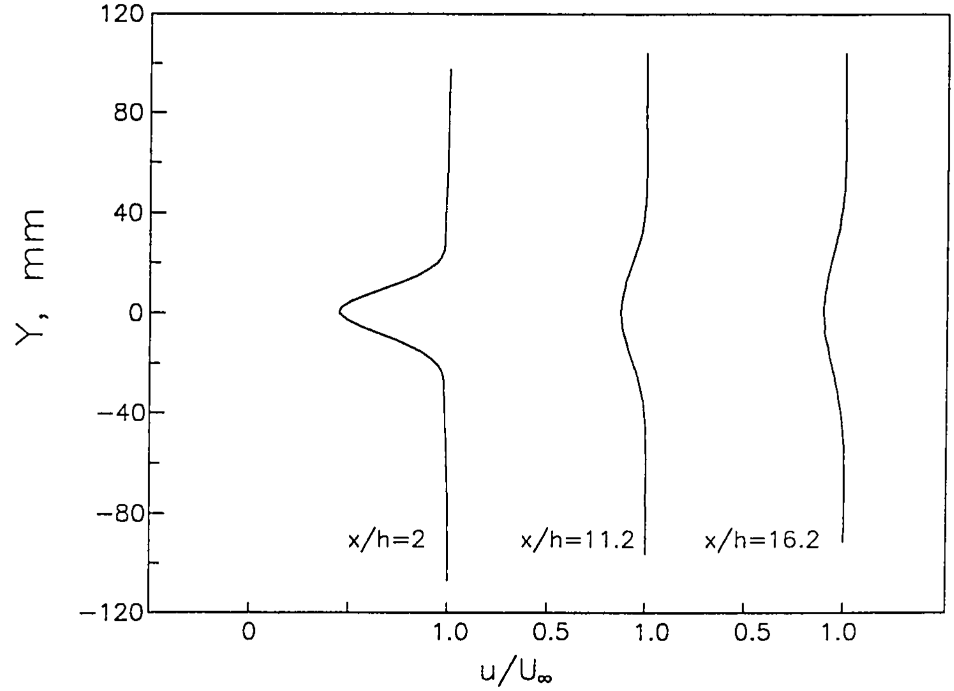

Fig. 4.25 Wake velocity defect profile for the 30° swept-base airfoil model at various streamwise positions (z/s = 0.50)

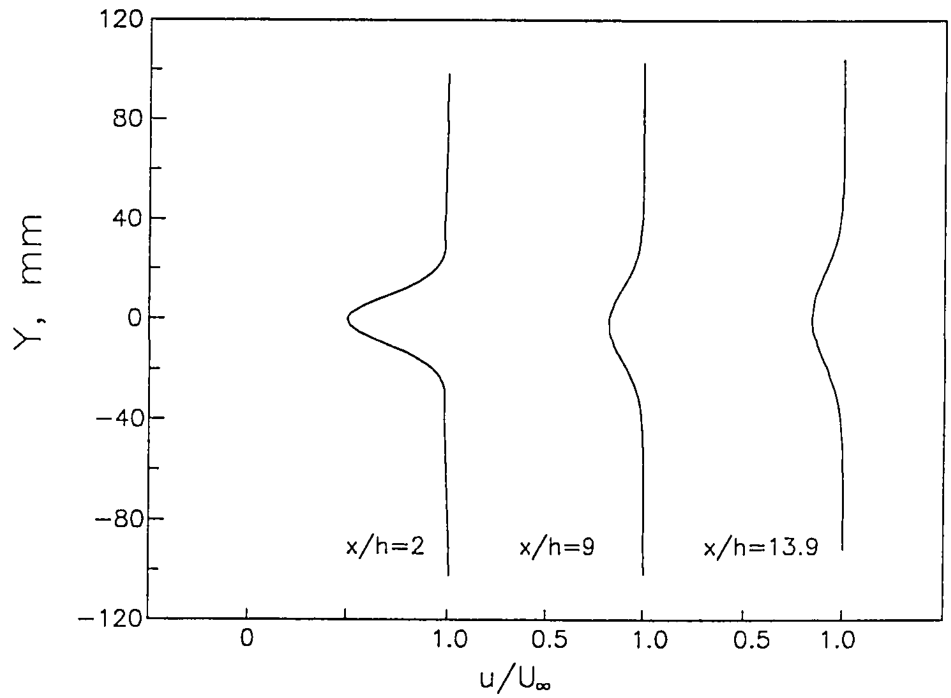

Fig. 4.26 Wake velocity defect profile for the 30° swept-base airfoil model at various streamwise positions (z/s = 0.75)

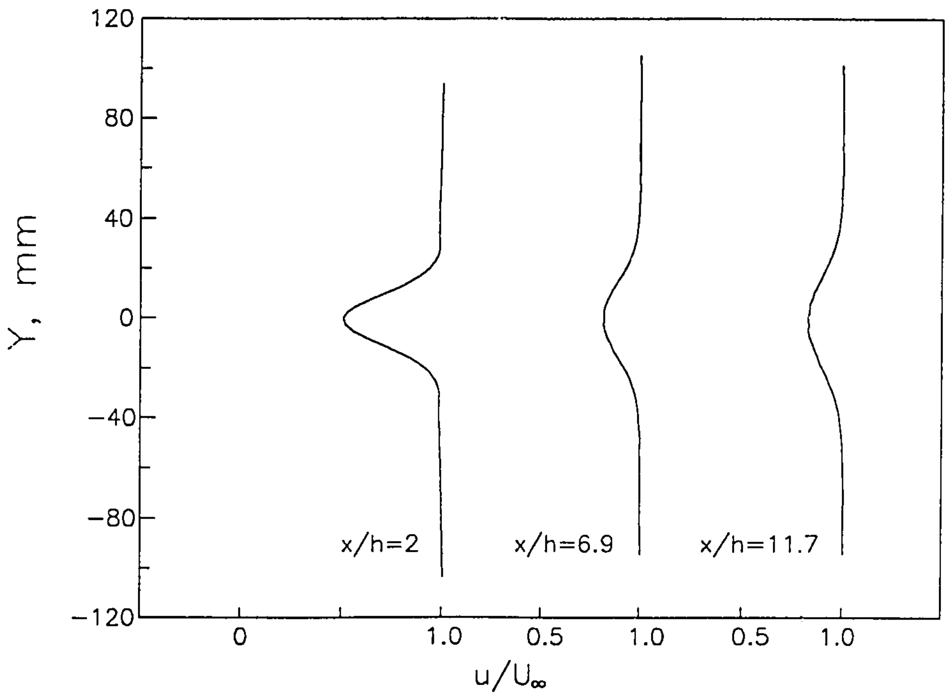

Fig. 4.27 Wake velocity defect profile for the 30° swept-base airfoil model with V-grooves (α = 50°, d = 6.4 mm) at various streamwise positions (z/s = 0.25)

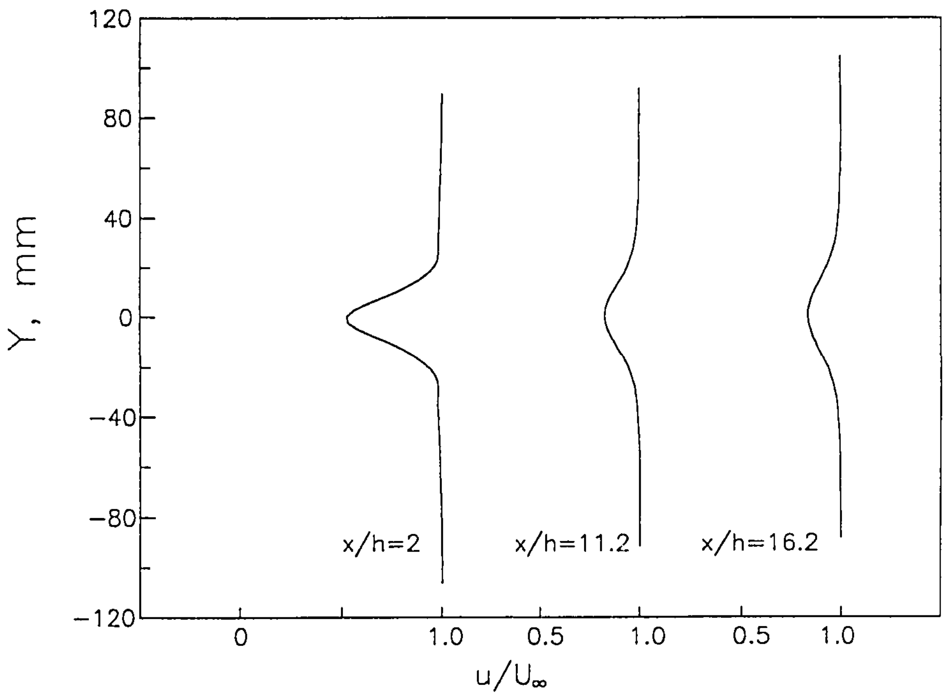

Fig. 4.28 Wake velocity defect profile for the 30° swept-base airfoil model with V-grooves (α = 50°, d = 6.4 mm) at various streamwise positions (z/s = 0.50)

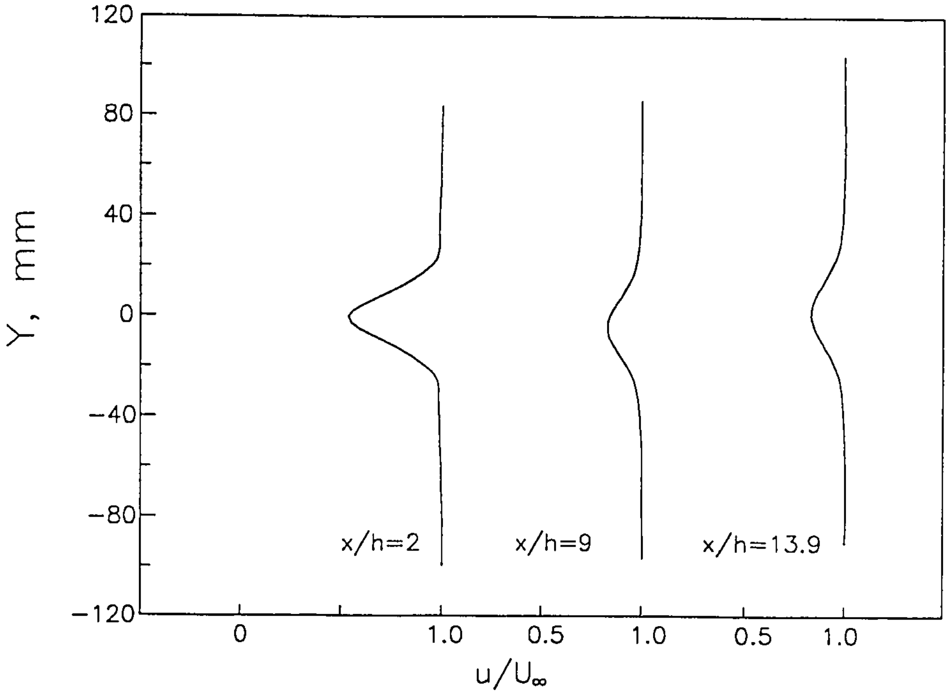

Fig. 4.29 Wake velocity defect profile for the 30° swept-base airfoil model with V-grooves (α = 50°, d = 6.4 mm) at various streamwise positions (z/s = 0.75)

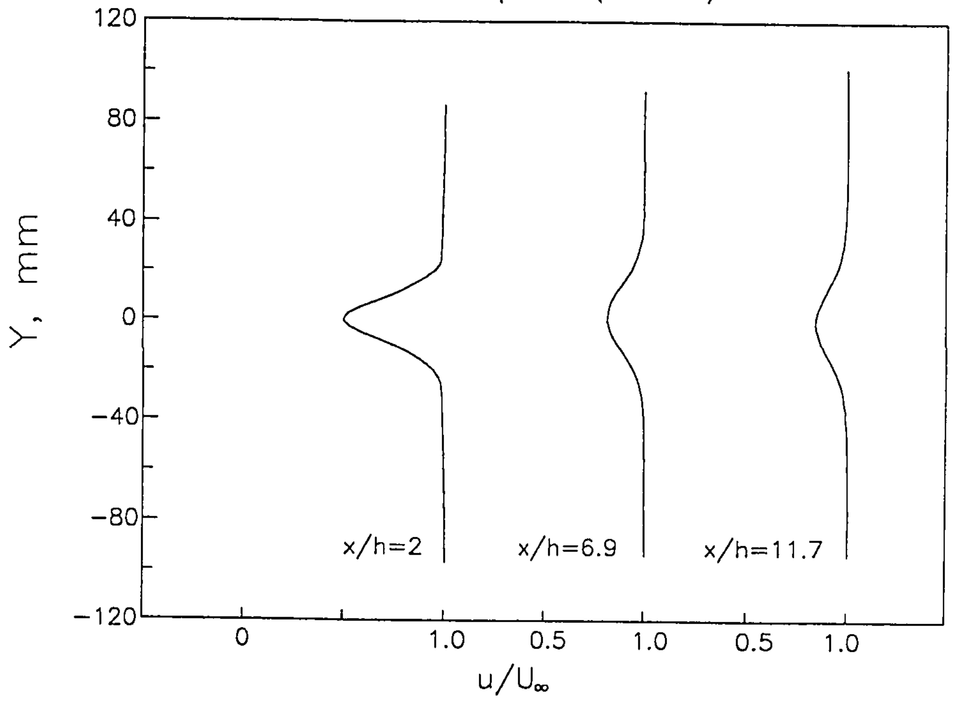

Fig. 4.30 Wake velocity defect profile for the 30° swept-base airfoil model with wishbone vortex generators (h_w = 6.4 mm) at various streamwise positions (z/s = 0.25)

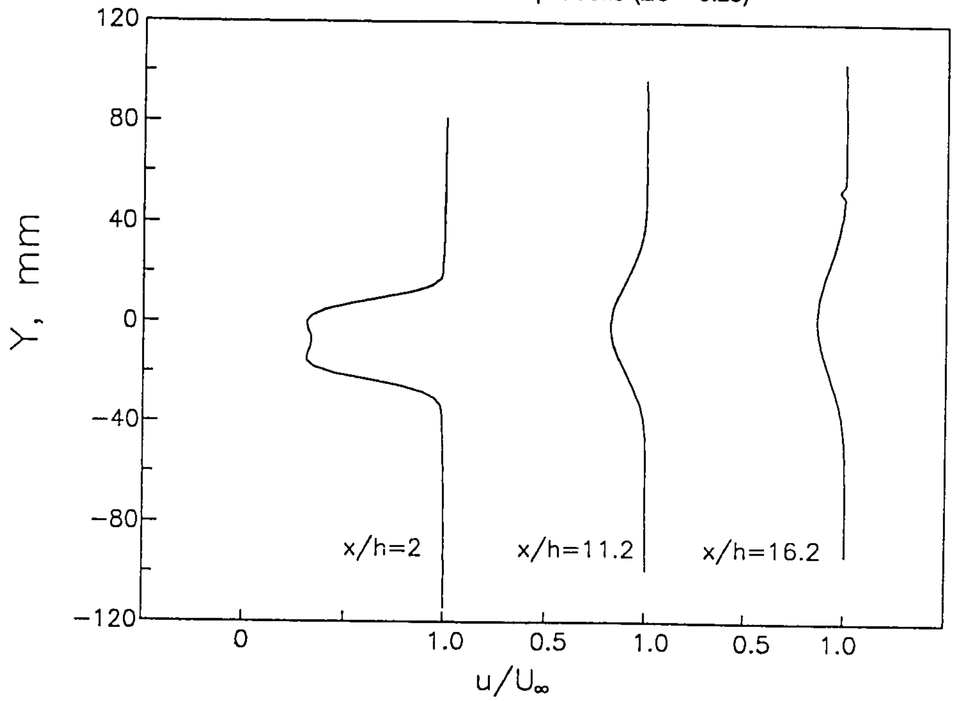

Fig. 4.31 Wake velocity defect profile for the 30° swept-base airfoil model with wishbone vortex generators (h_w = 6.4 mm) at various streamwise positions (z/s = 0.50)

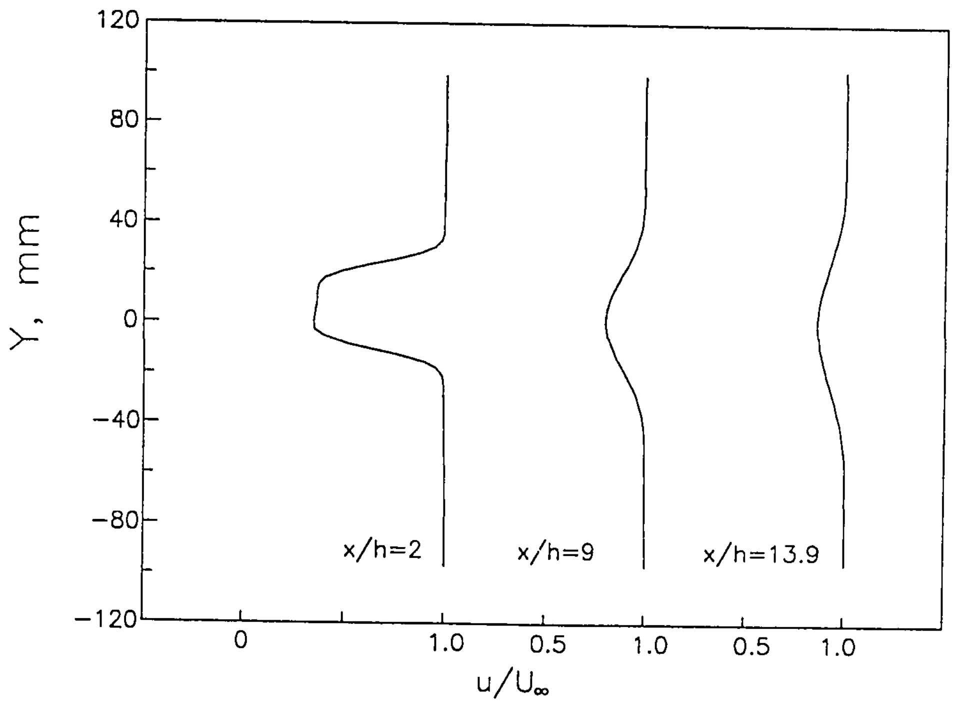

Fig. 4.32 Wake velocity defect profile for the 30° swept-base airfoil model with wishbone vortex generators (h_w = 6.4 mm) at various streamwise positions (z/s = 0.75)

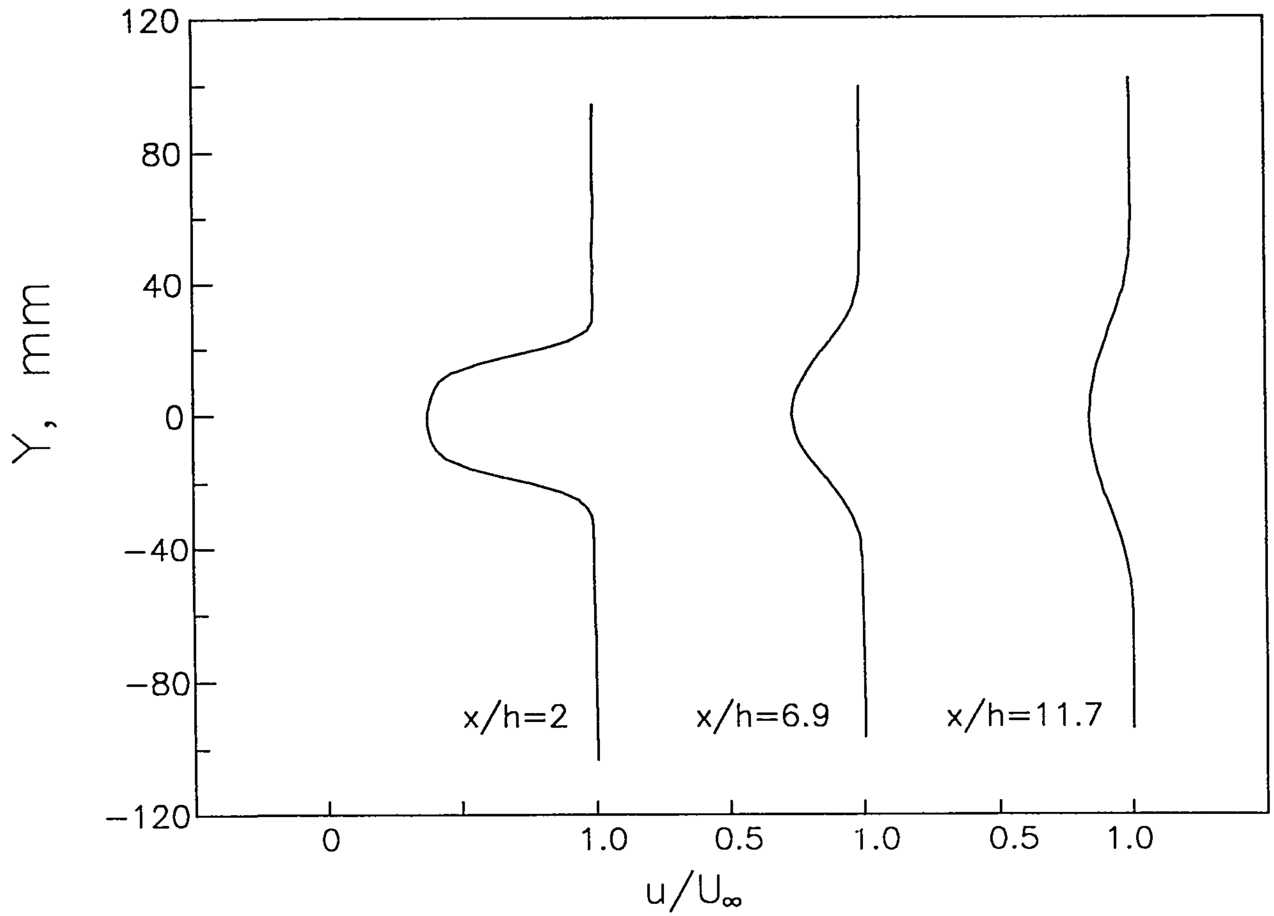

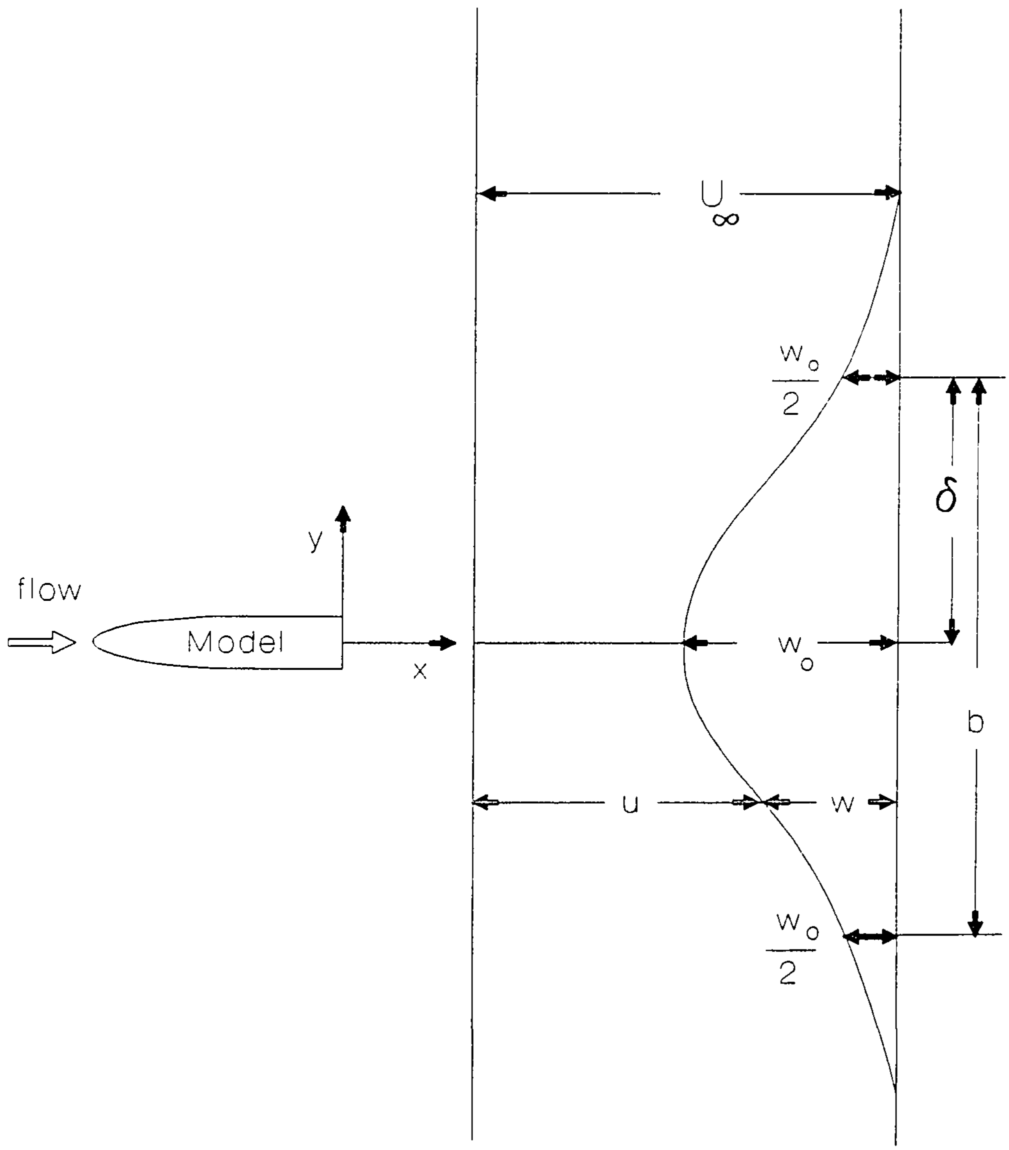

Fig. 4.33 Notation for asymptotic wake calculations

Fig. 4.34 Distribution of wake momentum thickness for 30° swept-base airfoil models (z/s = 0.25)

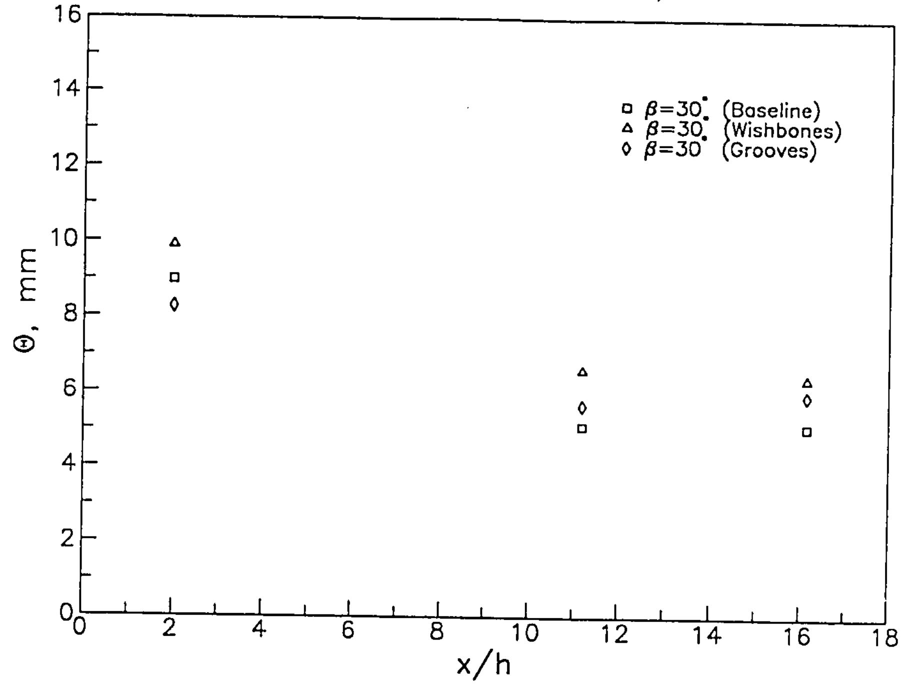

Fig. 4.35 Distribution of wake momentum thickness for 30° swept-base airfoil models (z/s = 0.5)

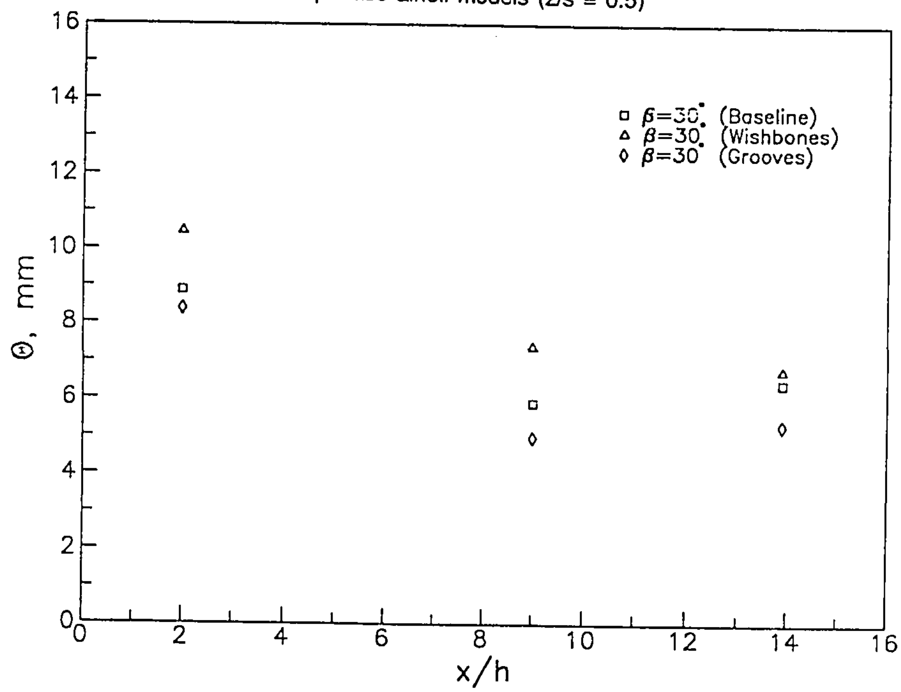

Fig. 4.36 Distribution of wake momentum thickness for 30° swept-base airfoil models (z/s = 0.75)

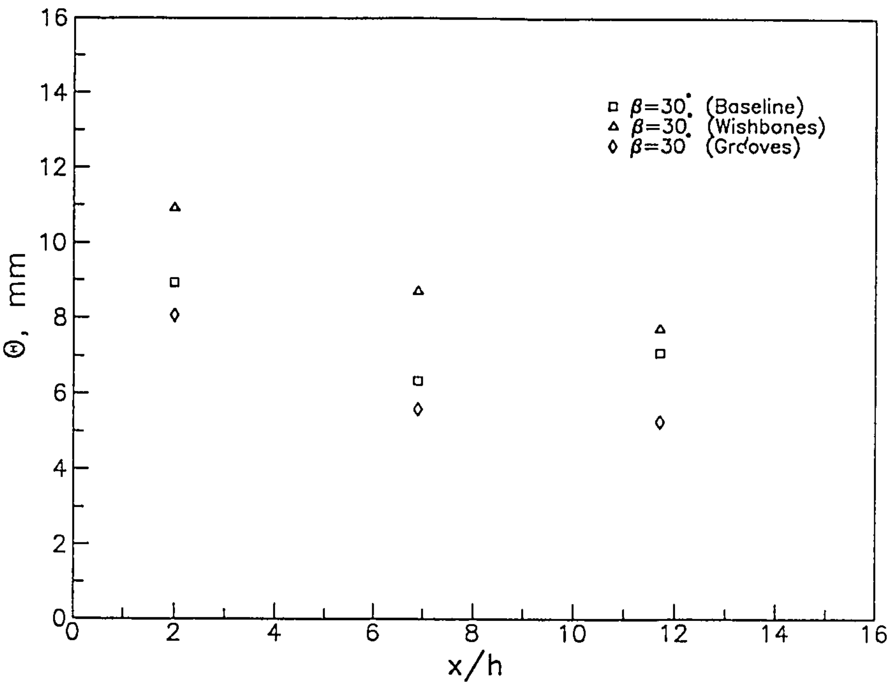

Fig. 4.37 Relationship between defect ratio and wake width for selected unswept and swept-base airfoil models

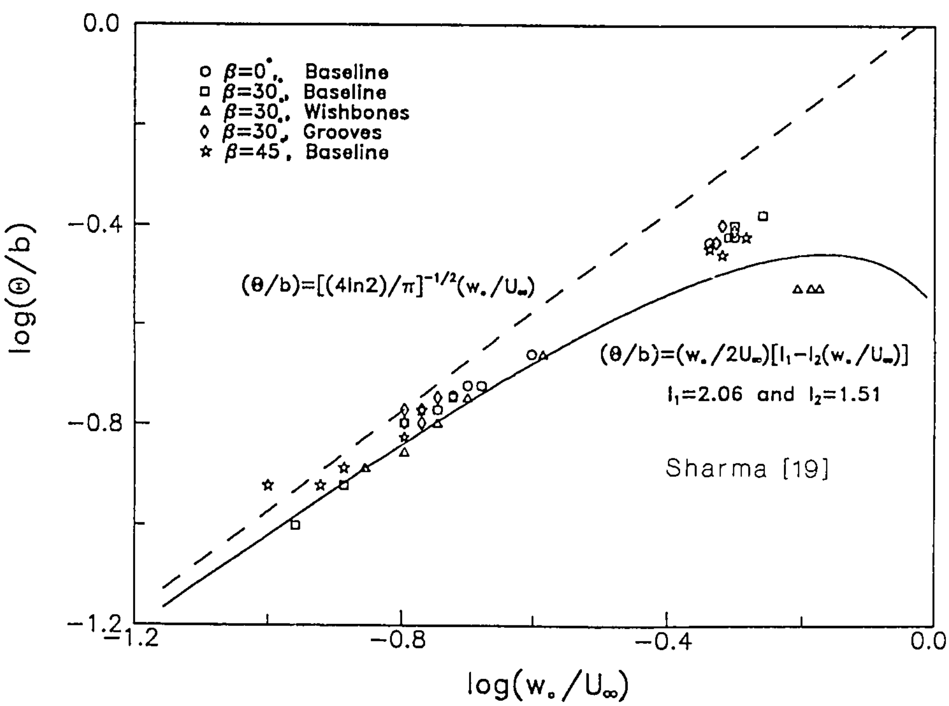

Fig. 4.38 Velocity profiles in the self-similar form at (z/s) = 0.25 and (x/h) = 14 for selected unswept and swept-base airfoil models

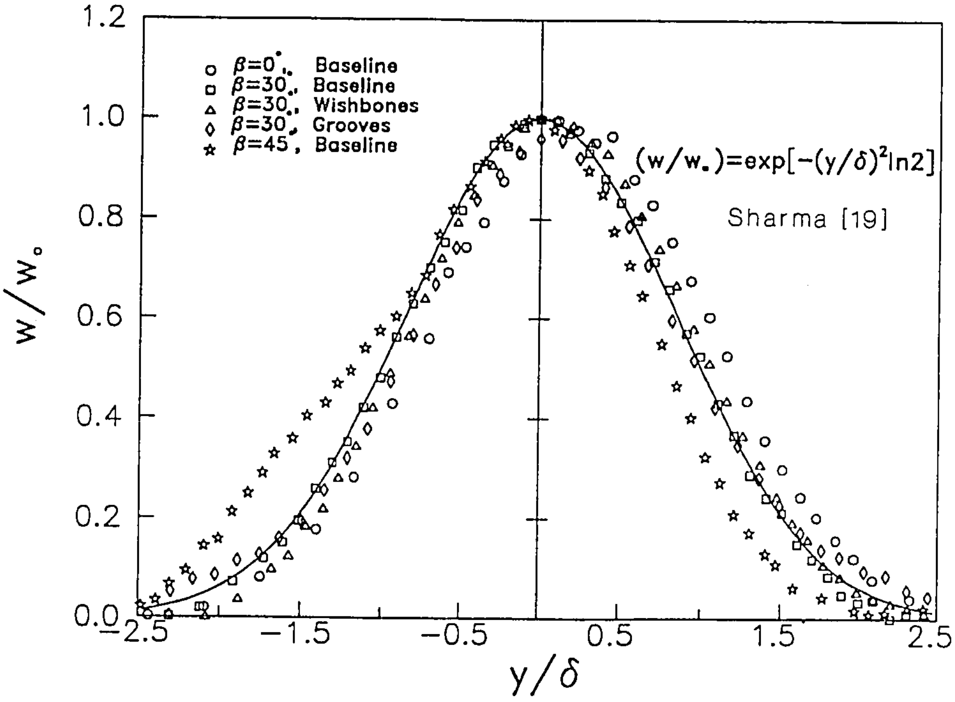

Fig. 4.39 Velocity profiles in the self-similar form at (z/s) = 0.50 and (x/h) = 14 for selected unswept and swept-base airfoil models

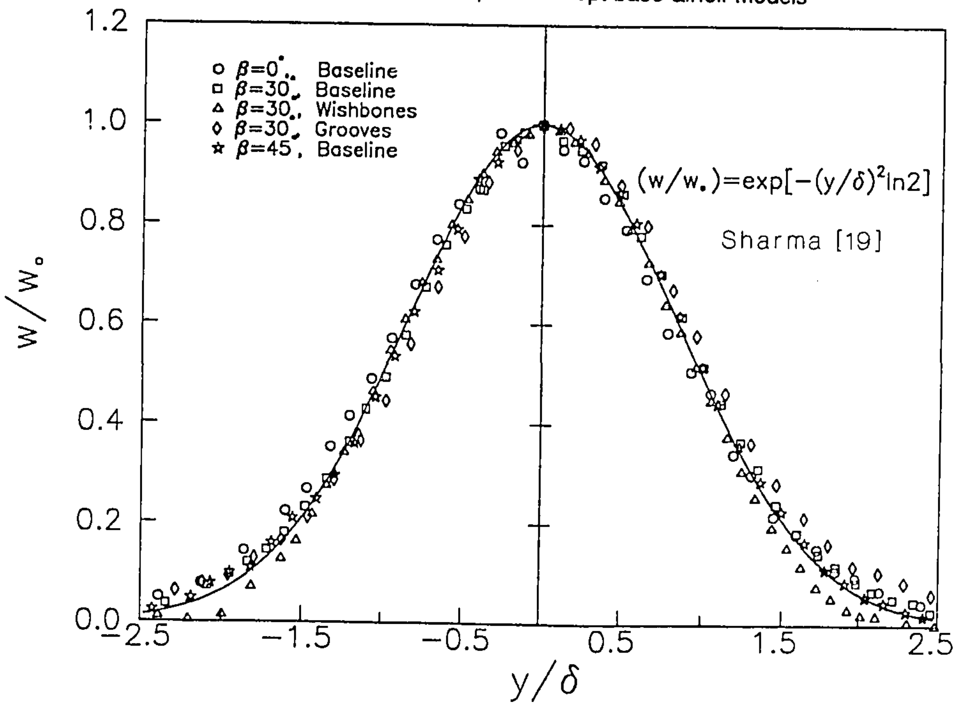

Fig. 4.40 Velocity profiles in the self-similar form at (z/s) = 0.75 and (x/h) = 14 for selected unswept and swept-base airfoil models

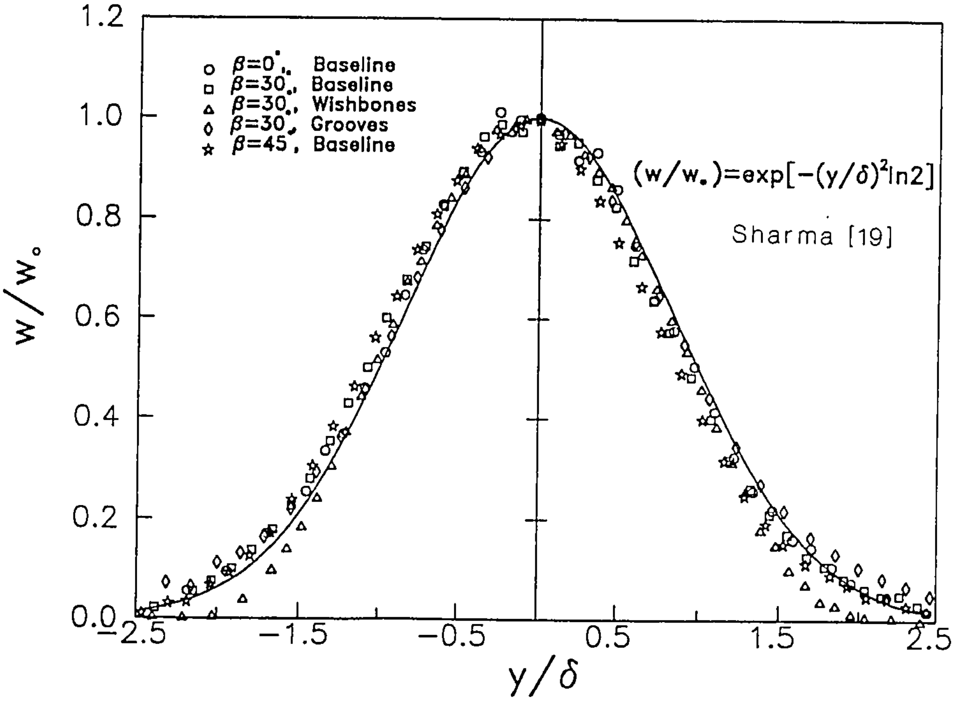

Fig. 4.41 Correlation of wake parameters Δ and W for selected unswept and swept-base airfoil models

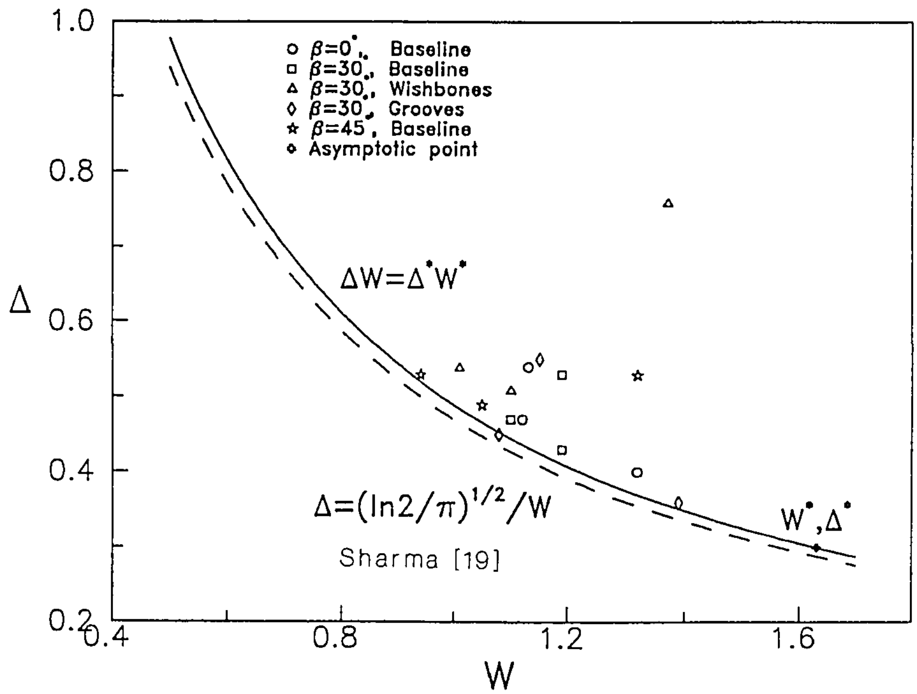

Chapter 5

CONCLUDING REMARKS

Experiments have been conducted on two- and three-dimensional flat plate airfoil and rearward-facing step models to determine the effect of various passive flow-control devices on low-speed turbulent base flow. For the rearward-facing step models, measurements have included surface and base pressure, surface streamline patterns (downstream of the step), and convective heat-transfer rates (from surface downstream of the step). For the flat-plate airfoil models, measurements have included surface and base pressure, vortex shedding frequency, and wake velocity surveys.

The passive flow control devices have included: 1) longitudinal surface V-grooves, 2) rectangular grooves, 3) wishbone vortex generators, 4) doublet vortex generators, 5) triangular base serrations, 6) triangular fences, and 7) base cavities.

Results from the experiments performed on the two-dimensional and swept rearward-facing step models have indicated:

1) Separation regions associated with flow over 2–D and 3–D rearward-facing steps can be significantly decreased using surface grooves and vortex generators, though a device drag penalty is incurred with the solid vortex generators when total drag considerations are relevant;

2) Base serrations and base cavities shifted both the separation and reattachment lines in the downstream direction, but did not significantly change the extent of the separation region;

3) Triangular fences caused the base flow to be segmented into several smaller regions of separated flow and caused an overall reduction to the separation region for the swept-step models;

4) All of the flow-control devices, except the shallow rectangular grooves, resulted in decreasing the base pressure below the baseline values;

5) Surface grooves and solid vortex generators became less effective as the step sweep angle increased, due to increasing strength of the spanwise vortical flow in the separation region with increasing sweep angle; and

6) Convective heat transfer rate from the surface downstream of the 2–D step models has enhanced on the order of 14 to 20% using longitudinal V-grooves.

Based on the experiments performed on the 2–D and 3–D flat-plate airfoil models, it is concluded that:

1) Base pressure was significantly higher than the baseline values with all the flow-control devices with the exception of base fences;

2) Base pressure (with respect to baseline) increased with increasing groove angle (at constant groove depth) and with increasing groove depth (at constant groove angle) for the 2–D models with V-grooves;

3) Deep rectangular grooves were more effective in increasing base pressure than 50 deg. V-grooves and shallow rectangular grooves with the same cross-sectional area;

4) Base-cavity modifications were the most effective in increasing base pressure;

5) Strouhal number was constant (0.2) for most of the grooved models tested, though higher values of St* were obtained with modifications which resulted

in the largest increases to base pressure, indicating that a different shedding mode may have been present for these latter modifications;

6) V-groove modifications to the 30° swept model appears to have produced a lower profile drag than the wishbone modifications;

7) Parameters defined to characterize the wake of the swept airfoil models modified with wishbones and V-grooves were in agreement with those obtained for 2–D wakes sufficiently further downstream of the base. Presence of vortical structures in the wake in the near base region resulted in the deviation of the wake parameter values from those taken further dowstream. This effect was most pronounced in the case of the wishbone vortex generators and less prominant with V-groove modifications.

In general, devices that increased the base pressure for the wake flow model had the effect of decreasing the base pressure for separated flow over rearward-facing steps. The most effective modification to the wake flow model (in terms of increasing the base pressure) was the base cavity. When tested on the rearward-facing step, the base cavity modification resulted in reducing the reattachment distance and decreasing the base pressure. Similar results were observed for V-groove modifications with respect to base pressure, even though they decreased the reattachment distance compared to baseline step. In comparison, all V-groove modifications to the airfoil model resulted in an increase in the base pressure. However, these modifications also increased the Strouhal number (St*).

5.1 Recommendation for Future Studies

Since most of the passive flow control devices examined here would be primarily utilized to improve aerodynamic performance, it is necessary that the effect of such devices be examined on the model lift and total drag. It is in this context that one could really do a comparative evaluation of the performance of each device. Additional devices and techniques should be tested for comparison purposes including vane-type vortex generators and active base bleeding. Passive base bleeding might be considered for the rearward-facing step model. An airfoil model mounted on an aerodynamic balance could be used for this study. Another area for further examination would be the relationship between base pressure and shedding frequency for a blunt body. Present results indicated trends contrary to other studies.

REFERENCES

1. Nash, J. F., "A Discussion of Two-Dimensional Turbulent Base Flows," Aeronautical Research Council R.&M. NO. 3468, 1967.
2. Rudy, D. H., Addy, A. L., "Navier-Stokes Solution of Subsonic Compressible Base Flows," paper presented at the Symposium on Fluid Dynamics, Urbana, Illinois, April 26–27, 1984.
3. Tanner, M., "A Method for Reducing the Base Drag of Wings with Blunt Trailing Edge," *The Aeronautical Quarterly*, Vol. XXIII, Part I, pp. 15–23, Feb. 1972.
4. Poole, R. J. D. and Teeling, P., "Airfoils for Light Transport Aircraft," SAE Transactions, Section 2, Vol. 90, pp. 2040–2046, 1981.
5. Chapman, D. R., "Airfoil Profiles for Minimum Pressure Drag at Supersonic Velocities," NACA TR 1063, 1952.
6. Chapman, D. R., "Reduction of Profile Drag at Supersonic Velocities by the Use of Airfoil Sections Having a Blunt Trailing Edge," NACA TN 3503, 1955.
7. Chapman, D. R. and Kester, R. H., "Effect of Trailing-Edge Thickness on Lift at Supersonic Velocities," NACA TN 3504, June 1955.
8. Holder, D. W., "The Transonic Flow Past Two-Dimensional Aerofoils," J. Royal Aeronautical Society, Vol. 68, No. 644, pp. 501–516, 1964.
9. Nash, J. F., "A Review of Research on Two-Dimensional Base Flow," Aeronautical Research Council R.&M. No. 3323, 1963.
10. Hefner, Jerry N. and Busnnell, D. M., "An Overview of Concepts for Aircraft Drag Reduction," Special Course on Concepts for Drag Reduction, NATO Advisory Group for Aerospace Research and Development, AGRAD Report No. 654, 1977.
11. Roshko, A. O., "On the Drag and Shedding Frequency of Two-Dimensional Bluff Bodies," NACA TN 3169, 1954.

12. Wood, C. J., "The Effect of Base Bleed on a Periodic Wake," J. Royal Aeronautical Society, Vol. 68, pp. 477–482, 1964.

13. Bearman, P. W., "Investigation into the Effect of Base Bleed on the Flow Behind a Two-Dimensional Model with a Blunt Trailing Edge," AGARD CP-4, Part 2, pp. 485–507, 1966.

14. Bearman, P. W., "The Effect of Base Bleed on the Flow Behind a Two-Dimensional Model with a Blunt Trailing Edge," Aeronautical Quarterly, Vol. 18, pp. 207–214, 1967.

15. Motallebi, F. and Norburg, J. F., "The Effect of Base Bleed on Vortex Shedding and Base Pressure in Compressible Flow," J. Fluid Mech., Vol. 110, pp. 273–292, 1981.

16. Nash, J. F., Quincey, V. G. and Callinan, J., "Experiments on Two-Dimensional Base Flow at Subsonic and Transonic Speeds," National Physical Laboratory, Aerodynamics Division, NPL Aero. Report 1070, ARC 25 070, 1963

17. Pollock, N., "Some Effects of Base Geometry on Two-Dimensional Base Drag at Subsonic and Transonic Speeds," Note ARL/Aero. 316, Aeronautical Research Laboratories, Australia, 1969.

18. Gai, S. L., Sharma, S. D., "Experiments on the Reduction of Base Drag of a Blunt Trailing Edge Airfoil in Subsonic Flow," *Aeronautical J.*, pp. 206–210, May 1981.

19. Sharma, S. D., "Development of Pseudo Two-Dimensional Turbulent Wakes," Phys. Fluids, Vol. 30, No. 2, pp. 357–363, Feb. 1987.

20. Sharma, S. D., "Influence of Yaw and Incidence on Base Drag of Rectangular Wings," Z. Flugwiss. Weltraumforsch. 11, pp. 19–22, 1987.

21. Tamura, H., Kiya, M. and Arie, M., "Vortex Shedding from a Two-Dimensional Blunt Railing Edge with Unequal External Freestream Velocities," *Bulletin of JSME*, Vol. 27, No. 231, pp. 1866–1872, Sept. 1984.

22. Boldman, D. R., Brinch, P. F. and Goldstein, M. E., "Vortex Shedding from a Blunt Trailing Edge with Equal and Unequal External Mean Velocities," *J. Fluid Mech.*, Vol. 75, Part 4, pp. 721–735, 1976.

23. Abbot, D. E. and Kline, S. J., "Experimental Investigation of Subsonic Turbulent Flow Over Single and Double Backward Facing Steps," *J. Basic Engineering*, No. 9, pp. 317–325, 1962.

24. Seban, R. A., "Heat Transfer to the Turbulent Separated Flows of Air Downstream of a Step in the Surface of a Plate," Trans. ASME C: J. Heat Transfer, Vol. 86, p. 259, 1964.

25. Goldstein, R. J., Eriksen, V. L., Olson, R. M. and Eckert, E. R. G., "Laminar Separation Reattachement, and Transition of Flow Over a Downstream-Facing Step," Trans. A.S.M.E. D: J. Basic Engineering, Vol. 92, p. 732, 1970.

26. Durst, F. and Whitelaw, J. H., "Aerodynamic Properties of Separated Gas Flows: Existing Measurements Techniques and New Optical Geometry for the Laser-Doppler Anemometer," Prog. Heat and Mass Transfer, Vol. 4, p. 311, 1971.

27. Gosman, A. D. and Pun, W. M., Lecture Notes for Course Entitled: "Calculation of Recirculating Flow," Heat Transfer Rep. HTS/74/2, Imperial College, London, 1974.

28. Kumar, A. and Yajnik, K. S., "Internal Separated Flows at Large Reynolds Number," J. Fluid Mech, Vol. 97, p. 27, 1980.

29. Sinha, S. N., Gupta, A. K. and Oberai, M. M., "Laminar Separating Flow Over Backsteps and Cavities, Part I: Backsteps," AIAA J., Vol. 19, No. 12, pp. 1527–1530, December 1981.

30. Gai, S. L., Sharma, S. D., "Pressure Distributions Behind a Rearward Facing Segmented Step," Experiments in Fluids, 5, pp. 154–158, 1987.

31. Armaly. B. F., Durst F., Pereira, J. C. F. and Schonug, B., "Experimental and Theoretical Investigation of Backward-Facing Step Flow," *J. Fluid Mech.*, Vol. 127, pp. 473–496, 1983.

32. Sparrow, E. M. and Chuck, W., "PC Solutions for Heat Transfer and Fluid Flow Downstream of a Abrupt, Asymmetric Enlargement in a Channel," *Numerical Heat Transfer*, Vol. 12, pp. 19–40, 1987.

33. Aung, W. and Goldstein, R. J., "Heat Transfer in Turbulent Separated Flow Downstream of a Rearward-Facing Step," *Israel J. of Technology*, Vol. 10, No. 1–2, pp. 35–41, 1972.

34. Troutt, T. R., Scheelke, B. and Norman, T. R., "Organized Structures in a Reattaching Separated Flow Field," *J. Fluid Mech.*, Vol. 143, pp. 413–427, 1984.

35. Adams, E. W. and Johnston, J. P., "Flow Structure in the Near-Wall Zone of a Turbulent Separated Flow," *AIAA J.*, Vol. 26, No. 8, pp. 932–939, Aug. 1988.

36. Adams, E. W. and Johnston, J. P., "Effect of the Separating Shear Layer on the Reattachment Flow Structure; Part 2: Reattachment Length and Wall Shear Stress," *Experiments in Fluids*, 6, pp. 493–499, 1988

37. Chang, P. K., "Control of Flow Separation," McGraw-Hill, New York, pp. 251–277, 1976.

38. Lin, J. C., F. G. Howard, and D. M. Busnell, "Investigation of Several Passive and Active Methods for Turbulent Flow Separation Control," AIAA 21st Fluid Dynamics, Plasma Dynamics and Lasers Conference, Seattle, WA, June 18–20, 1990.

39. Howard, F. G, Goodman, W. L. and Walsh, M. J., "Axisymmetric Bluff-Body Drag Reduction Using Circumferential Grooves," paper presented at the AIAA Applied Aerodynamics Conference, Danvers, MA, July 13–15, 1983.

40. Howard, F. G., Quass, B. F., Weinstein, L. M. and Bushnell, D. M., "Longitudinal Afterbody Grooves and Shoulder Radiusing for Low Speed Bluff Body Drag Reduction," ASME Winter Annual Meeting, Washington, D.C., 81–WA/FE-5, November 15–20, 1981,

41. Wheeler, G. O., "Means of Maintaining Attached Flow of a Flow Medium." U. S. Patent No. 4455045, 1984.

42. Wheeler, G. O., Proprietor to Mr. Gary Wheeler, U. S. Patent Pending, 1989.

43. Hewlett-Packard Company, "System 45B Desktop Computer Manual," Waveform Analysis, pp. 11–50, 1979.

44. Sreenivasan, K. R., "Approach to Self-Presentation in Plane Turbulent Wakes," AIAA J., Vol. 19, pp. 1365–1367, 1981.

45. Sreenivasan, K. R. and Narasimha, R.,"Equilibrium Parameters for Two-Dimensional Turbulent Wakes," J. of Fluids Engineering, Vol. 104, pp. 167, June 1982.

46. Patel, V. C. and Scheuerer, G., "Calculation of Two-Dimensional Near and Far Wakes," AIAA J., Vol. 20, No. 7, p. 900, Sept. 1982.

47. Hollman, J. P., "Experimental Methods for Engineers," McGraw-Hill, New York, pp. 41–47, 1989.

APPENDICES

Appendix A

BOUNDARY-LAYER SURVEYS

Fig. A.1 Velocity profiles at 2.5 cm upstream of the step for the 30° swept rearward-facing step model at three spanwise positions (U_∞ = 43 m/s)

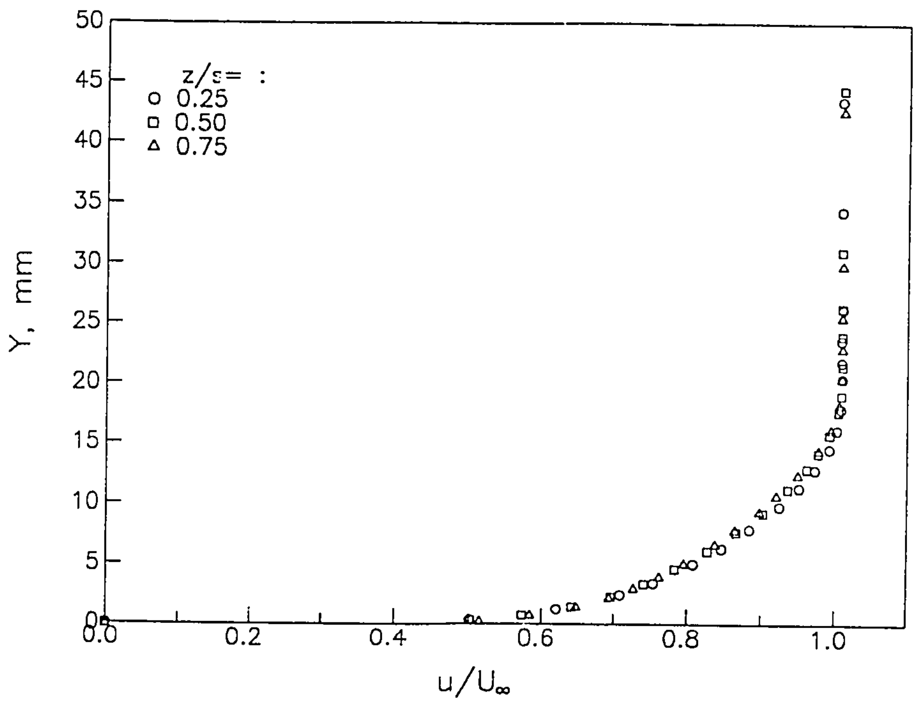

Fig. A.2 Power-law velocity profile at mid-span for the 30° swept rearward-facing step model at 2.5 cm upstream of the step (U_∞ = 43 m/s)

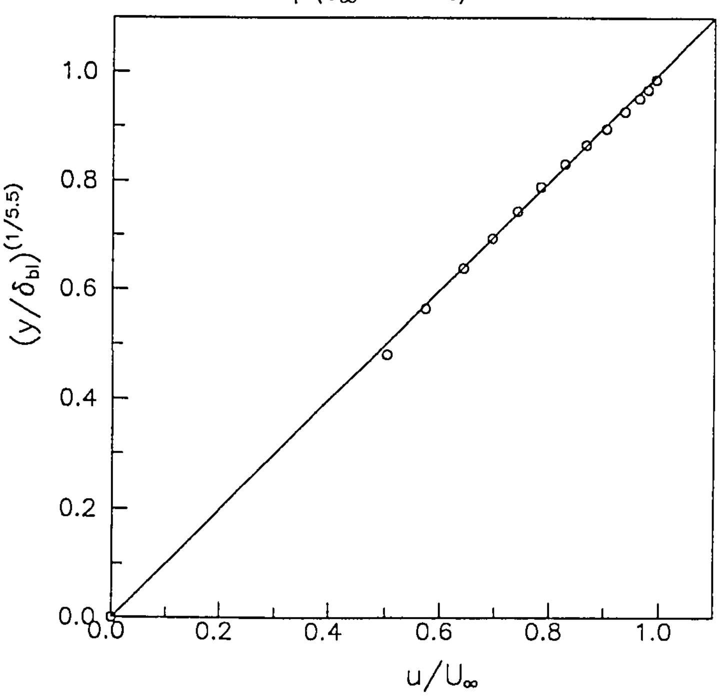

Fig. A.3 Velocity profiles at 2.5 cm upstream of the step for the 45° swept rearward-facing step model at three spanwise positions (U_∞ = 43 m/s)

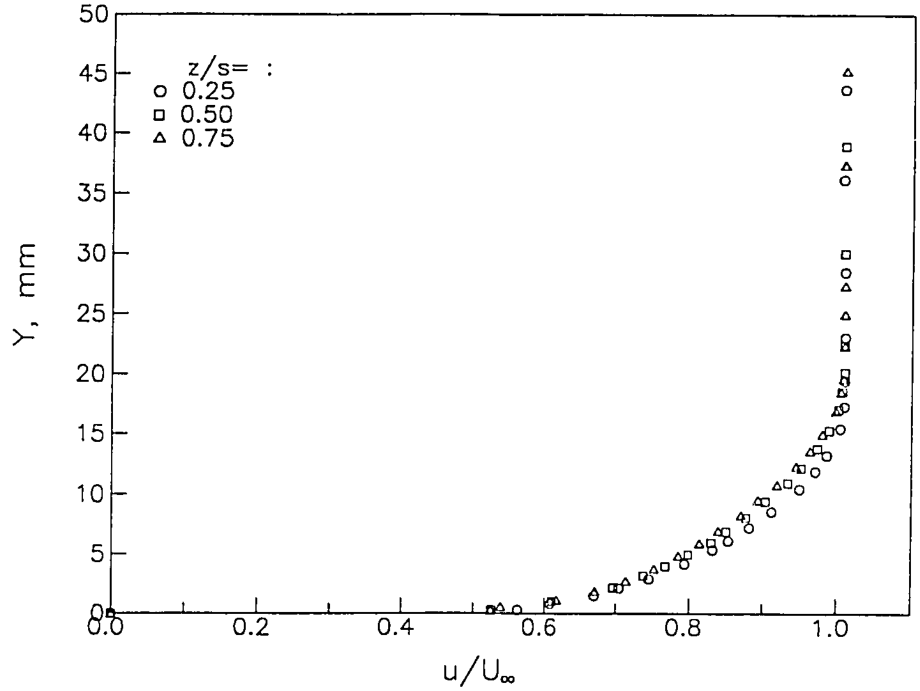

Fig. A.4 Power-law velocity profile at mid-span for the 45° swept rearward-facing step model at 2.5 cm upstream of the step (U_∞ = 43 m/s)

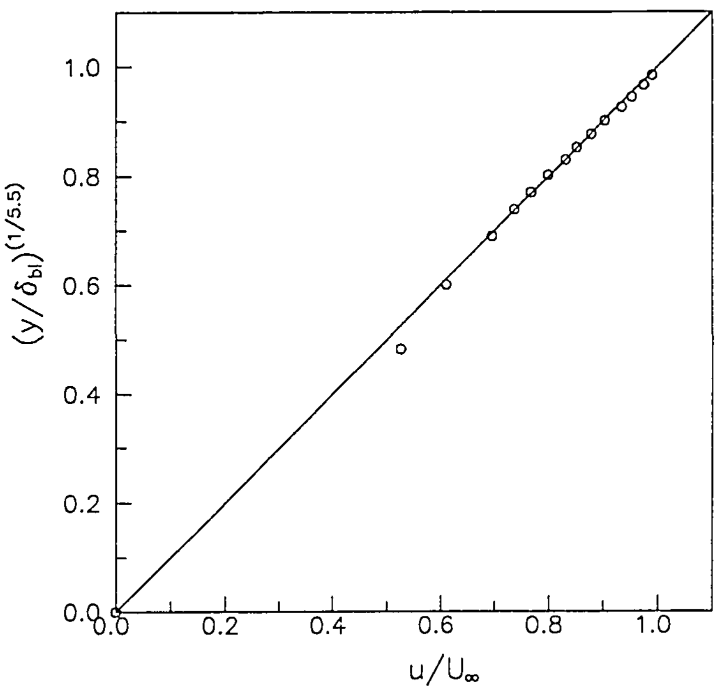

Fig. A.5 Upper surface velocity profiles at 2.5 cm upstream of the base for the 2-D wake model at three spanwise positions (U_∞ = 17 m/s)

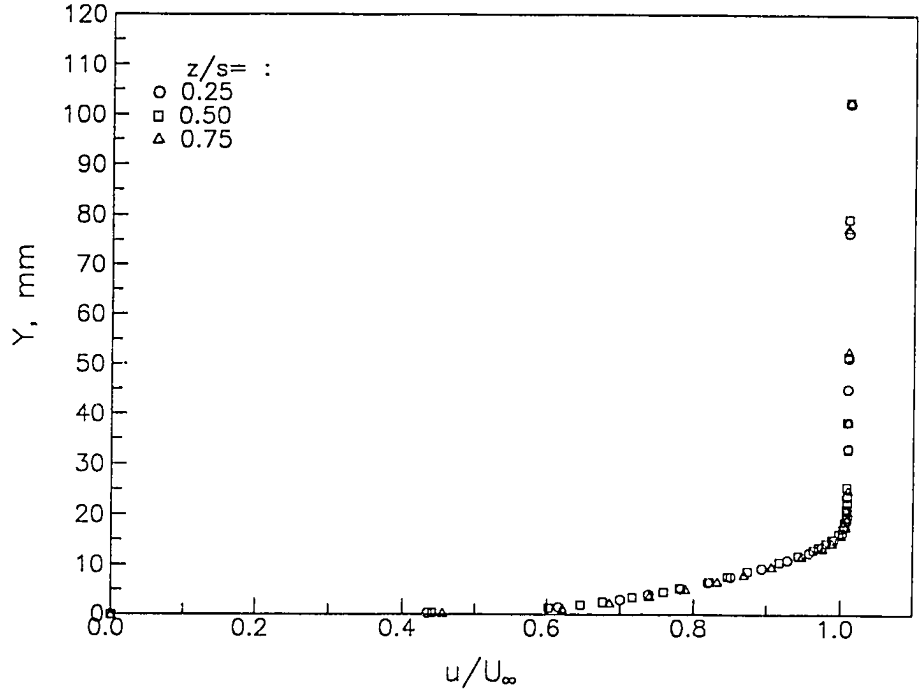

Fig. A.6 Lower surface velocity profiles at 2.5 cm upstream of the base for the 2-D wake model at three spanwise positions (U_∞ = 17 m/s)

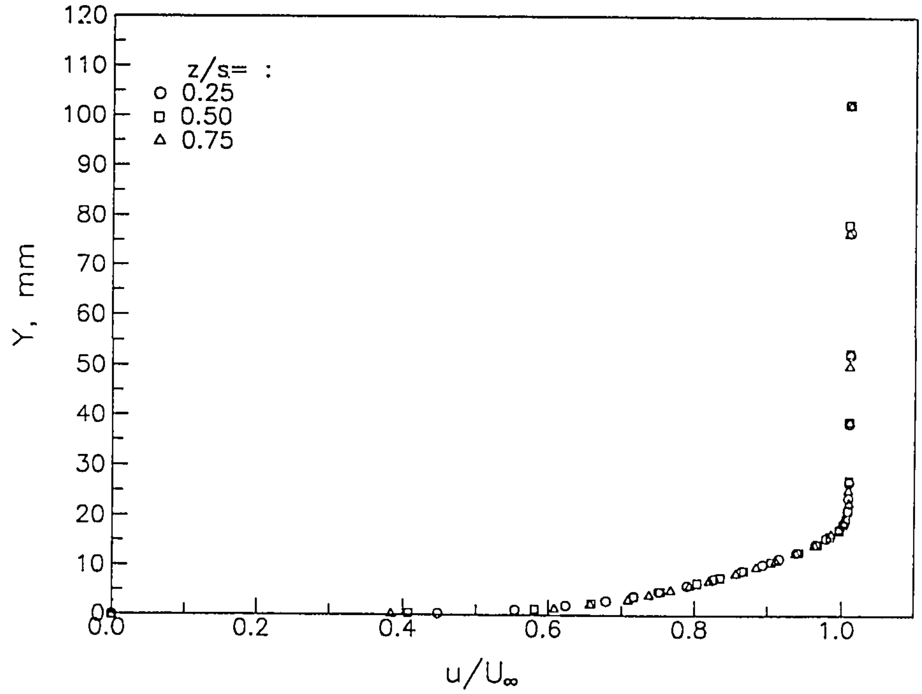

Fig. A.7 Upper and lower surface velocity profiles at 2.5 cm upstream of the base at midspan for the 2–D wake model (U_∞ = 17 m/s)

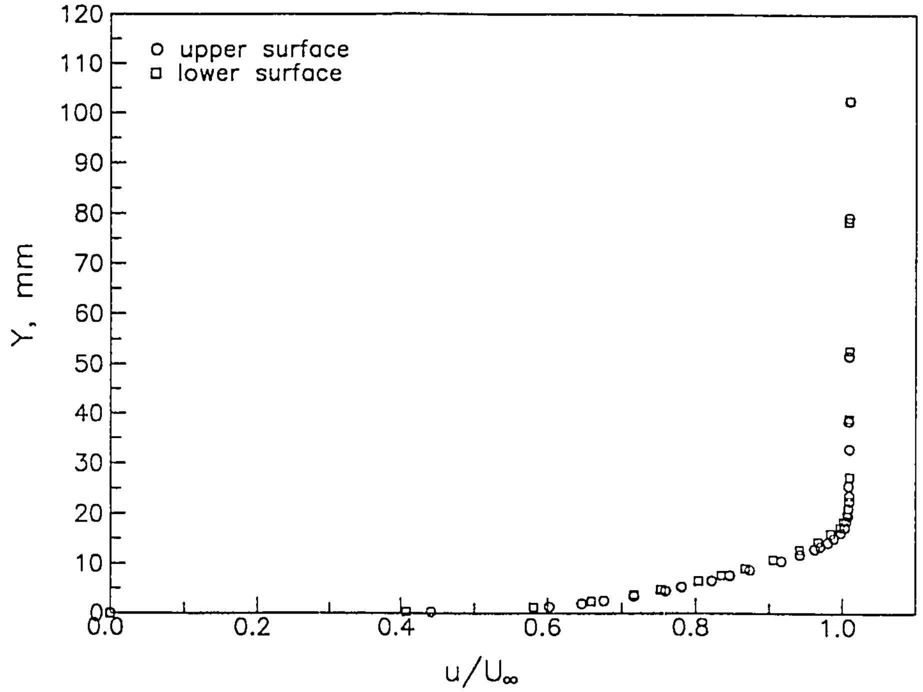

Fig. A.8 Upper and lower surface power-law velocity profiles at mid–span for the 2–D wake model at 2.5 cm upstream of the base (U_∞ = 17 m/s)

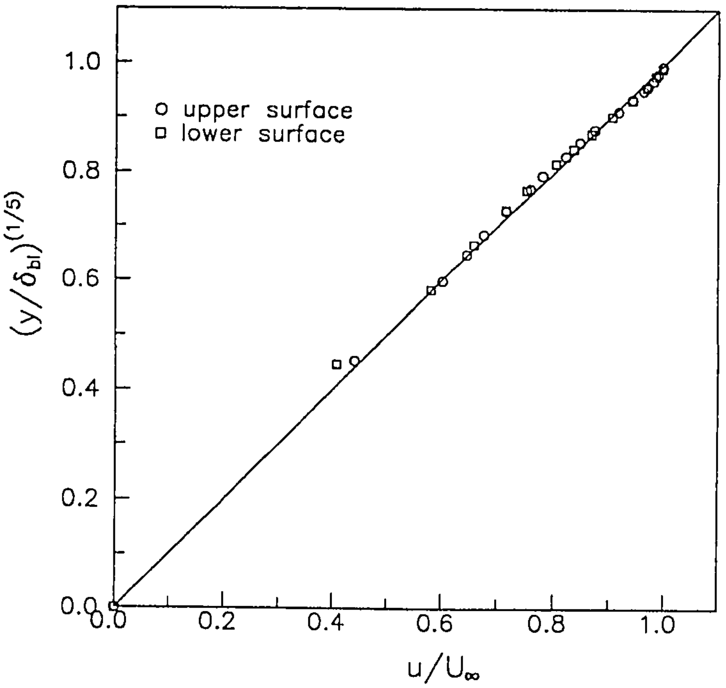

Fig. A.9 Upper and lower surface velocity profiles at 2.5 cm upstream of the base at midspan for the 2-D wake model (U_∞ = 43 m/s)

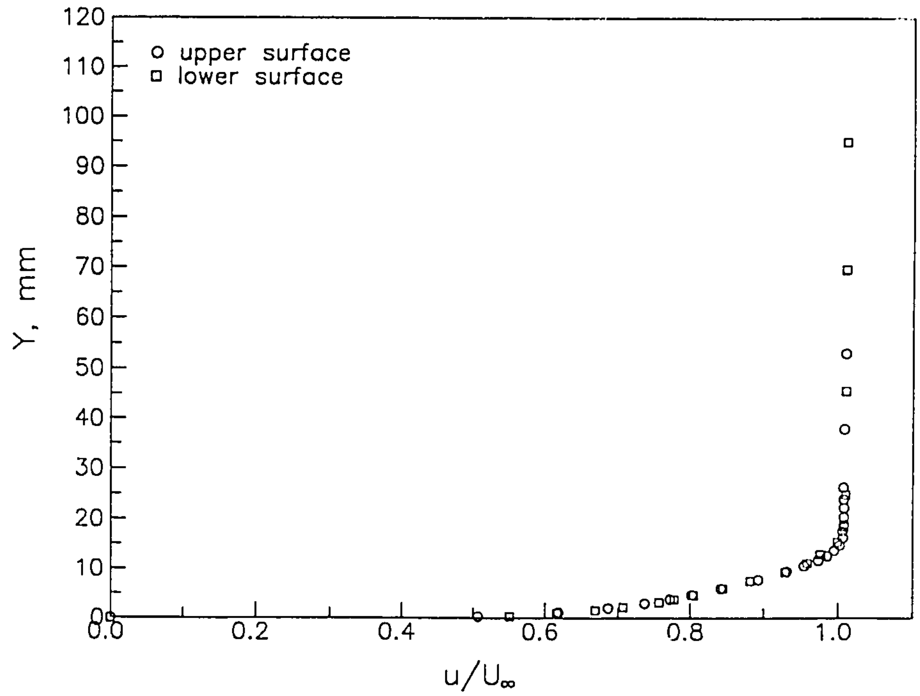

Fig. A.10 Upper surface power-law velocity profiles at mid-span for the 2-D wake model at 2.5 cm upstream of the base (U_∞ = 43 m/s)

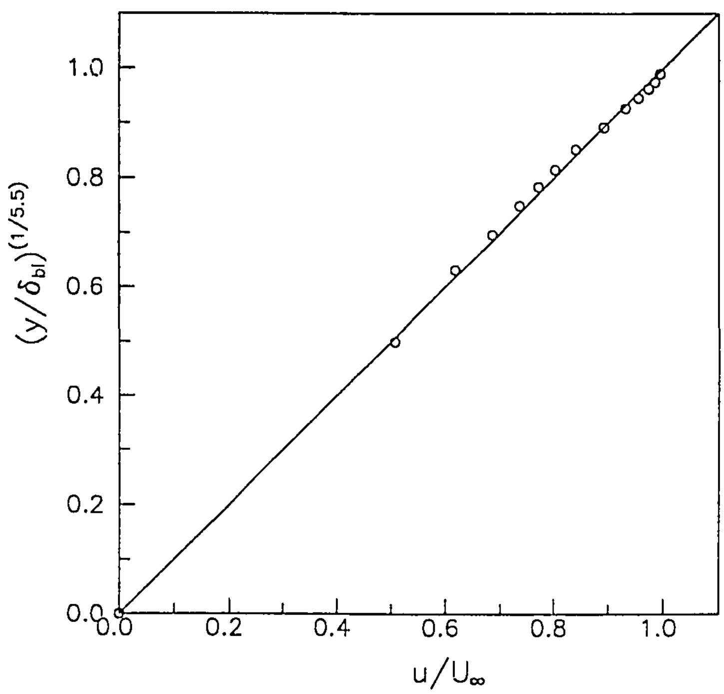

Fig. A.11 Upper surface velocity profiles at 2.5 cm upstream of the base for the 30° swept-base airfoil model at three spanwise positions (U_∞ = 43 m/s)

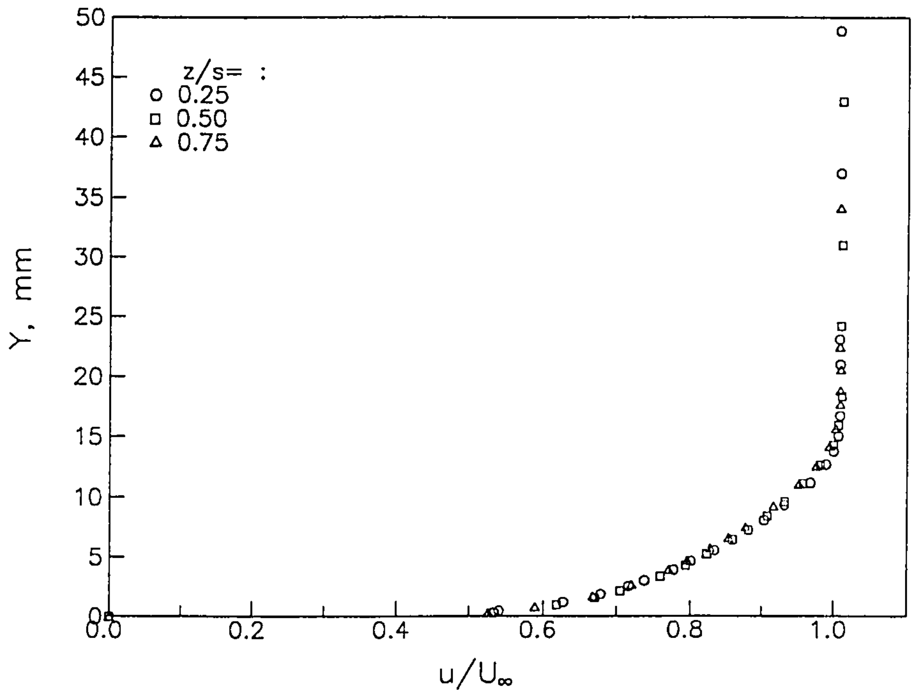

Fig. A.12 Lower surface velocity profiles at 2.5 cm upstream of the base for the 30° swept-base airfoil model at three spanwise positions (U_∞ = 43 m/s)

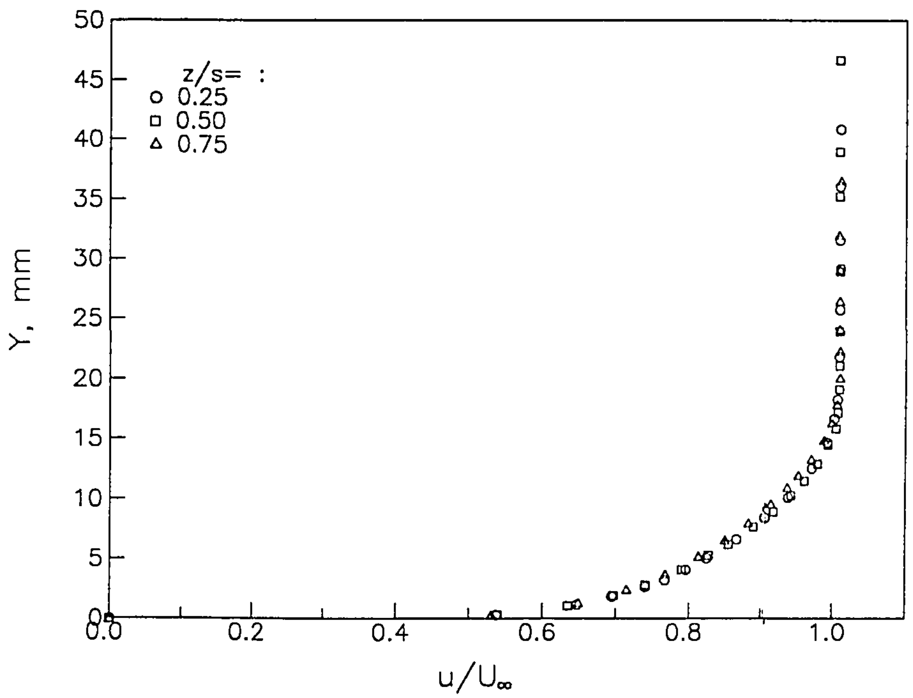

Fig. A.13 Upper and lower surface power-law velocity profiles at mid-span for the 30° swept-base airfoil model at 2.5 cm upstream of the base (U_∞ = 43 m/s)

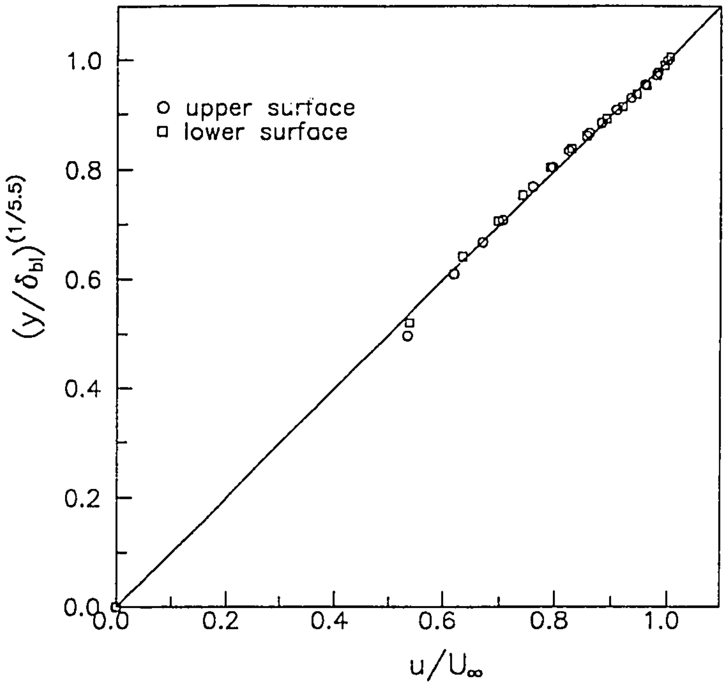

Fig. A.14 Upper surface velocity profiles at 2.5 cm upstream of the base for the 45° swept-base airfoil model at three spanwise positions (U_∞ = 43 m/s)

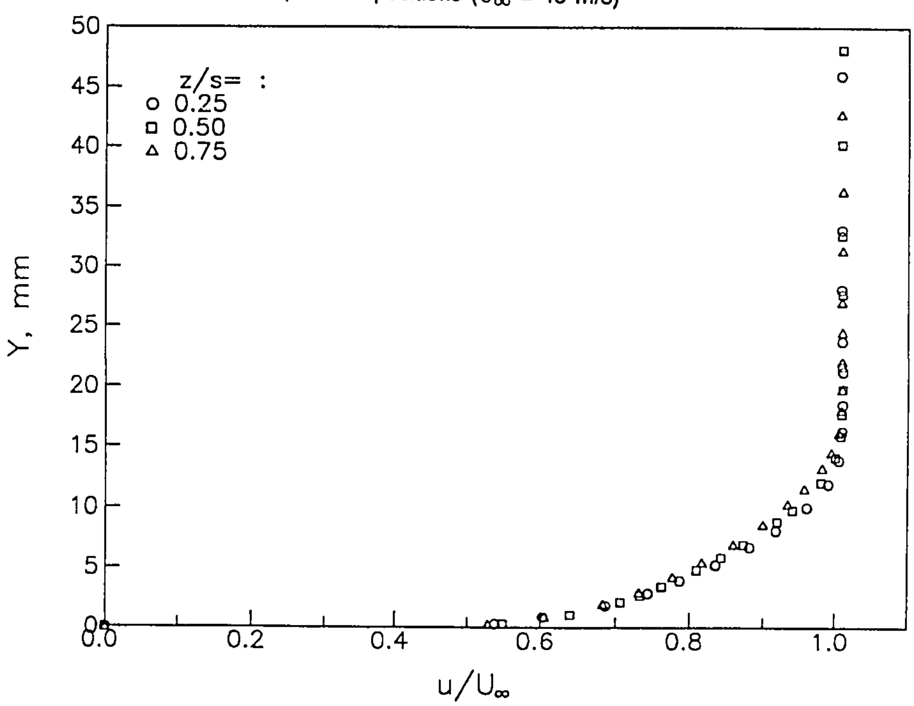

Fig. A.15 Lower surface velocity profiles at 2.5 cm upstream of the base for the 45° swept–base airfoil model at three spanwise positions (U_∞ = 43 m/s)

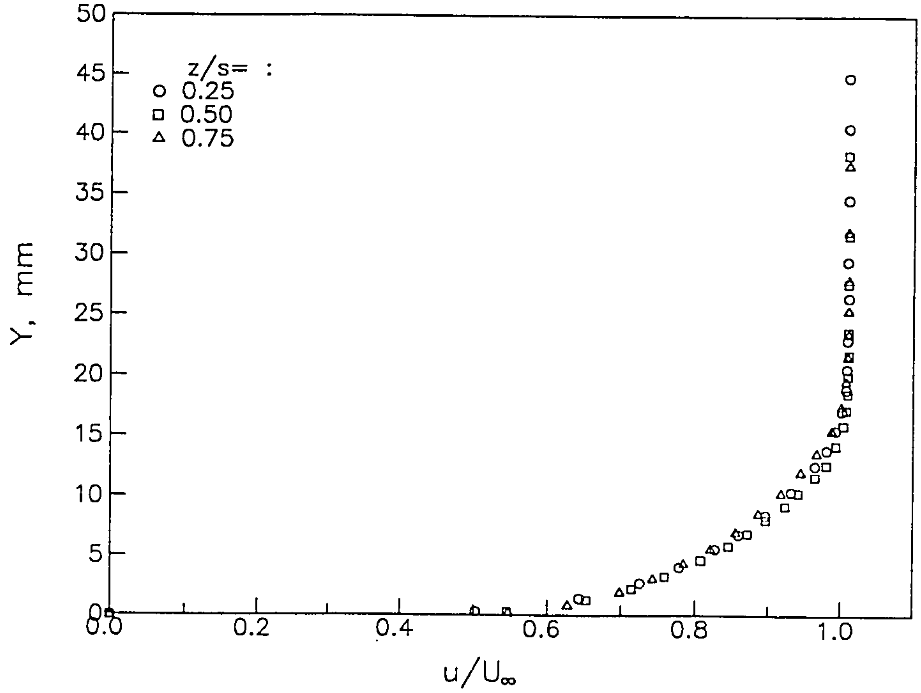

Fig. A.16 Upper and lower surface power-law velocity profiles at mid-span for the 45° swept–base airfoil model at 2.5 cm upstream of the base (U_∞ = 43 m/s)

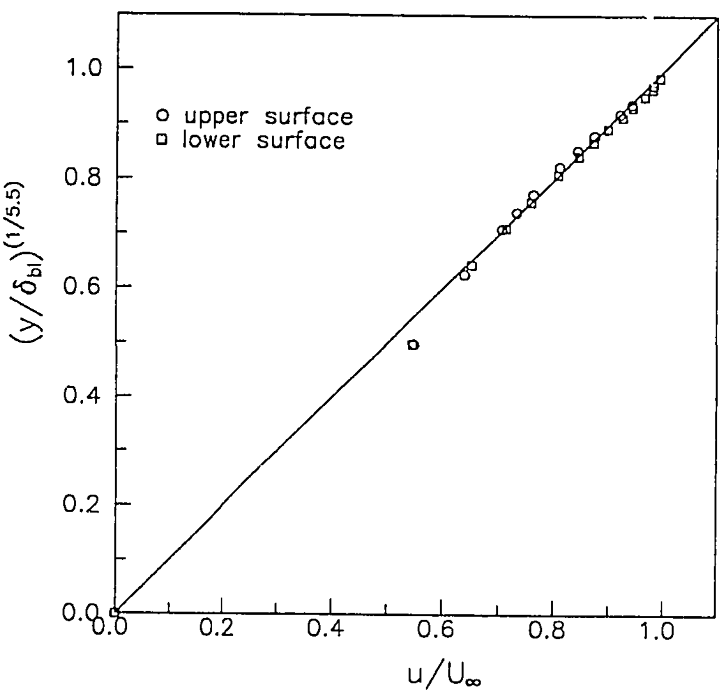

Appendix B

DATA ACQUISITION PROGRAM

```
10   CLEAR ,60000! : IBINIT1=60000! : IBINIT2=IBINIT1+3 : BLOAD "bib.m",IBINIT1
20   CALL IBINIT1(IBFIND,IBTRG,IBCLR,IBPCT,IBSIC,IBLOC,IBPPC,IBBNA,IBONL,IBRSC,
     IBSRE,IBRSV,IBPAD,IBSAD,IBIST,IBDMA,IBEOS,IBTMO,IBEOT,IBRDF,IBWRTF,IBTRAP)
30   CALL IBINIT2(IBGTS,IBCAC,IBWAIT,IBPOKE,IBWRT,IBWRTA,IBCMD,IBCMDA,IBRD,IBRDA
,IBSTOP,IBRPP,IBRSP,IBDIAG,IBXTRC,IBRDI,IBWRTI,IBRDIA,IBWRTIA,IBSTA%,IBERR%,IBCN
T%)
40   '________________________________________________________________
50   '  This program is designed to survey the wake for mean velocity profile
60   '              and static pressure using a pitot-static probe
70   '                          Farid H. Miandoab
80   '________________________________________________________________
90 '
100     DIM PTL(100),PTLSD(100),T(100),TK(100),V(100),Y(100)
110 '
120     GOSUB 290   ' INITIAL DATA
130     GOSUB 470   ' PRINT THE HEADING
140     DT$ = DATE$ : TM$=TIME$
150 '   (IN=1 CORRESPONDS TO NO SLIP CONDITION)
155     INPUT "Initial X reading";XINI
156     INPUT "Initial Z reading";ZINI
157   YINI=9.812 ' PROBE TRAVERSE Y VALUE AT BASE CENTERLINE!
160     FOR IN = 1 TO 100
170 '
180         GOSUB 1430     '  TRAVERSE POSITION & TUNNEL TEMPERATURE
190         GOSUB 1560     '  READING FLUKE TO CALCULATE VELOCITY
200         GOSUB 1250     '  PRINT & FILE THE DATA
210     NEXT IN
215     GOSUB 6000      ' FILE V-Y DATA!
220     LPRINT STRING$(80,205)
230     LPRINT SPC(5);TM$,DT$
240     LPRINT
250     CLOSE #1
260     GOSUB 1650          ' RECORD TEST COMMENTS
270     END
280 '  ----------------------------------------------------------------------
290 '                    INITIAL DATA
300 '  ----------------------------------------------------------------------
310 '
320     CLS : COLOR  4, 11,9 : LOCATE 12,20
330     LOCATE 7,10:INPUT " ATMOSPHERIC PRESSURE ,mm Hg "; PATM
340     LOCATE 9,10:INPUT " AMBIENT TEMPERATURE , deg C  "; TAMB
350     LOCATE 11,10:INPUT " TITLE OF THE TEST   "; TITLE$
360     LOCATE 13,10:INPUT " File Name "; NM$
370     LOCATE 15,10
380     INPUT "NOMINAL SPEED OF THE TUNNEL ,mph ";SP
390     LOCATE 17,10
400     INPUT "Lateral Location of Survey    "; Z : Z=Z-ZINI
410     LOCATE 19,10
420     INPUT " TUNNEL TEMPERATURE ,deg C   "; T(1)
430     CLS: COLOR 1,15, 6
440     FILNM$ = "a:" + NM$ + ".DAT"
450     OPEN FILNM$ FOR OUTPUT AS #1
460     RETURN
470 ' -----------------------------------------------------------------------
480 '                       PRINT THE HEADING
490 ' -----------------------------------------------------------------------
500   LPRINT STRING$(80,178)
510   LPRINT
520   LPRINT
530   NT  = LEN(TITLE$)
```

```
540   NTH = INT(40-NT/2)
550   LPRINT TAB(NTH), TITLE$
560   LPRINT TAB(NTH), STRING$(NT,175)
570   LPRINT
580   LPRINT SPC(5); "FILE NAME: ";NM$;SPC(10);
590   LPRINT DT$;SPC(10);TM$
600   LPRINT
610   LPRINT SPC(5);"ATMOSPHERIC PRESSURE = ";PATM;" mm Hg";SPC(10);
620   LPRINT "ROOM TEMPERATURE = ";TAMB;" deg C"
630   LPRINT
640   LPRINT SPC(5);"Z LOCATION OF SURVEY  = "; Z
650   LPRINT
660   LPRINT SPC(5);"NOMINAL VELOCITY  = ";SP;"mph"
670   LPRINT
680   WRITE #1, TITLE$
690   WRITE #1,DT$,TM$
700   WRITE #1, "FILE NAME : ",NM$
710   WRITE #1, "ATMOSPHERIC PRESSURE = ",PATM
720   WRITE #1, "CROSSFLOW LOCATION OF SURVEY    Z = ", Z
730 '  WRITE #1, 1, Y(1), T(1), PTL(1), PTLSD(1), V(1)
740   LPRINT STRING$(80,240)
750   LPRINT
760   LPRINT  SPC(5);" NO. ";SPC(5);"Y     ";SPC(4);"Temp.";SPC(5);
770   LPRINT  "Dyn. Head";SPC(4);
780   LPRINT "Std. Dev.";SPC(3);"VELOCITY"
790   LPRINT  SPC(15);"  mm  ";SPC(4);" deg C";SPC(5);"  mm Hg  ";SPC(4);
800   LPRINT "  mm Hg  ";SPC(3);"  m/s   "
810   LPRINT  STRING$(80,205)
820   RETURN
830 ' -----------------------------------------------------------------------
840 '                          GET DATA FROM FLUKE
850 ' -----------------------------------------------------------------------
860   BDNAME$ = "FLUKE"
870   BD%  = 6
880   RD$  = SPACE$(14)
890   CALL IBFIND (BDNAME$,BD%)
900   IF BD% < 0 THEN GOSUB 1540
910   CALL IBCLR (BD%)
920   IF IBSTA% < 0 THEN GOSUB 1550
930   CLS
940   COLOR   1,10,9
950   LOCATE  8,30
960   PRINT "Please Wait ! "
970   COLOR 17,10,9
980   LOCATE 12,25
990   PRINT "TAKING DATA FROM FLUKE "
1000   WRT$ = "VR2D5T1M1P8 B200 S0000N1N2N3N4N5N6N7?"
1010   CALL IBWRT(BD%,WRT$)
1020   IF IBSTA% < 0 THEN GOSUB 1550
1030   CALL IBRD (BD%,RD$)
1040   FOR I = 1 TO 200
1050       RD$ = SPACE$(14)
1060       CALL IBRD (BD%,RD$)
1070   NEXT I
1080   WRT$ = "GR8.1,"
1090   CALL  IBWRT (BD%,WRT$)
1100   CALL IBRD (BD%,RD$)
1110   NO   = VAL(RD$)
1120   COLOR  4, 15,9
1130   CLS
```

```
1140   WRT$ = "GR8.2,"
1150   CALL  IBWRT (BD%,WRT$)
1160   CALL IBRD (BD%,RD$)
1170   PTL(IN)  = VAL(RD$)
1180   WRT$ = "GR8.3,"
1190   CALL  IBWRT (BD%,WRT$)
1200   CALL  IBRD (BD%,RD$)
1210   PTLSD(IN) = VAL(RD$)
1220   CALL IBCLR (BD%)
1230   RETURN
1240 '  -----------------------------------------------------------------------
1250 '                            FILE AND PRINT DATA
1260 ' -----------------------------------------------------------------------
1270 '
1280   LPRINT STRING$(5,32);
1290   LPRINT USING "####";IN;
1300   LPRINT STRING$(5,32);
1305   IF IN<= 7 THEN Y(IN)=0     '   READING OF A STATIONARY PITOT PROBE!
1310   LPRINT USING "####.##";Y(IN);
1320   LPRINT STRING$(5,32);
1330   LPRINT USING "###.#";T(IN);
1340   LPRINT STRING$(5,32);
1350   LPRINT USING "##.####";PTL(IN);
1360   LPRINT STRING$(5,32);
1370   LPRINT USING ".####";PTLSD(IN);
1380   LPRINT STRING$(5,32);
1390   LPRINT USING "####.##";V(IN)
1400   WRITE #1, IN, Y(IN), T(IN), PTL(IN), PTLSD(IN), V(IN)
1410   RETURN
1420 ' -----------------------------------------------------------------------
1430 '                          MANUAL DATA INPUT
1440 ' -----------------------------------------------------------------------
1450   CLS : LOCATE 10
1460   PRINT " TYPE ----> 50 <--- TO END TESTING ";C
1470   LOCATE 12:INPUT " TRAVERSE READING " ;YTRD
1480   IF ABS(YTRD)> 49  THEN GOTO 215
1490   LOCATE 14:INPUT " TEMPERATURE deg C    "; T(IN)
1500   Y(IN)  =  (YTRD - YINI)*25.4  ' UPPER SURFACE
1510   TK(IN) = T(IN)  + 273
1520   RETURN
1530 '---------------------------------------------------------------------
1540   PRINT "IBFIND ERROR" : RETURN
1550   PRINT "GPIB ERROR"   : RETURN
1560 '---------------------------------------------------------------------
1570 '                  READING DYNAMIC-HEAD FROM FLUKE
1580 '---------------------------------------------------------------------
1590    R=287
1600    RO=PATM/(R*TK(IN))
1610    GOSUB 830             ' FLUKE
1611  IF IN=2 OR IN=4 OR IN=6 THEN 1630
1615  IF IN=3 OR IN=5 OR IN=7 THEN GOSUB 5000    ' CORRECT REFERENCE P
1620    V(IN)=SQR(2*PTL(IN)/RO)
1630    RETURN
1640 '---------------------------------------------------------------------
1650 '                     COMMENTS ABOUT THE TEST
1660 '---------------------------------------------------------------------
1670    INPUT "TYPE: 1 FOR WORD-PERFECT ...... 2 END ",CC
1680    ON CC GOTO 1690,1700
1690    SHELL "C:\WP50\WP.EXE"
1700    RETURN
```

```
1710 '-----------------------------------------------------------------------
5000 '------------------------------------------------------------------------
5010 '       SUB:  CORRECT REFERENCE STATIC PRESSURE!
5020 '------------------------------------------------------------------------
5030   PTL(IN)=PTL(IN-1)-PTL(IN)
5040   RETURN
5050 '------------------------------------------------------------------------
6000 '-------------------------------------------------------------------------
6010 '    SUB:   OPEN FILE TO STORE V-Y DATA FOR WAKE SURVEY!
6020 '--------------------------------------------------------------------------
6030   MM$="A:W"+NM$+".DAT"
6040   OPEN MM$ FOR OUTPUT AS #2
6050   WRITE #2, MM$
6060   FOR I=8 TO IN-1
6070           WRITE #2,V(I),Y(I)
6080   NEXT I
6090   CLOSE #2
6100   RETURN
6110 '--------------------------------------------------------------------------
```

Appendix C

ERROR ANALYSIS

In the following section, an uncertainty analysis [47] is performed for velocity, pressure coefficient, and Strouhal number measurements.

C.1 Primary Measurements

C.1.1 Uncertainty in Temperature Measurements

The uncertainty in temperature measurement is calculated as follows:

$$\lambda_T = \left(\lambda_1^2 + \lambda_2^2\right)^{1/2} \quad \% \,\mathrm{Rdg} \tag{C.1}$$

where λ_1 is thermocouple thermometer (Fluke: 2176A) uncertainty and λ_2 is the thermocouple wire (type: T) uncertainty. λ_1 and λ_2, according to the manufacturer specifications, are calculated as follows:

$$\lambda_1 = \frac{\sqrt{(0.3)^2 + (0.5)^2 + (0.02\%T + 0.1)^2}}{T}(100) \tag{C.2}$$

where T is the temperature reading of the instrument.

$$\lambda_2 = 0.75\% \ \mathrm{Rdg} \tag{C.3}$$

Substituting for λ_1 and λ_2 in equation (C.1) at the typical test wind tunnel air temperature of 35°C, λ_T is calculated to be

$$\lambda_T = \sqrt{(1.7)^2 + (0.75)^2} \ = 1.9\% \ \mathrm{Rdg}$$

$$T = 35 \pm 0.67 \ ^{\circ}C(\pm 1.9\%)$$

C.1.2 Uncertainty in Differential Pressure Measurement

The uncertainty in differential pressure measurement is calculated as follows

$$\lambda_p = \left(\lambda_{p1}^2 + \lambda_{p2}^2\right)^{1/2} \tag{C.4}$$

where λ_{p1} is the pressure tranducer (MKS Baratron: 310CD-000010) reading uncertainty and λ_{p2} is the multimeter (Fluke: 8520A) reading uncertainty. Then:

$$\lambda_p = \left[(0.08)^2 + (0.01)^2\right]^{1/2} = 0.081\% \text{ Rdg}$$

$$\Delta P = 8 \pm 0.0065 \text{ mm Hg}(\pm 0.081\%)$$

where 8 mm Hg is the maximum dynamic pressure measured for these tests.

C.1.3 Uncertainty in Vortex Shedding Frequency Measurement

The uncertainty in the measurement of vortex shedding frequency is calculated as

$$\lambda_f = \frac{1}{2}(\Delta f)(100)/f \quad \% \text{ Rdg} \tag{C.5}$$

where $\Delta f = \frac{1}{T_r}$ is the frequency resolution of the signal after Fast Fourier Transformation.

$$T_r, \text{time record} = \text{sample size} \times \text{reading rate} \tag{C.6}$$

$$T_r = (4097)(0.0002) \quad \text{sec}$$

f is the measured dominant frequency and is on the order of 340 Hz for the present tests.

$$\lambda_f = \frac{100}{(2)(4096)(0.0002)(340)} = 0.18 \ \% \text{ Rdg}$$

$$f = 340 \pm 0.61 \quad Hz(\pm 0.18\%)$$

C.2 Secondary Measurements

Below are uncertainty calculations for parameters that depended on measurements of the primary parameters.

C.2.1 Uncertainty in the Calculation of Air Density

Density of air is given by

$$\rho_{air} = \frac{P_{atm}}{RT} \tag{C.7}$$

Uncertainty in the calculations of air density is largely due to error in temperature measurement. Therefore

$$\lambda_\rho = 1.17 \pm 0.022\frac{Kg}{m^3}(\pm 1.9\%)$$

C.2.2 Uncertainty in the Calculation of Air Velocity Measurement

Air velocity is calculated as

$$V = \left(\frac{266.8\Delta P}{\rho_{air}}\right)^{1/2} \tag{C.8}$$

where ΔP is the dynamic pressure of air in mm Hg and ρ_{air} is the air density. The uncertainty in air velocity is given by [47]

$$\lambda_v = \frac{\sqrt{\lambda_P^2 + \lambda_\rho^2}}{2} = \frac{\sqrt{(0.081)^2 + (1.9)^2}}{2} = 0.95\% \text{ Rdg} \tag{C.9}$$

C.2.3 Uncertainty in the Calculation of Pressure of Coefficient

Pressure coefficient is defined as

$$C_p = \frac{\Delta P}{\Delta P_\infty} \tag{C.10}$$

uncertainty in C_p is given by

$$\lambda_c = \lambda_P + \lambda_{P_\infty} = 0.081 + 0.081 = 0.16\% \text{ Rdg} \tag{C.11}$$

Note that the measurements of ΔP and ΔP_∞ were made using the same instrument and therefore λ_P and λ_{P_∞} would be considered dependent errors.

C.2.4 Uncertainty in the Calculation of Strouhal number

Strouhal number is defined as

$$St = \frac{fh}{V} \tag{C.12}$$

Neglecting the uncertainty in base thickness measurement, the uncertainty in the calculation of Strouhal number is given by

$$\lambda_s = \left(\lambda_f^2 + \lambda_v^2\right)^{1/2} \tag{C.13}$$

$$\lambda_s = \sqrt{(0.95)^2 + (0.18)^2} = 0.97\% \text{ Rdg}$$